Stony Brook University

Atoms and Molecules in Strong Midinfrared Laser Fields

A Dissertation Presented

by

Cosmin Ioan Blaga

to

The Graduate School

in Partial Fulfillment of the Requirements

for the Degree of

Doctor of Philosophy

in

Physics

Stony Brook University

December 2009

Stony Brook University

The Graduate School

Cosmin Ioan Blaga

We, the dissertation committee for the above candidate for the Doctor of Philosophy degree, hereby recommend acceptance of the dissertation.

Louis F. DiMauro
Adjunct Professor, Department of Physics and Astronomy
and Professor, The Ohio State University, Department of Physics

Edward Shuryak
Distinguished Professor, Department of Physics and Astronomy

Thomas C. Weinacht
Associate Professor, Department of Physics and Astronomy

Trevor J. Sears
Professor, Department of Chemistry
and Senior Chemist, Brookhaven National Laboratory

This dissertation is accepted by the Graduate School.

Lawrence Martin
Dean of the Graduate School

Abstract of the Dissertation

Atoms and Molecules in Strong Midinfrared Laser Fields

by

Cosmin Ioan Blaga

Doctor of Philosophy

in

Physics

Stony Brook University

2009

When atoms and molecules are subjected to low frequency laser fields whose electric fields rival the atomic and molecular ones, the liberated photoelectrons can revisit and subsequently rescatter on their parent ions within a fraction of the laser period. In the last few years, using near-infrared pulses it has been shown that the photoelectron momentum distribution carries the fingerprint of a diffraction pattern from which for molecules it is possible to extract structural information. Given that the maximum kinetic energy of the returning photoelectron wave packet increases with the intensity and the square of the wavelength of the driving field, intense mid-infrared laser pulses should be used instead, since they create wave packets that can have an associated de Broglie wavelength smaller than the ionic size. Coupled with the sub-cycle dynamics of the electron wave packet, this diffraction-based mechanism can form the basis of a molecular camera, capable of "viewing" chemical reactions.

As a first step in the development of such a camera, we recorded high resolution momentum distributions for atoms and molecules extracting diffraction patterns for both near-infrared and mid-infrared driving laser

fields. In addition, a low energy structure present in the photoelectron spectra not predicted by analytical models has been investigated.

To my beloved wife Kathryn and our parents Maria, Mary, Ioan and James

Contents

List of Figures

List of Tables

Acknowledgements

There are many people whose support, guidance and encouragement had contributed to my development as a young scientist and had made this document possible in its current form. It has been a long journey, starting with my highschool years when I decided to become a physicist. In this section I would like to express my gratitude to all of you, but if my memory will let me down and I will forget some of you, please accept my deepest apologies.

First and foremost I would like to express my gratitude to my scientific advisor, Prof. Louis F. DiMauro, for offering me the opportunity to be part of his wonderful, world-class research group. Under his supervision, not only we had everything we needed to conduct successful experiments, but most importantly I am thankful for the freedom given to purse my own ideas, even the "wild" ones. I was also very fortunate to benefit from the vast knowledge and constant encouragement of Prof. Pierre Agostini. For me, Lou and Pierre are and will be two models for what a complete scientist should be and I feel I cannot thank you both enough for *everything*.

Next, I would like to thank those who worked with me on various projects. I would like to thank my friend and colleague Dr. Fabrice Catoire, a rare breed of young scientist with impressive experimental and theoretical skills. I've enjoyed greatly our discussions about physics and otherwise and I'm looking forward to further collaborations. I am grateful to Dr. Kevin Schultz, for his advice during my first years as a graduate student. Special recognition goes to Dr. Juana Rudati-Feser and Dr. Philip Colosimo, which both introduced me to the wonderful world of ultrafast lasers. Fruitful results and a great deal of knowledge was acquired by working with our outside collaborators. I've enjoyed working with Prof. Gerhard G. Paulus on the LES as well as Dr. Christoph Hauri, Dr. Rodrigo Lopez-Martens and Dr. Erik Power on the mid-infrared filaments. I'm also grateful for the collaborations and discussions had over the years with the remaining members of our research group. Many thanks go to to our former and current postdocs: Dr. Jennifer Tate, Dr. Jan Chaloupka, Dr. Pierre-Marie Paul, Dr. Anthony DiChiara, Dr. Ilya Lachko and Dr. Gilles Doumy. Likewise, my fellow graduate students: Dr. Anne-Marie March, Dr. Todd Clatterbuck, Emily Sistrunk, Razvan Chirla, Jonathan Wheeler, Christoph Roedig, Kaikai Zhang and Stephen Schoun.

Earlier in my career I have benefited from the guidance of my undergraduate mentor at "Babeş-Bolyai" University, Prof. Mircea Crişan, as well as Prof. Ioan Grosu and Dr. Ionel Ţifrea. Even earlier, the person who introduced me the the wonderful world of physics, my highschool reacher, Dorin Bunău. Thank you all.

Instrumental in the successful completion of my graduate work were the administrative personnel at Stony Brook University, Brookhaven National Laboratory and The Ohio State University. In particular, I would like to thank our Assistant Director of the Graduate Program at Stony Brook University, our dear Pat Peiliker, who so many times kept me out of trouble whenever my lack of paperwork skills got in the way.

Many thanks are due to my dissertation committee, Prof. Edward Shuryak, Prof. Thomas Weinacht and Prof. Trevor Sears, for their insightful comments.

Finally, I would like to thank my family: my brilliant and beloved wife Dr. Kathryn Krycka, our parents Maria, Mary, Ioan and James, as well as my sister Daniela, her husband Florin and my dear nephew Matei. Your constant support and encouragement over all these years have made this document possible.

Thank you all very-very much!

Chapter 1

A Brief Theoretical Incursion into Strong Field Physics

If one is to squeeze the ∼2,400,000 years of human evolution in 24 hours, the fire was first controlled around 6pm, agriculture emerged 6 minutes to midnight, the industrial revolution started 11 seconds to midnight, quantum mechanics was born around 3.6 seconds to midnight and finally, the laser was invented less than two seconds to midnight. The purpose of this exercise is obviously not to remind the reader when some of the most extraordinary human achievements took place from a historical perspective. Nor was it done to calculate that on this scale a 30 seconds commercial would take us back to Genghis Khan (despite the fact that sometime it feels this way). Instead, it was done to depict in human terms how long it took us to fully understand the quantum origin of light and its interaction with matter, since it is probably a fair assessment to state that at least intuitively, the importance of this interaction was realized from prehistoric times, given that virtually all ancient civilizations attributed various deities to the Sun, Moon, lightning or fire.

The aim of this chapter is to provide the reader with the minimum theoretical background required to understand the wonderful world of strong field physics. As we will see in the next pages, a full theoretical description is not tractable and hence approximations are required. Furthermore, since some of the results presented in this thesis are not fully understood within the framework of these approximate theories, special attention will be given to the limits of each theory. Since these limits stem from the ingredients present in each theory (or the lack thereof), further theoretical and experimental investigations are required to complete our understanding. Finally, all the formulas presented here are given in atomic units, unless stated otherwise. For the reader not familiar with atomic units, Appendix A provides a quick conversion from atomic units to the International System of Units (SI).

1.1 General Considerations

1.1.1 Ionization Regimes in External Electromagnetic Fields

To accurately describe the interaction between atoms and electromagnetic fields, the electromagnetic field needs to be quantized (this is the realm of quantum electrodynamics). However, if we are only dealing with ionization, a classical description of the electromagnetic field via Maxwell's equations is enough. This is not a normal approximation, in the sense that certain ingredients are left out, but an asymptotic treatment, similar to the use of nonrelativistic mechanics in astronomy. The only result that will be kept from quantum electrodynamics is the useful concept of the photon, which will only be used for energy and momentum conservation purposes, just like Albert Einstein did for his Nobel prize winning explanation of the photoelectric effect.

Since in their ground state atoms and molecules are bound systems, an electromagnetic (EM) field can ionize them only if enough energy is transfered to overcome the ionization potential (IP). If the angular frequency ω associated with the EM field is larger than the ionization potential ($\omega > IP$), the atom can absorb a photon and eject an electron whose kinetic energy (KE) will be the difference of the two: $KE = \omega - IP$. This is the essence of the photoelectric effect. Because even a single photon with $\omega > IP$ is enough to ionize the atom, the ionization rate is large at very low intensities. In this case, the weapon of choice to deal with this process is the well established perturbation theory within the framework of nonrelativistic quantum mechanics, with the atomic Hamiltonian being the unperturbed Hamiltonian and the EM field Hamiltonian the perturbation. Since this process is usually described in any half-decent graduate level quantum mechanics textbook for hydrogenic atoms in monochromatic fields and no experimental results presented in this thesis apply to this case, although instructive, no further discussion is necessary on this subject.

On the other hand, if the photon does not have enough energy to overcome the ionization potential, $\omega < IP$, the atom can be ionized only if it is capable of absorbing multiple photons to fulfill the energy conservation:

$$KE = N\omega - IP, \tag{1.1}$$

where N is the minimum number of photons, so that $KE < \omega$. In this process, all N photons need to be absorbed all at once, since there are no *real* atomic states separated by ω. There are however *virtual* ones, called Floquet states [1]. Because N can be very large, to obtain a measurable (or I should say a reasonable) nonlinear ionization rate W_N it is required that many photons are simultaneously "packed" around the atom. This condition is equivalent to saying that the intensity must be

large. If there are no intermediate resonances, the nonlinear ionization rate W_N can be expressed in general terms according to the perturbation theory as:

$$W_N = \sigma_N(\omega, \epsilon)\frac{I^N}{\omega^N}, \tag{1.2}$$

where $\sigma_N(\omega, \epsilon)$ is the generalized multiphoton cross section and I is the intensity generated by the EM field. The cross section depends only on the atomic structure, the frequency of the field and the ellipticity of the field ϵ but it is intensity independent. Obviously, the case $N = 1$ (single photon ionization) can be viewed as a particular case of multiphoton ionization.

At sufficiently large intensities, Eq. (1.2) no longer applies. The reason for this is that as the intensity increases, the perturbation theory breaks down. One indication of the non-perturbative regime is a process called above threshold ionization (ATI), in which the atom absorbs more photons than the minimum required [2]. Not only that, but it is possible to have an ionization rate W_{N+S} larger than W_N, with S being the excess number of photons absorbed. This fact is clearly in contradiction with perturbation theory, since according to this theory the ionization rate should decrease strongly as S increases. An exact point where perturbation theory ends cannot be given, and even if there is one, it would depend on the atom (molecule) and the EM field. However, we can say that in our community the regime beyond perturbation theory is the realm of Strong Field Physics.

At even larger intensities, the EM field is so strong it starts rivaling the atomic potential, opening up another mechanism: tunnel ionization. In this case, the ionization rate is no longer a power law as a function of intensity, but:

$$W \sim \exp(-2(2IP)^{2/3}/3F), \tag{1.3}$$

with F being the strength of the EM field. Since this is the regime investigated in this document, in the following pages we will discuss this process and its predictions in detail for both atoms and molecules.

Finally, at the highest intensities, the external field strength overcomes the atomic potential. This can be viewed as the asymptotic case for tunnel ionization, when the barrier is completely suppressed. For this reason, this regime is referred to us as over the barrier ionization (OTBI). However, it is worth mentioning that while tunnel ionization is a purely quantum mechanical process, over the barrier ionization is not, as it can be fully understood classically.

All the above mechanisms are presented graphically in Fig. 1.1, as a function of field strength and the photon energy.

At this point we have to answer an important question: how do we know if an atom or molecule is ionized via multiphoton or tunneling? The obvious answer would

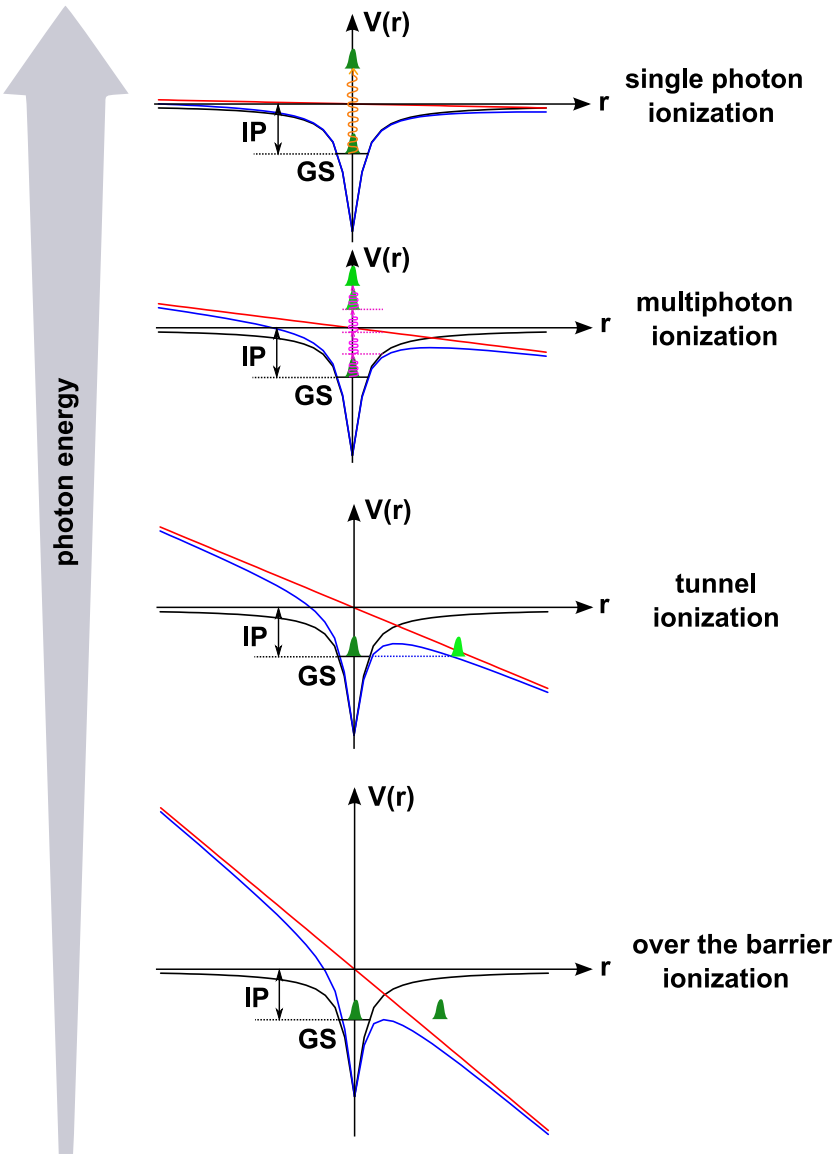

Figure 1.1: **Ionization regimes as a function of electric field strength.** From top to bottom: single ionization (low field strength), multiphoton ionization (moderate strength), tunnel ionization (high field strength) and over the barrier ionization (very high field strength). The atomic potential is in black, the laser field in red, the total potential in blue and the electron wave packet in green. IP denotes the ionization potential and GS the ground state.

be to perform a full calculation of the ionization rates for both cases and see which one dominates. However, this is not an easy task. In fact, it is an impossible task, since the problem does not have an analytical solution for either case. And even if one can live with certain approximations or numerical calculations, is there any back of the envelope estimation available? It turns out there is, thanks to Leonid Keldysh. According to Keldysh [3], the passage from multiphoton to tunneling is governed by the adiabacity parameter γ (also called the Keldysh parameter) given by:

$$\gamma = \frac{tunneling\ time}{optical\ angular\ period}. \tag{1.4}$$

If $\gamma \ll 1$ tunnel ionization dominates and if $\gamma \gg 1$ multiphoton ionization does.

As stated above, Eq. (1.4) should cause the reader who took a quantum mechanics class to immediately object to it. Indeed, tunneling time is still an ambiguous quantity in modern quantum mechanics. Some physicists suggest tunneling time is zero, some finite while others even claim that is meaningless [4] (and the references therein). What Keldysh understood by tunneling time (τ) is that it is the time that it takes for a classical electron with a velocity v determined by the virial theorem applied to the unperturbed ground state to pass through the barrier of thickness L (in atomic units):

$$\langle KE \rangle = \frac{v^2}{2} = \frac{L^2}{2\tau^2} = IP. \tag{1.5}$$

Neglecting the atomic size, the barrier thickness can be approximated using the fact that on the other side of the barrier we have $F \cdot L = IP$, so we can finally write:

$$\gamma = \sqrt{2IP}\,\frac{\omega}{F}. \tag{1.6}$$

One of the most important quantities used in strong field physics and which will be used throughout this dissertation is the ponderomotive potential. Its meaning is very simple. When a free electron is placed in an electromagnetic field, it oscillates with the period of the field. In this situation, the electron's cycle-averaged kinetic energy is the above mentioned ponderomotive potential. It is usually designed as U_P and it is given by [5]:

$$U_P = \frac{A_0^2}{4}, \tag{1.7}$$

where the newly introduced quantity A_0 is the magnitude of the vector potential of the EM field. This expression is a general one, since it does not depend on the polarization of the light. In the case of linear polarization, a more useful formula for

calculating the ponderomotive potential is:

$$U_P[eV] = 9.3 \cdot I[10^{14}W/cm^2] \cdot \lambda^2[\mu m].$$

Introducing Eq. (1.7) into Eq. (1.6), we obtain the following well-known expression for the Keldysh parameter as a function of U_P and IP:

$$\gamma = \sqrt{\frac{IP}{2U_P}}. \tag{1.8}$$

1.1.2 AC Stark Shifts and the Ponderomotive Potential

Subjecting atomic and molecular systems to electromagnetic fields causes their energy levels to shift and split through the well known AC Stark effect. The magnetic nature of the field also produces the Zeeman effect, but since in our experiments the relativistic regime was not reached, its magnitude is rather small and therefore its role can be neglected. On the other hand, the magnitude of the AC Stark effect at intensities reaching the petawatt per squared centimeter is significant and in general it depends not only on the strength and frequency of the applied field but also on the quantum details of each particular state as well. In this subsection I will briefly present the consequences of these AC Stark shifts the their connection with the ponderomotive potential.

When dealing with this issue, most authors prefer to present the AC Stark shift in the multiphoton limit [5]. Although there are good practical reasons to do so, at least from a pedagogical perspective this can be detrimental, since Stark shifts are general in nature, manifesting themselves from the lowest to the highest of intensities. As we will see later in the experimental section dedicated to the laser driven Auger decay, the Stark effect is crucial in the tunneling regime as well.

With this warning in mind, I will describe the AC Stark shifts in the traditional way using the perturbation theory. While not entirely accurate, since I have mentioned already that in the strong field limit the perturbation theory breaks down, for the purpose of understanding this effect this will suffice. In this case, the AC Stark shift of n-th atomic level, which I will label δE_n is given by:

$$\delta E_n = -\frac{1}{4}\chi_n(\omega)F_0^2, \tag{1.9}$$

where I introduced the dynamical polarizability of the n-th level $\chi_n(\omega)$, given by:

$$\chi_n(\omega) = 4\sum_{n'} |(d_x)_{n,n'}|^2 \frac{2(E_{n'} - E_n)}{(E_{n'} - E_n)^2 - \omega^2}. \tag{1.10}$$

In the last equation d_x is the projection of the dipole operator along the laser polarization (chosen here as the x-axis). In general, the dipole matrices are complicated, depending on the wave functions of each atomic and molecular level. Since the matrix elements are complex numbers, the resulting polarizabilities can be either positive or negative, resulting in so-called low field or high field seeking states. For highly excited states, for which n is large, Eq. (1.10) has the simple asymptotic limit $\chi_n(\omega) = -\omega^{-2}$, resulting in the following expression for the AC Stark shift:

$$\delta E_{n\to\infty} = \frac{F_0^2}{4\omega^2}. \tag{1.11}$$

Noting that if we substitute the EM field strength with the vector potential in the last equation ($F_0 = A_0\omega$), the AC Stark shift in the asymptotic limit is just the ponderomotive potential U_P. The meaning is very simple. To promote an electron into the continuum, it is not enough to supply only an amount of energy equal to the ionization potential, but also an amount of kinetic energy, equal to U_P to make it quiver in the field. This has the effect of increasing the ionization potential from the field-free value of IP to the field value $IP + U_P$. As a consequence, the energy conservation law given in Eq. (1.1) should read:

$$KE = N\omega - (IP + U_P). \tag{1.12}$$

Although strictly speaking Eq. (1.1) should be replaced with Eq. (1.12), the two formulas are valid for two different cases if we want to compute the energy of an electron *at detection*, long after the pulse is gone. The two cases stem from the interplay between the pulse duration τ (which gives the ponderomotive shift of the continuum during this time) and the time t it takes the ionized electron to leave the focal volume. Despite the fact that for both cases the electron is born near the peak of the field (in the presence of U_P), if $t \gg \tau$ as is the case for long pulses, it will roll down the ponderomotive potential effectively gaining back one unit of U_P. For this reason Eq. (1.1) can be used for long pulses whereas Eq. (1.12) is used for ultrashort pulses.

The above considerations are presented in graphical form in Fig. 1.2. In general, the AC Stark shift of the ground state is much smaller than that of the Rydberg states. In addition, the AC Stark shift can lift state degeneracies, if present. For the inner shell, the AC Stark shift is not shown. To take it into account and prove that it is insignificant a complicated multielectron computation is needed, beyond the purpose of this dissertation. However, a classical, intuitive reasoning can be provided. Since the valence shell (the ground state) is at least partially filled with electrons, they form a Faraday cage around the atom, shielding the inner shell electrons from the influence of the external field. As a consequence, the AC Stark shift of inner levels is ignored.

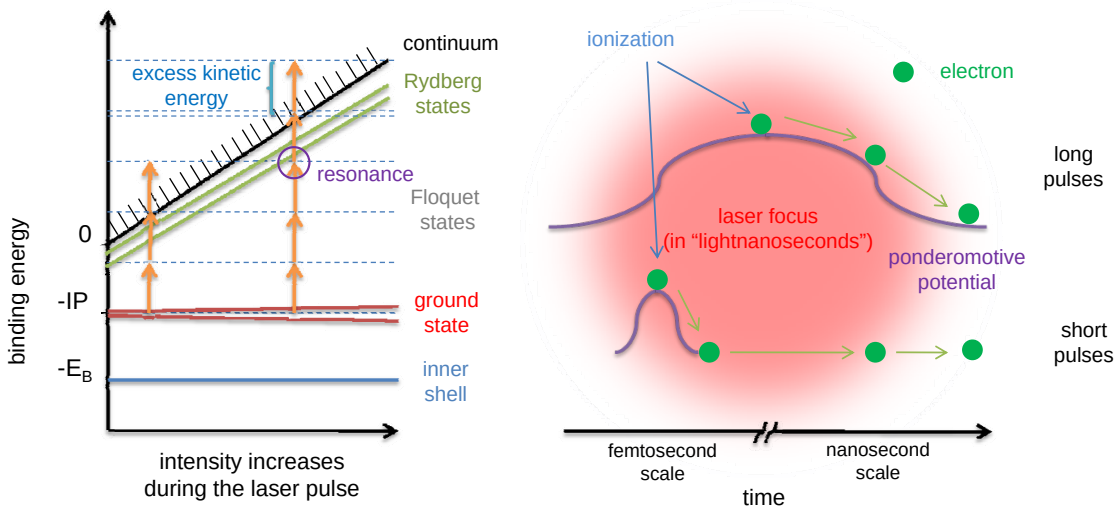

Figure 1.2: **AC Stark shift of energy levels.** Left panel: as intensity increases, the energy levels suffer AC Stark shifts. The magnitude of the shift is given by the product between the polarizability of each level and the square of the EM field strength. Right panel: the interplay between the pulse duration and the time it takes the ionize electron to leave the laser focus determines the energy of the electron at the detector. (see text for details)

1.2 Single Ionization Models for Atoms and Molecules in an Electromagnetic Field

1.2.1 Ammosov-Delone-Krainov (ADK) Theory for Tunnel Ionization

The first of the three theories presented in this section developed over the years to explain the behavior of atoms and molecules in strong laser fields is the Ammosov-Delone-Krainov (ADK) approximation. While the original formulation can be found here [6], in [7] a step by step detailed derivation can be found, perhaps more suitable for entry-level graduate students. The major benefits of this theory are its simplicity and a straightforward physical interpretation, which lead to its early adoption and widespread use. The main idea is very simple: in slow varying fields ($\gamma \ll 1$), the electric field changes slow enough that a static tunneling rate W_{static} can be calculated for each instantaneous value of the electric field, with the overall tunneling rate W_{ADK} being just the sum of all the static rates. Before we go into the details of

this approximation, we first notice that as stated above the ADK does not describe the ionization process in its entirety. Indeed, the propagation of the ejected electron is completely left out, so that ADK alone cannot predict the photoelectron energy and angular distributions as measured at the detector. Additionally, the electron might recombine with its parent ion after ionization in a process called high harmonic generation (HHG), which also is not included in this model. However, coupled with rate equations to take into account ground state depletions, ADK is a great tool for predicting or explaining experimental ionization rates from arbitrary charge states, especially in highly elliptical laser fields (so that the restrictions listed above do not apply). For linear polarization however, because (e,2e) processes are not included, ADK gives good results only for single ionization.

The starting point of the theory is the so-called Landau-Dykhne adiabatic approximation, which provides the following expression for the ionization rate between the initial and final states:

$$W_{i\to f} = \exp\left\{-2\mathrm{Im}\int_0^{t_0}[E_f(t) - E_i(t)]dt\right\}, \tag{1.13}$$

where E_f and E_i are the energies of the final and initial states, respectively. The integration limit t_0 is the complex time corresponding to the tunnel exit (called the outer classical turning point), given by:

$$E_i(t_0) = E_f(t_0). \tag{1.14}$$

Before we go any further we should mention here that the Landau-Dykhne formula can be obtained easily from the action, if we assume that the amplitude of the wave function changes slowly (adiabatically) during the process. This link is not just a mere computational artifact, but it has the profound meaning that it provides a connection between ADK and the next two models to be described latter in this chapter (SFA and TDSE). In effect, all three theories can be traced back to the principle of least action, which in turns is at the core of Feynman's path integral formulation of quantum mechanics.

The validity of the ADK approximation is governed by the accuracy in determining the three quantities involved in Eq. (1.13). For $E_i(t)$, one usually uses the value of the unperturbed ionization potential, therefore neglecting the AC Stark effect displacement of the ground state. This effect can be included, but because the shift depends on the polarizability of the ground state which is atom dependent, this automatically sacrifices the generality of the final result. In addition, since the only atoms studied in this document were all noble gases their tightly bound ground states AC Stark shift by small amounts so we can in a first approximation neglect their corre-

sponding shifts. For other systems, with ground states close to the continuum (small ionization potentials) such as alkali atoms, negative ions or weakly bound molecules, ADK should be used with a cautious eye. Therefore, to obtain a general result we will ignore the Stark effect so in practice we always have $E_i(t) = -IP$.

For the final energy $E_f(t)$ we can use the general formula:

$$E_f(t) = \frac{(\vec{\mathbf{p}} - \vec{\mathbf{A}})^2}{2} + V_C, \tag{1.15}$$

where $\vec{\mathbf{p}}$ is the canonical momentum, $\vec{\mathbf{A}}$ is the vector potential of the EM field and V_C is the Coulomb potential of the atomic or molecular core. In its original formulation ADK neglected the Coulomb potential in $E_f(t)$. Far from saturation (by saturation meaning the onset of over the barrier ionization), the barrier is thick and since the Coulomb potential has a $1/r$ dependence this approximation is justified. For this reason, if we put $V_C = 0$ in Eq. (1.15), we have the short range formulation of ADK (the atomic potential only matters for the inner turning point). Finally, it can be seen from Eq. (1.13) that $W_{i\to f}$ is maximum at $\vec{\mathbf{p}} = 0$ if V_C is zero. Therefore, as a first step we can assume that the electron tunnels out of the barrier with $\vec{\mathbf{p}} = 0$.

In this case, for a complex atom in linearly polarized field [6]:

$$W_{atom}^{linear}(\vec{\mathbf{p}} = 0) = D(n^*, l, m)\left(\frac{2Z^3}{Fn^{*3}}\right)^{2n^* - |m| - 1}\left(\frac{3Fn^{*3}}{\pi Z^3}\right)^{1/2}\exp\left(-\frac{2Z^3}{3n^{*3}F}\right), \tag{1.16}$$

where the constant $D(n^*, l, m)$ is given by:

$$D(n^*, l, m) = \frac{(2l+1)(l+|m|)!}{2^{|m|}(|m|)!(l-|m|)!}\left(\frac{2e}{n^*}\right)^{2n^*}\left(\frac{Z^2}{4\pi n^*}\right).$$

The quantities that enter in the above formulas are the atomic charge Z, the effective principal quantum number $n^* = Z/(2E_H)^{1/2}$ where E_H is the ionization potential of the hydrogen atom, the orbital and magnetic quantum numbers l and m and finally e is the base of the natural logarithm.

The corrections to Eq. (1.16) for nonzero momenta where found by Nikishov and Ritus [8] and Delone and Krainov [9]:

$$W_{atom}^{linear}(p_\parallel) = W_{atom}^{linear}(\vec{\mathbf{p}} = 0)\exp\left(-\frac{p_\parallel^2\omega^2(2IP)^{3/2}}{3F^3}\right) \tag{1.17}$$

and respectively

$$W_{atom}^{linear}(p_\perp) = W_{atom}^{linear}(\vec{\mathbf{p}} = 0)\exp\left(-\frac{p_\perp^2(2IP)^{1/2}}{F}\right). \tag{1.18}$$

Equations (1.16), (1.17) and (1.18) are the heart of short range atomic ADK approximation. More recently, Ristic et al. [10] included a Coulombic correction in the calculation of the outer turning point, essentially extending the validity of the ADK approximation for long range potentials. The correction turned out to be small, only affecting the preexponential factor, but not the exponential behavior. For $m = 0$ (in general all m's have to be included, but it can be easily seen from Eq. (1.16) that $m = 0$ dominates), the correction is:

$$\left(\frac{2Z^3}{Fn^{*3}}\right)^{2n^*-1} \longrightarrow \left(\frac{2Z^3}{Fn^{*3}}\frac{1}{1+\frac{2ZF}{(\vec{\mathbf{p}}^2+2IP)^2}+\frac{(ZF)^2}{2IP(\vec{\mathbf{p}}^2+2IP)^3}}\right)^{2n^*-1}. \tag{1.19}$$

For many years, ADK was applied exclusively for atoms, primarily because no lasers were capable to take the molecules with their usually small ionization potential into the tunneling regime. However, using the same principles used for atoms, recently Tong et al. [11] successfully extended ADK to molecules (the authors abbreviated the extended theory as MO-ADK). The main idea was to expand the radial molecular wave function in the asymptotic region (that is near the turning points) as a superposition of spherical harmonics generated from the individual centers. The weight of each harmonic depends on the shape of the molecular orbital as well as the orientation of the molecule with respect to the laser polarization. After time-averaging over one period of the EM wave, the ionization rate as a function of the field strength F and an arbitrary orientation angle $\vec{\mathbf{R}}$ is:

$$\begin{aligned} W^{linear}_{molecule}(F,\vec{\mathbf{R}}) = &\sum_{m'}\frac{B^2(m')}{2^{|m'|}\mid m'\mid !}\left(\frac{n^*}{Z}\right)^{2n^*-1}\left(\frac{2Z^3}{Fn^{*3}}\right)^{2n^*-|m'|-1}\times \\ &\times\left(\frac{3FZ^3}{\pi n^{*3}}\right)^{1/2}\exp\left(-\frac{2Z^3}{3n^{*3}F}\right). \end{aligned} \tag{1.20}$$

The function $B(m')$ is given for an arbitrary orientation by:

$$B(m') = \sum_l C_l D^l_{m',m}(\vec{\mathbf{R}})Q(l,m')$$

with C_l being constants that give the weight of each spherical harmonic when the molecular axis is aligned along the laser polarization, $D^l_{m',m}$ the rotation matrix and $Q(l,m')$:

$$Q(l,m') = (-1)^{m'}\sqrt{\frac{(2l+1)(l+\mid m'\mid)!}{2(l-\mid m'\mid)!}}.$$

molecule	C_l		
or ion	$l=0$	$l=2$	$l=4$
$H_2^+(\sigma_g)$	4.37	0.05	0.00
$D_2(\sigma_g)$	2.51	0.06	0.00
$N_2(\sigma_g)$	2.02	0.78	0.04
$O_2(\pi_g)$	–	0.62	0.03

Table 1.1: C_l **coefficients for homonuclear diatomic molecules.**(from [11])

The values of C_l for several diatomic molecules are given in Table 1.1, taken from [11]. The similarities between molecular ADK and atomic ADK are striking, as it can be seen from Eqs. (1.16) and (1.20). First, the ionization rate is dominated by the exponential factor, which is identical in both cases. This should not come as a surprise, since it is known that in general quasi stationary states decay exponentially in tunneling processes. Second, even some of the prefactors are identical, a testimony of the fact that in both formulas the outer turning point was found neglecting the Coulomb potential. Finally, even including the Coulomb potential would probably provide similar results, since for both atoms and molecules the long range behavior of the Coulomb potential is of the same $1/r$ form. To the best of my knowledge, a generalized molecular ADK formulation that includes Coulomb corrections has not been developed yet.

One of the major findings of molecular ADK is the fact that the ionization rate depends rather consistently on the orientation of the molecule, presenting a maximum if the molecular cloud is aligned parallel to the laser polarization. For example, based on their molecular configuration, nitrogen ionizes more readily if the molecular axis is parallel to the field while oxygen prefers to ionize when the molecule is aligned perpendicular to the field. This prediction was tested successfully and the data is presented in the subsequent chapters.

1.2.2 Keldysh-Faisal-Riess Strong Field Approximation (KFR-SFA)

In quantum mechanics, the exact transition amplitude between an initial state $|i\rangle$ and a final state $|f\rangle$ can be expressed as:

$$M_{i\to f}(t) = -i\int_{-\infty}^{t}\langle i|V(t')|f\rangle dt', \tag{1.21}$$

where $V(t)$ is the interaction potential and all dependencies other than time were omitted. The usefulness of the above formula is limited for computational purposes,

because the exact expressions for the two states involved are in general not known. However, it can be the starting point if one can approximate the two wave functions. In 1963, Keldysh [3] approximated the above formula by neglecting the effect of the atomic potential on the final state. While the exact formula (1.21) is always gauge invariant, approximate methods usually are developed sacrificing gauge invariance. Primarily for this reason, depending on the gauge chosen, there are several formulations of the KFR-SFA, each with its strengths and weaknesses. A detailed presentation of all these formulations can be found in the review article by Milošević [12]. In the following, we will only follow Keldysh's original formulation.

In the length gauge, $V(\vec{\mathbf{r}},t) = \vec{\mathbf{r}} \cdot \vec{\mathbf{F}}(t)$, the wave function of a "free" electron in an electromagnetic field (by "free" meaning no Coulomb potential) is:

$$\langle \vec{\mathbf{r}} | f^V(\vec{\mathbf{p}},t) \rangle = \frac{e^{i\vec{\mathbf{r}}[\vec{\mathbf{p}}+\vec{\mathbf{A}}(t)]}}{(2\pi)^{3/2}} \exp\left\{ i \int_t^\infty \frac{[\vec{\mathbf{p}}+\vec{\mathbf{A}}(\tau)]^2}{2} d\tau \right\}. \tag{1.22}$$

The above wave function is called a Volkov state and it describes an electron under the solely influence of an EM field.

Introducing the action (which provides the connection with ADK as we mentioned before)

$$S(t) = \frac{1}{2} \int_t^0 [\vec{\mathbf{p}} + \vec{\mathbf{A}}(\tau)]^2 d\tau + IPt \tag{1.23}$$

the transition amplitude can be expressed as:

$$M_{\vec{\mathbf{p}}}^{direct} = i \frac{Z^{5/2}}{\pi\sqrt{2}} \int_0^{kT} \frac{\exp[iS(t)]}{\partial S(t)/\partial t} dt, \tag{1.24}$$

where T is the period of the laser pulse, Z is the atomic number and k is an integer. The transition amplitude as expressed in Eq. (1.24) can be solved using the saddle point method, by finding the roots in the integrand's denominator. It turns out there are two such points, both complex. The real part of the two saddles are the birth times, i.e. the phase at which the electron is promoted from the ground state into the continuum. These phases correspond to the same values of the vector potential $A(t_1) = A(t_2)$. As such, one can write the transition amplitude as a sum of two terms and since the ionization rate is the squared of the sum, an interference term will be present. This interference term is not present in ADK because ADK was derived in the static case and we only integrated the ionization rate to account for the oscillatory motion in the field. As a result, the phase information of the ADK transition amplitude was lost. We will come back to this interference term in the last section of the experimental chapter.

Using the saddle point method, the final transition amplitude is in Keldysh's approach:

$$M_{\vec{\mathbf{p}}}^{direct} = -\frac{Z^{5/2}}{\sqrt{2}} \sum_{n=1,2} \frac{\pi \exp[iS(t_n)]}{F(t_n)(IP + p_\perp^2)^{1/2}} \exp\left[-\frac{(2IP + p_\perp^2)^{3/2}}{3F(t_n)}\right], \tag{1.25}$$

where the sum is obviously done over the two saddle points. From this point forward the calculation of the ionization rate has to be performed numerically by finding the two saddle points for each value of the electric field.

Before we end however, few remarks are in order. KFR-SFA is not only applicable to tunneling, but also multiphoton since nowhere in the calculation we made the distinction between the two regimes. For this reason KFR usually matches the experiment better than ADK, especially in the region where $\gamma \sim 1$. The theory is also closely related via the S-matrix to the Born approximation. In its simplest form described above, only the first order Born approximation was used, since we did not include the Coulomb potential in the continuum. However, a generalization does exist which accounts for the presence of the Coulomb potential, but to my knowledge only in the second order [25]. This means that a single electron-ion core scattering event is permitted. To allow multiple returns, higher and higher orders are needed, which pose significant computational challenges. However, one rescattering event is enough to explain many features of the ionization process, such as high harmonic generation and the existence of the plateau in the photoelectron spectrum (the latter will be presented shortly). Although we only covered the case for an atom, KFR-SFA models were successfully adapted to cover molecules as well. Finally, since it is a fully quantum mechanical theory, KFR allows us to investigate interference effects in the electron energy and angular distribution spectra (although for a quantitative analysis KFR must take into account Coulomb effects).

1.2.3 Single Active Electron Time Dependent Schrödinger Equation (SAE-TDSE)

The last theoretical approach that will be presented in this section is the numerical evaluation of the time-dependent Schrödinger equation. If we are only interested in the study of processes that involve just one electron, such as single ionization or high harmonic generation, the single active approximation works extremely well. On the other hand, multiple ionization and electron-electron correlations can only be described by bringing additional electrons into the picture. For this purpose, two electron one dimensional and three dimensional TDSE codes have been developed ([26] and [27]). However, these multielectron calculations require a vast amount of

computational power (especially in 3D) and in general they are only carried out on the most powerful supercomputers. In this chapter, we will only address the case of the single active electron (SAE), presenting only the general characteristics of the method.

The main advantage using TDSE is the fact that we can obtain accurate results, because all the essential ingredients are included in the calculation: the long range Coulomb potential, the ground state and all excited states, realistic pulse shapes as well as a full description of the electron wave packet in the continuum. Because the method essentially provides the full time-dependent wave function at the end of the calculation, any physically measurable quantity can be extracted, a proof of the method's power. There are, however, two main disadvantages.

The first disadvantage is obvious: due to the complexity of the problem, the computational times are generally long. This problem is particularly severe at long wavelengths because the quiver amplitude of the electron increases, requiring large computational grids. For example, a single intensity calculation for argon near saturation using 2.0 μm, 50 fs pulses takes up to 5 days even on the fastest processor. To make matters worse, for a comparison with the experiment one has to perform hundreds of such calculations at slightly different peak intensities to integrate over the spatial volume in the laser focus. As a rule of thumb the number of calculations is chosen such that between two consecutive intensities the corresponding ponderomotive potentials change by less than a photon energy across the entire intensity range. The intensity range in turn is chosen to assure the convergence of the result. For most practical reasons, between one and two orders of magnitude have to be considered. Using argon again as an example, at $2.0{\cdot}10^{14}$ W/cm^2 with 2.0 μm pulses, the number of calculations can be estimated from $N = U_P/\lambda$, which gives $N = 120$. In our case, computations were performed at The Ohio Supercomputer Center, allowing us to launch as many as 50 such calculations all at once. Another problem stemming from long computational times is the fact that tweaking physical parameters cannot be done on the fly (for example altering the shape of the potential).

The second disadvantage is a bit more subtle and somewhat paradoxical. Because TDSE has all the ingredients, quite often it is hard to distinguish the exact origin of certain effects found in the experiment and the computational results. In the experimental findings chapter we will see an example of this problem when we will discuss the appearance of a low energy feature in the photoelectron spectra in the tunneling regime. Despite these two disadvantages, TDSE is a formidable tool. Its accuracy in matching experimental findings is so remarkable [13] and scientists trust this method to such an extent that 3D TDSE calculations are often used as a benchmark for non-numerical calculations, especially when experimental results are nonexistent or inconsistent.

The 3D TDSE calculations performed by our group were based on the propri-

etary code developed by Professor Harm G. Muller at FOM in The Netherlands [14]. Other codes exist, mostly proprietary, with one notable exception: Professor Dieter Bauer's *Qprop*, an open-source TDSE code available for immediate download at $http://www.qprop.de/$. In addition to the code itself, the website also provides a lengthy manuscript with all the details, both theoretical and numerical. Professor Muller's TDSE was designed in late 90s, when ultrashort mid-infrared pulses were scarce, so that the code was tweaked for 800 nm, the wavelength for the titanium sapphire laser. Additionally, the code was designed only for few atoms (hydrogen, helium and argon) both for numerical (finding realistic potentials eventually becomes a trial and error search) and practical reasons (argon was and still is the main gas used in HHG). A testimony to the fact that the code was designed for 800 nm will be presented in the experimental section when we will uncover a limitation of the code for mid infrared pulses.

We will end our qualitative description of TDSE here, encouraging the reader eager to dive further into this subject to consult the references (an excellent starting point is *Qprop*'s manuscript, available for free download together with the code).

1.3 Photoelectron Spectra - a Photoelectron's Journey from Birth to Detection

In the previous section we saw that both SFA and TDSE will provide at the end of the calculation not only the ionization rate, but also the full photoelectron spectra. This, however, is not the case for ADK, a theory that ends at the outer classical turning point. In this section we will follow the motion of the "ADK photoelectron" after tunneling. This will not only bring ADK closer to the other two methods, but as we will see below, it will also allow us to get a clearer picture about the entire process. In Fig. 1.3 we present a typical electron spectrum in the tunneling regime recorded in our laboratory (argon, irradiated by 2 μm, 50 fs pulses at 200 TW/cm^2) as a function of U_P. In this section, we will provide a brief explanation how the major features of this spectrum arise.

If the ponderomotive potential is not too large, the electron motion can be described by nonrelativistic classical mechanics:

$$\ddot{\vec{\mathbf{r}}}(t) = -\nabla V_C(\vec{\mathbf{r}}) - \vec{\mathbf{F}}(t) - \vec{\mathbf{v}}(t) \times \vec{\mathbf{B}}(t). \tag{1.26}$$

The above expression is quite general and is valid for complex structures such as molecules in arbitrary fields. However, except for numerical methods (such as Monte Carlo) it is not very useful since it cannot be solved exactly. As a consequence, for analytical purposes it is necessary to simplify it further.

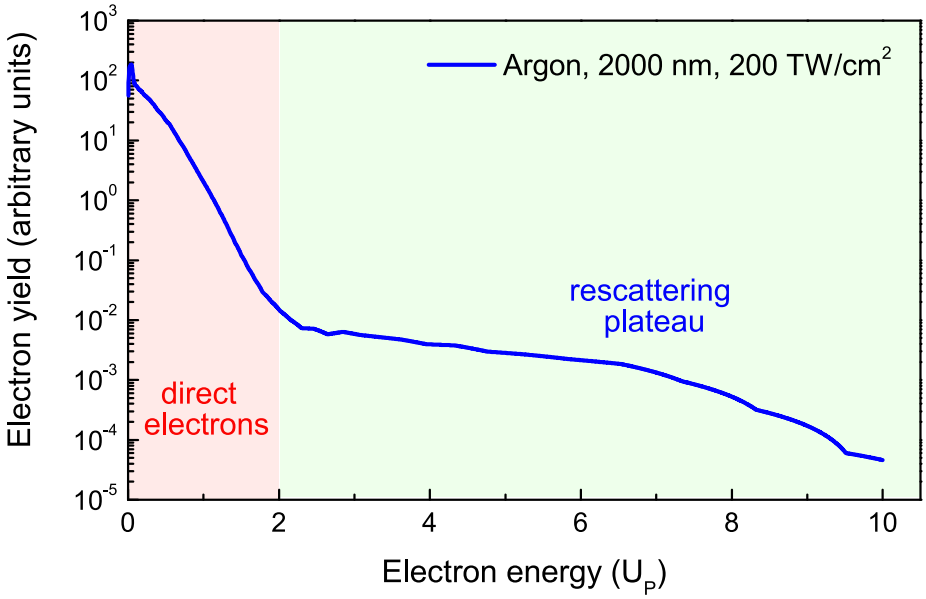

Figure 1.3: **A typical photoelectron spectrum in the tunneling regime.** The red region extending up to $2U_P$ is dominated by the direct electrons, while the blue region extending up to $10U_P$, arises from rescattering (see text for details).

1.3.1 Simpleman's Model

The Simpleman's model was introduced by van Linden van den Heuvell and Muller [15] in 1987. The main idea was to strip the effect of the Coulomb field in Eq. (1.26) as well as the influence of the magnetic field. With these approximations, it can be easily shown from the Hamilton-Jacobi equations that the generalized momentum $\vec{P}(t)$ is a constant of motion:

$$\vec{\mathbf{P}}(t) = \vec{\mathbf{p}}(t) - \vec{\mathbf{A}}(t) \equiv C, \tag{1.27}$$

where $\vec{\mathbf{p}}(t)$ is the electron's mechanical momentum and $\vec{\mathbf{F}}(t) = -\partial\vec{\mathbf{A}}(t)/\partial t$. In the last equation the gauge condition $\phi = 0$ was imposed, with ϕ being the scalar potential. The constant C must be found from initial conditions. By writing Eq. (1.27) from the moment of birth t_{birth} and the moment of detection $t_{detection}$ and assuming the pulse is over at detection (this is a very good approximation, since we're dealing with femtosecond pulses and detection is usually done nanoseconds after ionization) we have:

$$\vec{\mathbf{p}}(t_{detection}) = \vec{\mathbf{p}}(t_{birth}) - \vec{\mathbf{A}}(t_{birth}). \tag{1.28}$$

In Eqs. (1.17) and (1.18) we have given the expression of the ionization rate as a function of the momentum at birth. Remembering that the tunneling rate has a maximum at $\vec{\mathbf{p}} = 0$, we can neglect the first term in Eq. (1.28) and write for the electron's kinetic energy at detection $KE(t_{detection})$:

$$KE(t_{detection}) = \frac{\vec{\mathbf{A}}(t_{birth})^2}{2}. \tag{1.29}$$

This expression is valid for arbitrary polarizations. For linearly polarized light we can take $F(t) = F_0 \sin(\omega t)$ and $A(t) = A_0 \cos(\omega t)$ with $F_0 = \omega A_0$. Finally, introducing the ponderomotive potential U_P, the final energy at the detector in the case of linearly polarized light is:

$$KE(t_{detection}) = 2U_P \cos^2(\omega t_{birth}). \tag{1.30}$$

From the above equation we see that the maximum kinetic energy is indeed $2U_P$, in accordance with the experiment. Furthermore, the low energy electrons are born at the peak of the field ($\sin(\omega t_{birth}) = \pi$), while those near $2U_P$ are born near the minimum of the field. Since the tunneling rate behaves as $\exp(-1/F)$, the electron energy (or momentum) spectrum is expected to have a maximum at zero and decrease exponentially towards $2U_P$. This behavior was indeed observed experimentally [28].

Before we end the presentation of this simple model we should note that during an optical cycle there are two different birth times that give the same final momentum. These two birth times are not identical. If we consider the above equations for the definition of $\vec{\mathbf{F}}$ and take a pulse period from $\omega t = -\pi \rightarrow \pi$ (if the reader is puzzled by negative times we can simply perform a temporal translation) we have:

$$\vec{\mathbf{A}}(t) = \vec{\mathbf{A}}(-t), \quad \text{while} \quad \vec{\mathbf{F}}(t) = -\vec{\mathbf{F}}(-t). \tag{1.31}$$

As a consequence, there are two different trajectories contributing to the same final kinetic energy. Because we treated the electron classically, there are no immediate effects due to this fact. The real world however is always governed by quantum mechanics and as such the electron wave packets launched at t and $-t$ will interfere *at detection*. The two trajectories are nothing else than the two saddle points from SFA introduced earlier. We will further discuss interference effects later in the experimental chapter.

1.3.2 Rescattering Model

In the mid-nineties a more elusive feature was discovered in the photoelectron spectra when atoms were ionized by linearly polarized radiation [16], [17]. It consisted of a long plateau extending up to $10U_P$ (Walker et al. [18]), with a height many orders

of magnitude lower that the maximum at $KE = 0$, as it can be seen in Fig. 1.3. Its explanation was provided by Schafer et al. [19] and shortly after Corkum [20], when it was realized the connection between the $10U_P$ cutoff in the photoelectron spectra and the cutoff in the high harmonic generation spectra.

To explain the plateau, elastic rescattering was introduced, as an extension to the Simpleman's model. The basic assumption is that if an electron revisits the atomic core (considered immobile, point-like and located at $\vec{\mathbf{r_a}} = 0$) it can elastically rescatter under an angle θ preserving its energy (and hence the magnitude of its momentum). Without rescattering, the electron can only gain up to $2U_P$, but if rescattering is allowed, the electron can gain additional energy from the field in excess of $2U_P$ (in essence, rescattering rephases the electron's motion). Assuming again that the electron is born with zero momentum, we can impose that at $t_{rescatter} > t_{birth}$ the electron is at $\vec{\mathbf{r_a}} = 0$, or explicitly:

$$\vec{\mathbf{r}}(t_{rescatter}) = \int_{t_{birth}}^{t_{rescatter}} \vec{\mathbf{A}}(t)dt - \vec{\mathbf{A}}(t_{birth})(t_{rescatter} - t_{birth}) = 0. \tag{1.32}$$

The above equation allows us to find the time of rescattering as a function of time of birth. It can be easily seen that if the polarization of the light is not near-linear, the above condition cannot be satisfied and hence the electron does not revisit the core. This fact is used in the so-called polarization gating technique used to generate single attosecond pulses in HHG [21]. For this reason, we will restrict our discussion to linearly polarized pulses. For a pulse given by $A(t) = A_0\cos(\omega t)$, it can be shown that the above condition is satisfied only for phases from $\pi/2$ to π. We can find the energy at rescattering:

$$KE(t_{rescatter}) = \frac{1}{2}\left[A(t_{rescatter}) - A(t_{birth})\right]^2. \tag{1.33}$$

The maximum of this function is the well known HHG cutoff (without the IP correction) and it corresponds to $3.17U_P$. This maximum occurs at a phase of approximately 1.88 radians or 107°. With the exception of this particular phase, there are at least two birth phases in the interval $[\pi/2, \pi]$ that give the electron the same energy at recollision. Electrons born after 1.88 radians return first, moving along the so-called short trajectories. Those that are born before 1.88 radians, return later along the so-called long trajectories. It can be shown that long trajectories are from $\pi/2$ to 1.88 while the short ones are from 1.88 to π. It is even possible to have more than two returns. For phases above 1.79 the electron returns exactly twice (with the exception of the phase at 1.88 radians), while for phases from $\pi/2$ to 1.79 we have multiple returns. Obviously, all multiple returns correspond to long trajectories. Finally, since

long trajectories are born near the peak of the electric field, they usually dominate (the ionization rate is higher for them).

The $10U_P$ cutoff in the electron spectra can be found if we assume an elastic backscattering event along the laser polarization ($\vec{\mathbf{p}} \rightarrow -\vec{\mathbf{p}}$). In this case the final energy (at detection) will be:

$$KE^{backscatter}(t_{detection}) = \frac{1}{2}\left[2A(t_{rescatter}) - A(t_{birth})\right]^2 \tag{1.34}$$

The maximum at this expression is $10.007U_P$ in accordance to the experiment and it occurs at a phase close to 1.83 which corresponds to a long trajectory.

Just as in the case for the different trajectories that give rise to two different final energies at detection, the long and short trajectories interfere at recollision. These effects are crucial for high harmonic generation but they will not be described here. We should point out that only *one* of the two trajectories that interfere *at detection* will revisit the core, while the other does not. This means that the one that does, it is either a short or a long trajectory, but never both. Which one it is depends on the initial birth phase. There were many HHG experiments performed with the aim of studying these interferences between the long and short trajectories. From the above discussion, one can readily conclude that measuring interferences at detection might provide an alternative (perhaps complementary) way of studying these effects. Up until now, however, the interferences at detection were never observed.

The above discussions are summarized graphically in Fig. 1.4. The figure is for the general case since we used the phase on the coordinate and the momenta were plotted in terms of the maximum value of the vector potential.

So far we have only discussed the first return, either long or short. If one is to include elastic backscattering for multiple returns, it is found that each have different cutoffs in terms of U_P, all lower than $10U_P$ [29].

1.4 Beyond Single Ionization

So far we have only dealt with a single active electron and we uncovered a multitude of effects for this rather simple case. However, this is not the whole story. When the electron revisits the core, its energy can be many times over the ionization potential of that of the parent ion. In these cases, the electron can dislodge multiple electrons, as it was reported by Walker at al. [22]. In Fig. 1.5 (adapted from the above cited source) the measured single and double ionization yields are plotted in the case of helium for 780 nm, 100 fs linearly polarized pulses.

If one is to consider the ADK rate applied sequentially (both electrons are ejected by the field independently), it would underestimate the production of He^{++} by many

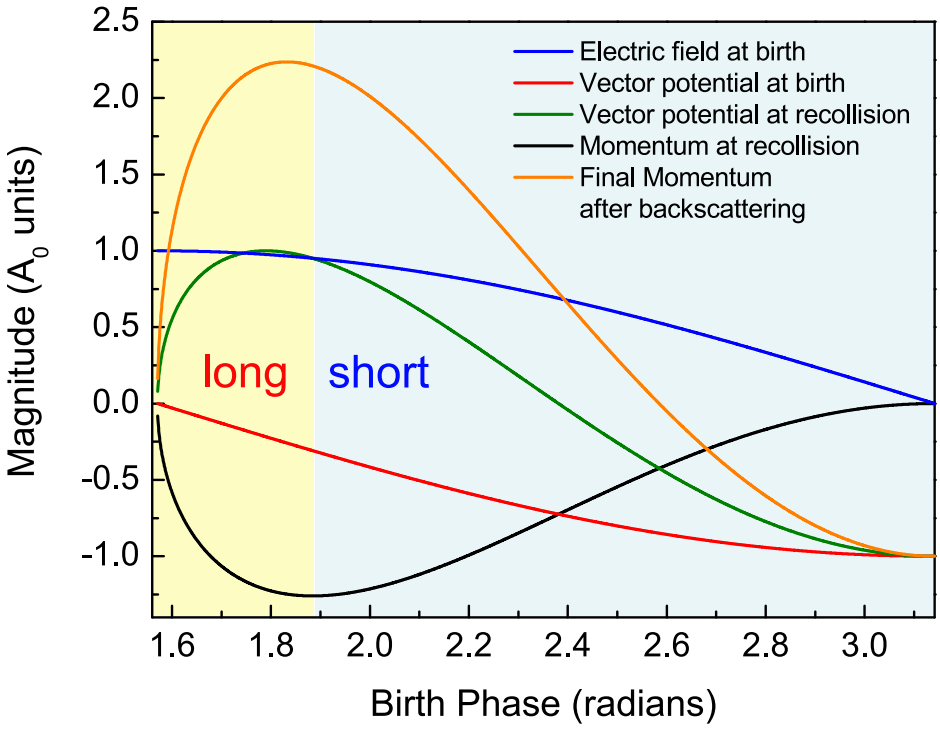

Figure 1.4: **Photoelectron propagation in the continuum as a function of birth phase**. The plots are for a sine, linearly polarized infinite pulse assuming a zero kinetic energy at birth. The shaded areas correspond to the born phases for the long and short trajectories (see text for details).

orders of magnitude (the blue region in Fig. 1.5). The reason for this gigantic discrepancy is the neglect of the effect the first ejected electron has in the ejection of the second. To accurately describe the process, the inelastic $(e, 2e)$ process has to be considered, by allowing the first electron to "donate" part of its energy upon the revisit of the core to the second electron. This process is usually described by introducing the Lotz ionization cross-section. Careful electron-ion coincident measurements have been performed in the past to study this process [23]. The entire process is rather complicated for a brief description since electron correlations play a significant role, to such an extent that even below the classical $(e, 2e)$ threshold (when the returning electron does not have enough energy even to excite the ion) the process is still efficient [24].

For now, we will only take note of this process, keeping in mind that ADK underestimates the rate of ionization when the Keldysh parameter $\gamma \sim 1$, a clear signature

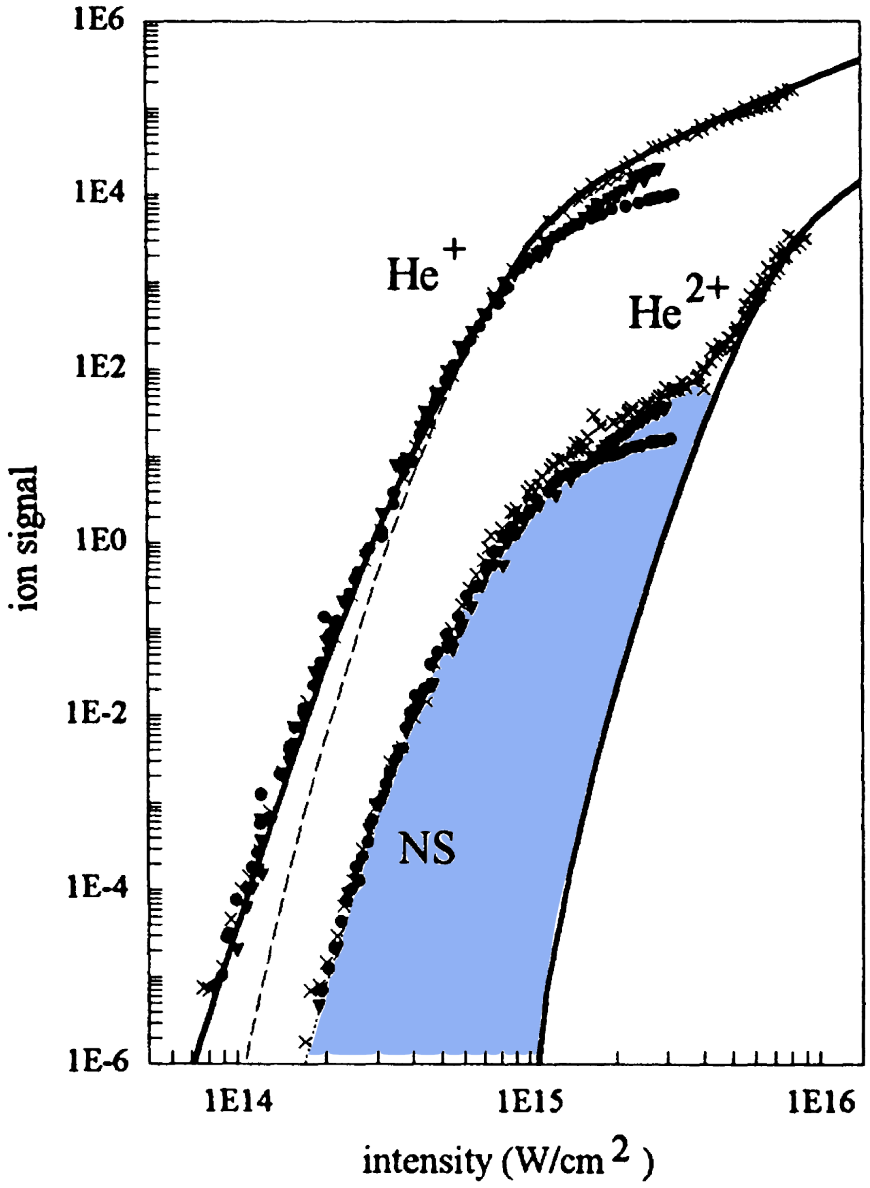

Figure 1.5: **Double ionization of helium.** The dotted line represents the ADK rate calculated for the single ionization, while the solid lines are the TDSE-SAE numerical calculations. At low intensities, the ADK formula does not reproduce the experimental results, due to the onset of multiphoton ionization. The blue shaded area is the inelastic $e, 2e$ enhancement which is also missing from the TDSE-SAE. Figure taken from [22].

of the mixed tunneling-multiphoton regime.

Chapter 2

Experimental Setup

Nowadays, it is common knowledge that physics is an observational science. In more colloquial terms, it is the tool we developed over the millennia to understand how stuff works. We started with the small world around us and through both evolutionary and revolutionary steps we expanded it from subatomic particles to the whole universe and beyond. To achieve all, we replicated the outside world in the lab performing clever experiments, but also developed complex theories and numerical simulations. However, one might also argue that physics is an art in itself. Quite often, the next breakthrough comes not by using the latest technological advances, but by combining existing ones in a new way or viewing things from a different perspective. In this chapter I will describe some of the experiments envisioned and performed in our laboratory.

2.1 Laser Sources

Even before the first laser was built by Maiman [30] in 1960, Gordon Gould, the scientist who coined the term laser, noted in his laboratory notebook that this new tool can be used for spectrometry, interferometry, radar, and nuclear fusion. Today, Gould's prediction came true. The laser has become not only an extraordinary tool for scientists, but also a daily occurrence in modern life.

It is not surprising then that the laser is an essential tool for strong field atomic and molecular physics. Indeed, the development of this field would have been impossible without the emergence of powerful lasers, capable of generating fields comparable to the atomic ones. Taking the hydrogen atom as an example, the electric field generated between the electron orbiting the proton is $E = e/4\pi\epsilon_0 a_0^2 \sim 5 \cdot 10^9\ V/cm$ (this represents 1 atomic unit of field strength), where $e \sim 1.6 \cdot 10^{-19}\ C$ is the electron charge, $\epsilon_0 \sim 8.85 \cdot 10^{-12}\ F/m$ is the vacuum permittivity and $a_0 \sim 0.53\ \mathring{A}$ is the first Bohr radius. To create such a field, an electromagnetic field must deliver in

vacuum an intensity $I = c\epsilon_0 E^2/2 \sim 3.5 \cdot 10^{16}\ W/cm^2$, where $c = 3 \cdot 10^8\ m/s$ is the speed of light. This is not an easy task. Focusing a cw Ruby ($\lambda \sim 694.3\ nm$) with a $f\sharp = 4$ lens produces a transform limited spot of $2.4 \cdot 10^{-7}\ cm^2$ and hence would require the laser to deliver 8.5 GW of power. Such a laser is not only impractical but literally impossible to build. Instead of delivering the energy stored in the gain medium continuously, pulsed lasers dump the stored energy in a very short amount of time, easily achieving such a peak power. In the following I will briefly discuss the three major breakthroughs made over the years in producing such short pulses.

Q-switching

Q-switching was the first method developed to produce short pulses. It was proposed by Gould even before Maiman constructed the first laser. The first experimental demonstration was performed in 1961 by Hellwarth and McClung [31]. It consists of inserting a temporary attenuator inside an otherwise high Q factor laser resonator. When the attenuator is inserted (or on), the gain medium is pumped but lasing cannot occur. This has the effect of dramatically decreasing the Q factor (high loss). When the attenuator is removed (or switched off), lasing takes place and due to the high Q factor the energy stored in the gain medium is quickly released producing a short laser pulse. Typical q-switched lasers operate at low repetition rates (single shot to tens of kHz) and produce hundred nanosecond pulses. These lasers are widely used, but in our experiment they are only applied as pumps for other lasers.

Mode-locking

Mode-locking [32] is a somewhat more subtle technique than q-switching. If a laser resonator allows multiple longitudinal cavity modes that fall inside the gain bandwidth to have fixed phases with respect to each other, then short pulses (soliton formation) will build up. Mode-locking is the technique used to generate ultrashort, few cycle femtosecond pulses in Ti:sapphire oscillators. For a resonator with a $L = 1.9\ m$ cavity length, the spacing between adjacent cavity modes is given by $\Delta f = c/2L \sim 80\ MHz$, where c is the speed of light. Given the enormous bandwidth for Ti:sapphire (over 100 THz), over a million longitudinal modes can build and if dispersion is properly compensated, pulses as short as 5 femtoseconds at 80 MHz are generated. However, the pulse energy is extremely low, typically few nanojoules. Nevertheless, the peak power is quite high (MW) but low enough to prevent damage in the laser crystal. Using again a $f\sharp = 4$ lens like we used above for Ruby, the peak intensity that can be reached with such a laser is $3 \cdot 10^{12}\ W/cm^2$. Although this intensity is enough to study low binding energy atoms, e.g. alkali, it is not enough for hydrogen or other atoms with high ionization potentials. However, it is the best

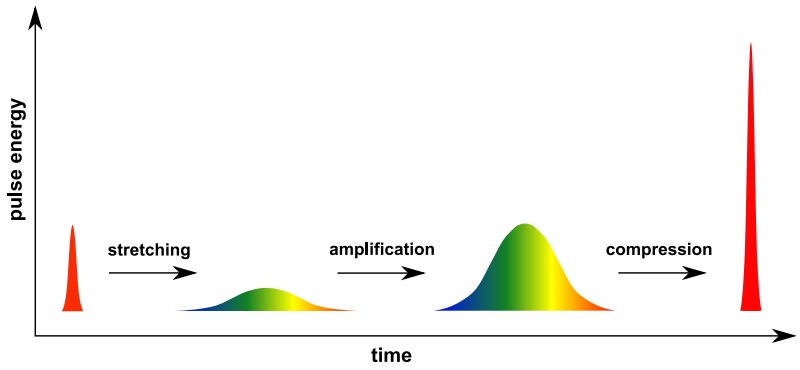

Figure 2.1: **A typical Chirped Pulse Amplification (CPA) system.** Ultrashort pulses from an oscillator are stretched up to a million times and are subsequently amplified and compressed back, generating ultrashort ultra intense pulses.

method to generate the shortest laser pulses and this is extremely useful, if we can somehow amplify them.

Chirped Pulse Amplification

Chirped Pulse Amplification (CPA) is a technique developed at the University of Rochester by Gérard Mourou and Donna Strickland [33]. Although it is not a method to generate ultrashort pulses in itself, it is a technique to amplify them. The basic concept of CPA is presented in Fig. 2.1. A broadband ultrashort pulse from an oscillator is first stretched, by making one side of the spectrum travel a difference distance that the opposite side. After stretching, the pulses are amplified and finally compressed back to their initial duration. With this scheme, depending on the approach, amplification factors of 10^6 were achieved for high repetition (kHz) lasers. For large scale single shot lasers, the amplification factors are much higher, typically around 10^9, generating intensities well into the relativistic domain.

The crucial key in CPA is dispersion management. A complete treatment of dispersion in CPA however, although instructive, is beyond the purpose of this thesis. For a reader eager to study this issue in detail, two excellent review articles by Backus et al. [37] and Walmsley et al. [38] are easily available.

2.1.1 The Tunable Infrared Source

The tunable infrared source is a complex laser system designed to generate ultrashort pulses centered at various mid-infrared wavelengths. Part commercial part homebuilt, it is the workhorse used for most of the results reported in this thesis.

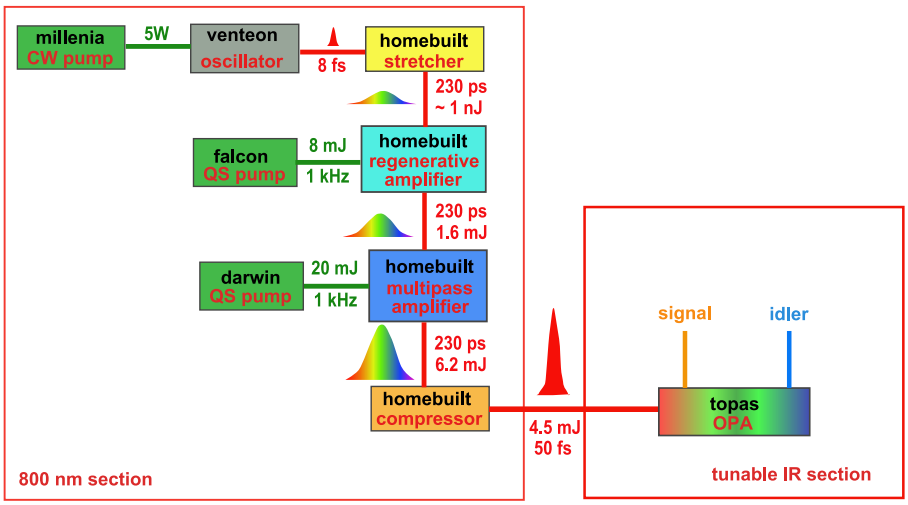

Figure 2.2: **Diagram of the Tunable Infrared System.** It consists of a Ti:sapphire 800 nm section pumping a tunable Optical Parametric Amplifier (OPA). The 800 nm section can also be used independently.

The laser diagram is depicted in Fig. 2.2 and it consists of a CPA Ti:sapphire system operating at 800 nm and a tunable Optical Parametric Amplifier (OPA).

The 800 nm Section

First in the laser chain, the oscillator (Venteon by Nanolayers GmbH) is pumped by a CW Nd:VO_4 laser (Millennia by Spectra Physics) producing 8 fs pulses centered at 800 nm. This corresponds to a bandwidth larger than 200 nm. The repetition rate of the oscillator is 80 MHz and the pulse energy is around 25 nJ. These very short pulses are then stretched up to 230 ps in an all reflective stretcher. A typical stretcher, slightly different than the one used, is depicted in Fig. 2.3. In our setup the stretcher is folded in half by inserting a flat rectangular silver mirror (6 in by 1 in) in the telescope's focal plane, allowing the use of a single grating (Spectrogon, 110 mm by 50 mm and 1200 grooves per mm) and a single curved mirror (8 in diameter, 150 cm radius of curvature). The retro reflector is a rectangular silver mirror (4 in by 1 in). Due to geometrical restrictions, the passing bandwidth of the stretcher is "only" 100 nm, enough to support sub 30 fs pulses.

After stretching, the pulses are amplified in two stages. In the first stage a titanium sapphire based regenerative amplifier, whose diagram is presented in Fig. 2.4, traps and amplifies 1 in every 80,000 pulses, effectively dropping the repetition rate of the entire system down to 1 kHz. This so-called "pulse-picking" is done

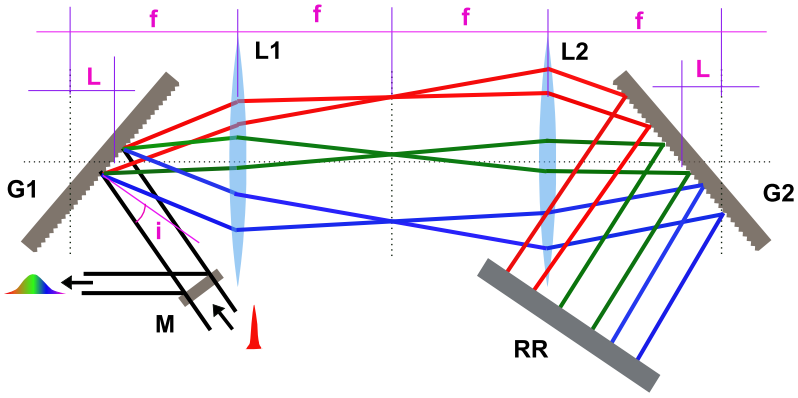

Figure 2.3: **The Stretcher.** The frequencies within an ultrashort pulse injected into the stretcher are spatially dispersed causing them to travel different distances, accumulating different phases. The input pulse accumulates positive dispersion, and therefore the red part of the spectrum travels before the blue, resulting a much longer final pulse with a much lower peak power. G1 and G2 are diffraction gratings, L1 and L2 are convex lenses (of focal length f) forming a 1:1 telescope, RR is a retro reflector and M is the output mirror. L and i are the important stretcher parameters denoting the stretcher length and the input angle. The two parameters determine the stretching factor.

by manipulating the polarization of the light with the use of electrically induced birefringence in a device called Pockels cell. The regenerative amplifier is pumped with 120 ns, 8 mJ, 527 nm pulses generated by a flash lamp driven Nd:YLF Q-switched laser (Falcon 527 by Quantronix). To ensure optimal contrast between the main pulse and the pre-pulse and the post-pulse, the regenerative amplifier's cavity length almost matches that of the oscillator (an exact match would lead to an unwanted coupling between the two cavities, making the oscillator unstable). This way one and only one pulse is trapped and amplified at any given time. After the regenerative amplifier, the 800 nm chirped pulses are amplified from the nJ level up to 1.6 mJ. Due to the optics used inside the regenerative amplifier, primarily the Pockels Cell and the two polarizers, but also due to gain narrowing, the final pulses have a bandwidth of 21-22 nm, enough to support 50 fs pulses.

The second amplification step takes place in a multipass amplifier, also based on the titanium sapphire technology (Fig. 2.5). The pump is a diode driven 527 nm Nd:YLF Q-switched laser (Darwin by Quantronix) producing 120 ns, 20 mJ pulses. The pump pulses are split in half and each is used to pump one side of the liquid nitrogen cooled Ti:Sapphire crystal. Although the Ti:sapphire can be cooled effectively with liquid water at room temperature, cryogenic cooling was chosen to suppress

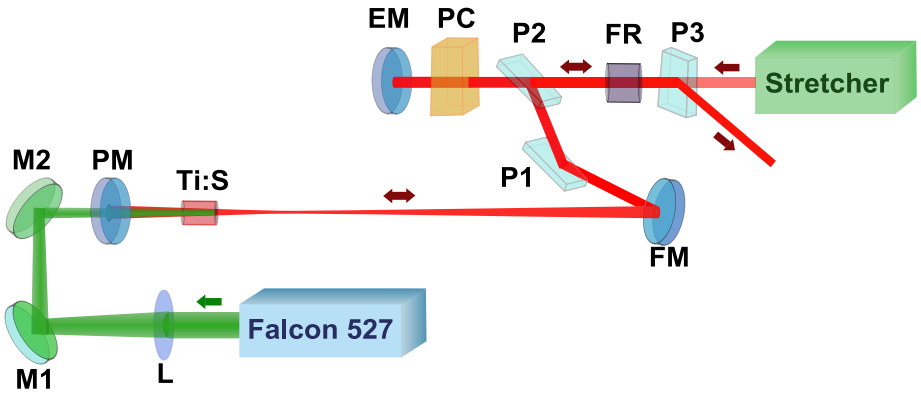

Figure 2.4: **The Regenerative Amplifier Diagram.** P1, P2 and P3 are polarizers, FR is a Faraday rotator which together with P3 form an optical insulator, PC is the Pockels Cell, EM is the end mirror, FM is the fold mirror, Ti:S is the laser rod and the PM is a dichroic pump mirror. The 527 nm pump pulses from the Falcon 527 are focused by the lens L and sent into the laser cavity by the steering mirrors M1 and M2.

thermal lensing effects. To prevent condensation of atmospheric water vapors, the crystal sits in a high vacuum chamber, whose low pressure (10^{-8} Torr) is kept with a small, vibration-free ion pump (StarCell by Varian). Because only two passes are necessary to deplete the gain medium in this design, no significant gain narrowing is observed. Also due to the fact that only two passes are required, the dispersion accumulated in the multipass is significantly lower than the one in the first stage. Beam quality however, in general is somewhat lower in multipass amplifiers compared to regenerative amplifiers because the first is not a cavity while the latter is. In the end, after two stages of amplification, 6.2 mJ pulses are generated.

After amplification, the pulses have to be compressed back by flattening the spectral phase. This is done in the compressor, as illustrated in Fig. 2.6.

Because the pulse has accumulated additional dispersion during the amplification, the compressor has to compensate this extra phase as well. However, this is not possible if the compressor is built with gratings whose groove density is the same with the one in the stretcher. Using mismatched gratings between the stretcher and compressor, adequate phase compensation is possible [34]. In our case the two compressor gratings (Spectrogon, dimensions 64 mm by 64 mm and 140 mm by 120 mm) have a groove density of 1500 grooves per mm. Properly adjusting the compressor parameters (the input angle i and the separation between the gratings L) through an iterative process monitoring the final pulse duration as well as the spectral phase with a frequency resolved optical gating (FROG) apparatus (citation

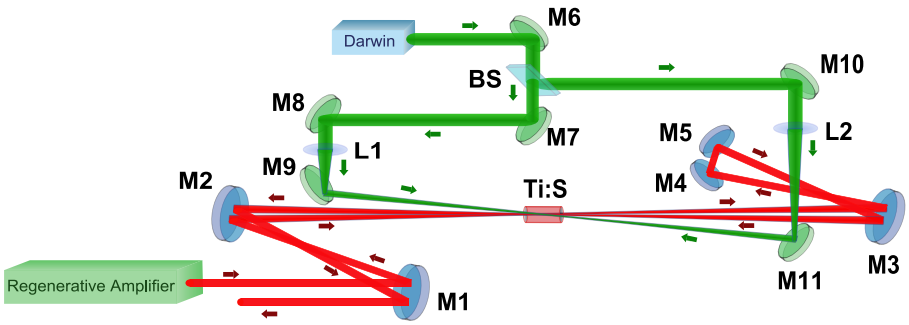

Figure 2.5: **The Multipass Amplifier Diagram.** M1 to M11 are flat mirrors, BS is a 50-50 beam splitter, TiS is the cryogenically cooled laser rod and L1 and L2 are the pump focusing lenses. To assure a uniform pumping of the laser rod, the pump is split in two, pumping symmetrically the crystal.

here), we obtain 50 fs, 4.5 mJ near transform limited pulses. The seemingly low compressor efficiency is due to the fact that four grating bounces with around 92% efficiency each are needed. Such grating efficiencies are typical for holographic pulse compression gratings and they slowly degrade with time as dirt is slowly accumulated on them. We have tried to clean old gratings with ozone (generated in air by placing a UV lamp few inches in front of the grating) with limited success. A better method used to clean old gratings is to pour warm distilled water and then methanol along the grooves and at the end use high purity nitrogen to dry the methanol. Repeating several times this procedure, we successfully recovered the original grating efficiency.

The Tunable Infrared Section

The tunable infrared section is a commercial optical parametric amplifier based on difference frequency generation (TOPAS-HE, by Light Conversion). Difference frequency generation (DFG) is a nonlinear optical process that takes place in crystals that lack inversion symmetry (such as beta barium borate, commonly known as BBO). The process takes place as follows: the most intense beam with the most energetic photons, called the pump, is mixed (overlapped in time and space) inside the nonlinear crystal with another beam whose photons have a longer wavelength, called the signal, generating a third beam with even longer wavelength photons, called the idler. In effect, the crystal splits a photon from the pump in two photons, one in the signal and one in the idler. Conservation of energy requires that the sum of the frequencies of the signal and idler equals the frequency of the pump:

$$\omega_{signal} + \omega_{idler} = \omega_{pump}. \tag{2.1}$$

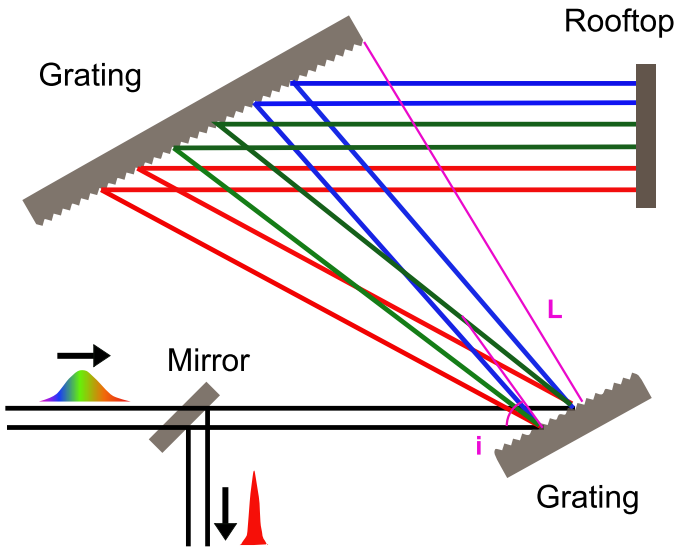

Figure 2.6: **The Compressor.** Essentially a stretcher in reverse, it is comprised of two gratings and a rooftop retro reflector. The input angle i and the compressor length L determine the phase accumulated by each individual color that contained in the input pulse.

Because DFG is a $\chi^{(2)}$ process (where χ is the usual susceptibility), the conversion increases linearly with the intensity of the pump, so to be efficient, the intensities involved are quite high. Additionally, it is desired to chose crystals with large nonlinear responses (the well-known d_{eff} coefficient, quantifying the magnitude of the response, must be as large as possible). Finally, to assure that there is no slippage between the electric fields of the pump and the signal over the length of the crystal, the crystal is cut and oriented in such a way that the idler photons generated at different positions inside the crystal add coherently. This is called phase-matching condition and is given by:

$$\cdot\vec{k}_{signal} + \cdot\vec{k}_{idler} = \vec{k}_{pump}, \tag{2.2}$$

This condition is usually satisfied using the birefringence of the crystal, aligning the polarizations of the three beams along the ordinary and extraordinary axes. Depending on which beams are along the ordinary and extraordinary axes, different types of phase-matching exist. For negative uniaxial crystals, such as BBO, one can have Type-I phase-matching (pump is along the extraordinary axis and both the signal and the idler along the ordinary axes), Type-IIA (pump and idler along the extraordinary axis and the signal along the ordinary axis) and finally Type-IIB (pump and

signal along the extraordinary axis and the idler along the ordinary axis). In Type-I the polarizations of the signal and idler are parallel, while in both Type-II they are perpendicular. In the case of our tunable optical parametric amplifier, Type-IIB phase-matching is employed. For a rigorous treatment of nonlinear processes, the reader is encouraged to consult the numerous books readily available, such as Robert W. Boyd's "*Nonlinear Optics*" [39].

So to generate a tunable source, starting with a non-tunable pump and signal is obviously not enough, according to Eq.2.1. So far, we only have a non-tunable pump operating at 793 nm, which was described in the previous section. In principle at least, due to the large bandwidth of the oscillator, one can attempt to tune the wavelength in the regenerative amplifier by adjusting the Pockels cell (voltage and angle of its crystal). This method is in fact used in our laboratory on a different system, whose titanium sapphire section lases at 815 nm, on the red side of the peak of the gain curve. An alternative method is to use a part of the pump to generate an ultra broadband spectrum at lower frequencies. Then, one can pick the desired portion of this newly generated light and use it as the signal.

One of such processes, capable of generating huge bandwidths, is superfluorescence (another is white light continuum generation). Superfluorescence is a quantum optics process in which atoms excited by the pump start fluorescing *coherently*. This is possible because the electric dipoles induced by the strong pump in *all* atoms become coupled, so that when de-excitation takes place, the photons released from adjacent atoms add coherently. Because no seeding pulse is used in this process, the superfluorescence spectrum arises from quantum noise (similar to spontaneous emission). This is the reason why the spectrum changes significantly from shot to shot, with strong modulations. From a practical point of view, a word of caution is in order here: because very high intensities are needed to initiate superfluorescence (otherwise we will only have the standard fluorescence through spontaneous emission, an incoherent process) great care is needed when this technology is deployed. For example, in the case of BBO, superfluorescence takes place efficiently around 50-60 GW/cm^2, while the damage threshold is around 80 GW/cm^2, with white light continuum generation (WLCG) somewhere in between. At a first look, there seems to be enough slack between superfluorescence and permanent damage (good BBO crystals can easily cost few thousand dollars), but peak to peak pulse fluctuations, mode hoping or transient phenomena can easily cross the damage threshold. In addition, just like people, no two crystals are the same and the damage threshold level quoted above should be taken as an average number, not an absolute one. Since WLCG lies between superfluorescence and the damage threshold, after three years of extensive use we still have the original BBO crystal intact, by carefully controlling an aperture in the pump every time WLCG was observed (which is the case on a daily basis if the 800 nm section works perfectly).

After this short excursion into the realm of quantum optics, for the attentive reader it is probably obvious how the tunable mid-infrared laser works. The 793 nm pump beam is split in two, with the first, weaker portion of it being used in a first stage (Fig. 2.7) to generate the tunable signal by superfluorescence, while the stronger portion of the pump is being used in a second stage (Fig. 2.8) to difference frequency generate the tunable idler using the signal from the first stage.

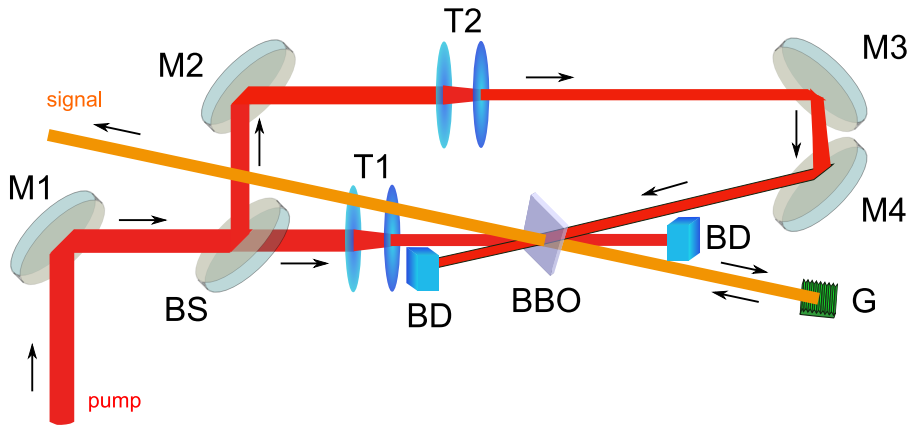

Figure 2.7: **Diagram of the superfluorescence section in the TOPAS.** The optics in the figure are mirrors (M1-4), beam splitter (BS), telescopes (T1, T2), beta barium borate nonlinear crystal (BBO), motorized diffraction grating (G) and beam dumps (BD). The 793 nm pump beam (red) is split in two. The first portion is used to generate broadband superfluorescence. The second portion of the pump is then used to amplify the spectral window selected by the motorized grating, generating a strong signal. This second passage is based on difference frequency mixing, so an idler is generated along with the signal. However, after the passage through a thick calcite window (not shown), the signal and idler become separated in time, and only the signal will be used in the final section of the laser.

The superfluorescence section is in practice a bit more complicated. There are a total of five passages through the nonlinear crystal and the pump is actually split in three. The reason for this additional complexity is not only that a single pass is not capable to generate enough signal, but also because as mentioned before, the superfluorescence spectrum has considerable modulation for a single pass. Therefore, the first pass, that generates superfluorescence, is actually three passes, designed to flatten the spectrum. Only after these three passes the superfluorescence spectrum see the motorized diffraction grating, which selects the required color for the next two passes, where it is amplified through, what else, DFG. After the fifth pass, around

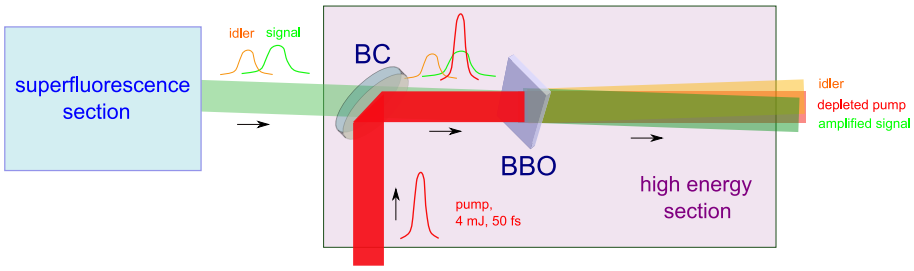

Figure 2.8: **Diagram of the high energy section in the TOPAS.** The optics in the figure are the beta barium borate nonlinear crystal (BBO) and the beam combiner (BC). The pump (red) and the signal (green) are overlapped in the BBO, generating the strong idler (orange) and the strong signal. The geometry used in the original setup was collinear, but this was later modified to a slightly non collinear geometry, as depicted here. This allows to spatially separate the two beams approximately 4 meters after the output of the laser. Because the pump gets severely depleted, it is no longer usable after this stage.

40 μJ of signal plus idler (remember that the last two passes are DFG, so an idler is generated along with the amplified signal) are collinearly generated. Because the signal and the idler are also overlapped in time, they are passed through a thick calcite window before being sent in the second section, that separates them by 1 ps.

The first commercial OPA by Light Conversion was called TOPAS and it had only the superfluorescence section, while our model has the second, high energy stage, and is called TOPAS-HE. In this second stage, the part of the pump that was not used in the first section (only 5% is used in the first stage, so most of the pump is used in this second stage) is temporally overlapped with the signal generated in the first section. Through DFG, not only is the signal amplified, but it also produces a very strong idler (this idler is "fresh", since it has nothing to do with the idler generated in the superfluorescence section). Since the signal is tunable (by moving the grating and the BBO angle in the first section), so is the idler generated in the last section. The signal covers the range 1200-1600 nm, while the idler covers the range 1600-2300 nm. The upper limit for the idler is due to the fact that BBO starts absorbing radiation above 2300 nm. Near the degeneracy, where both the signal and the idler have 1600 nm, their spectra overlap, and since for Type-II phase-matching the two are orthogonal, it is not recommended to be used at this wavelength (the polarization in the two can behave erratically from shot to shot). In the end, we obtain for the signal pulses around 1 mJ, and for the idler around 550 μJ. In the previous sentence the word "around" was used not because we cannot measure very well the energy of

these pulses, but because the numbers are a function of the chosen wavelength. The pulse durations for both the signal and the idler are very close to that of the pump (50 fs), due to TOPAS's low dispersion design. This was confirmed experimentally by comparing the autocorrelation traces for the pump and the idler at 2 μm.

The Performance of the Laser Chain

To maximize, monitor and characterize the overall performance of the laser chain, several beam measurements were performed (Fig. 2.9).

For pulse durations, depending on the wavelength, we used either a FROG technique (793 nm) or single-shot autocorrelators (793 nm and 2 μm). These are direct, optical pulse duration measurements. However, the pulse duration was indirectly determined, albeit with more uncertainty, from estimating the intensity of the focused beams looking at photoelectron spectra. This second method should not be used to obtain hard, quotable numbers, but since in practice pulse durations are not performed on a daily basis, looking at photoelectrons allows one to determine if there is something wrong with either the pulse duration or the beam quality (focusability) of the pulse. According to our direct measurements, the pulse durations for all three beams (pump, signal and idler) are within 10% at 50 fs and are determined by the pulse duration of the pump alone.

Also depending on the wavelength, the focusability was measured with CCD (charge-coupled device) cameras (if the energy of the photon was larger than the energy gap in these silicon-based devices) or thermal cameras (for longer wavelengths). By scanning the focus, we determined that the M^2 for the 793 nm was below 1.1, while for 2 μm it was around 1.5. At the focus, both beams are Gaussian (see Fig. 2.9). If hot spots would be present in the pump, this would necessarily lead to poor performance of the OPA, not to mention the possibility of damaging the crystals, as discussed before.

In addition to pulse durations and beam quality, we also measured peak to peak fluctuations and beam stability in time. These are important quantities, especially for the pump. Because six passes through two nonlinear crystals are necessary to generate the tunable infrared pulses, it is crucial that the pump is well behaved. We determined that the peak to peak fluctuations at the end of the titanium sapphire chain are below 3 %, while the long term stability, once the laser is warmed up, is better than 0.5 % RMS (relative root mean squared). For the infrared pulses, the peak to peak fluctuations are below 6 % and the RMS is around 0.7 %. At first look, the numbers for the infrared pulses are better than expected, since once expects peak to peak fluctuations roughly six times worse than the ones for the pump after six passes through the nonlinear crystal. This is not the case, however, since most of the passes are driven into saturation.

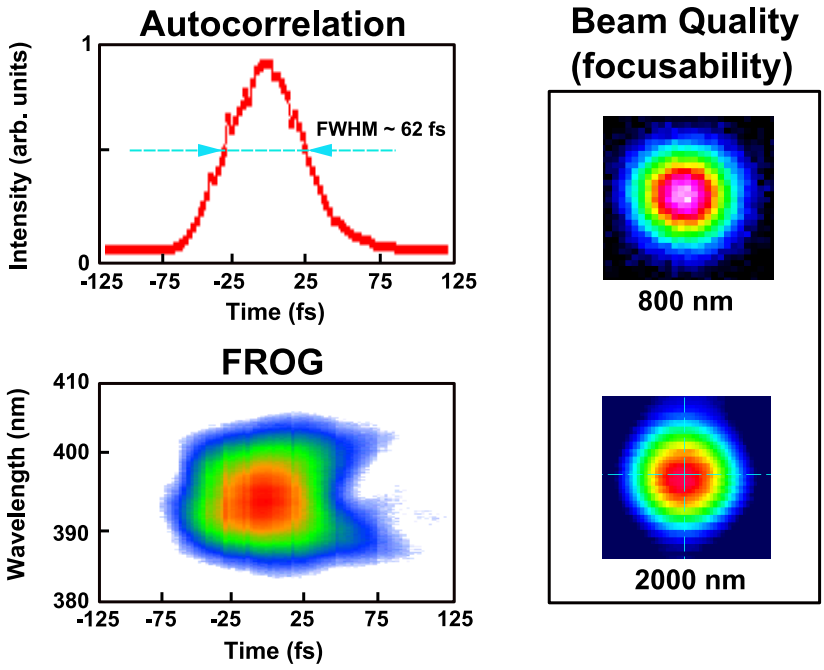

Figure 2.9: **Performance parameters of the laser chain.** Upper left panel: the autocorrelation trace for the 793 nm pump beam. For a Gaussian beam, it corresponds to a 44 fs pulse. Bottom left panel: the FROG trace for the same beam. The round shape signifies a near transform limited pulse (wings are a signature of third order dispersion). Right panel: Spatial beam quality for the pump (793 nm) and idler (2 μm). The idler image was not imaged directly, due to the large pixel size for the thermal camera. A $\times 25$ magnification imaging system was used instead.

In general, the entire laser chain is robust and dependable on a daily basis. Due to its relative complexity and large size, it is fully usable after 4-5 hours of warm-up time. In our laboratory, two other laser systems of similar complexity (of which one is fully commercial), have comparable warm-up times. It is truly a state of the art laser, capable of driving in saturation every atom or molecule, for any wavelength, generating peak intensities in excess of 10^{15} W/cm^2 using not so powerful lenses ($f\sharp = 4$).

2.1.2 Other laser sources

Two other laser systems were used to obtain some of the results presented in this thesis. Since one is fully commercial and one closely resembles the near-infrared

system described in detail above, I will only give a brief description of the two.

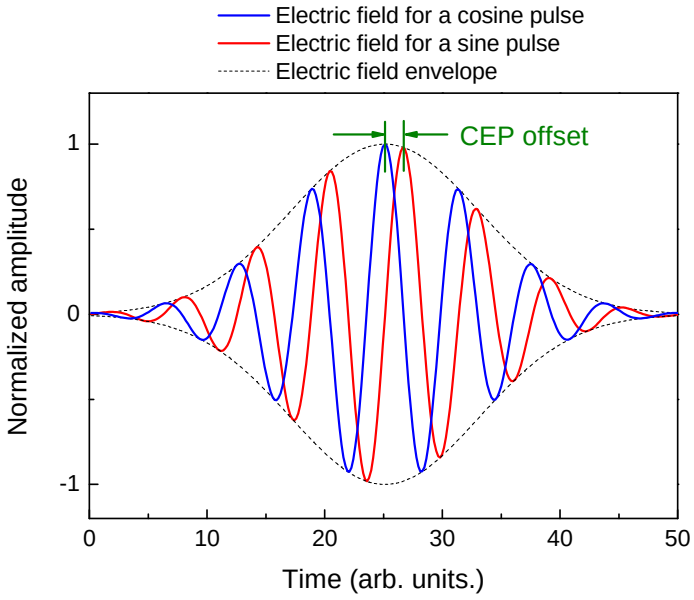

Figure 2.10: **Definition of the carrier envelope phase (CEP).** The CEP is defined as the phase offset between the maximum of the pulse envelope (dashed black curve) and the maximum of the electric field under the envelope. For a cosine pulse (blue) this phase is 0, while for a sine pulse (red) it is $\pi/2$. For very long pulses, with many cycles under the envelope, this phase does not manifest itself in experiments.

The first is a commercial CPA system based on titanium sapphire (Femtopower by Femtolasers GmbH). It consists of an ultra broadband oscillator, a stretcher, a 9-pass amplifier and a compressor. It operates at 3 kHz and it produces 0.8 mJ, 30 fs pulses at 800 nm. What makes this laser system special is the fact that it has an active carrier envelope phase mechanism. For few-cycle pulses, the carrier envelope phase (CEP) is an important quantity, designating the offset between the envelope of the pulse and the instantaneous electric field (see Fig. 2.10). Since for the data presented in this work the stabilization feedback loop was not turned on, I will not discuss here how this is accomplished. It is worth mentioning though that in the last few years there's been a flurry of reports in the literature, primarily concerning high harmonic generation, about experiments where the effect of the CEP plays a crucial role (see the review article by Krausz and Ivanov [35]). As we will see below, other schemes exist to stabilize the CEP, a quantity that in general fluctuates uncontrollably from shot to shot. Finally, for long pulses, with tens of cycles under the envelope,

this quantity basically loses its meaning as it does not manifest itself in experiments. A more detailed description of this laser is readily available at the manufacturer's website.

The third and last laser system whose photons were used in the present work is another DFG laser system. The pump is a 815 nm titanium sapphire system, virtually identical in design with the 800 nm section of the near infrared system described above. However, its signal is not generated using the pump, but it consists of a synchronized Nd:YLF system, operating at its fundamental frequency (1053 nm). The two beams are combined in a KTA crystal (potassium titanyl arsenate), generating via different frequency mixing in a non collinear geometry 3.6 μm pulses. The mid-infrared pulses have 120 μJ and 90 fs, with very good beam quality, producing $1.5{\cdot}10^{14}$ W/cm^2 with an $f\sharp = 4$ lens. For an excellent description of this system the reader is encouraged to consult the excellent dissertations of Dr. Philip Colosimo and Dr. Anne-Marie March, two alumni of our research group.

2.1.3 Generation of Few-cycle, Phase-stabilized Mid-infrared Pulses

If generation of few-cycle pulses is possible in carefully designed oscillators (our Venteon is such an oscillator, producing 3 cycle pulses), amplifying them across the entire bandwidth is almost impossible. To the best of my knowledge, no CPA laser system to date is capable of putting back together a 3-cycle pulse after amplification. The two reasons behind this fact are dispersion and to a lesser extent gain narrowing. For example, a Gaussian 3-cycle pulse centered at 800 nm has a total bandwidth (estimated roughly at three times FWHM) of 375 nm. Even propagating in air such a pulse will suffer temporal broadening (chirping). After 10 m, its pulse duration is more than 40 fs, an increase by a factor of 5. To make matters worse, diffraction disperses the pulses even in vacuum, causing the center portion of the beam to become bluer and bluer during propagation. Today, the best millijoule level CPA titanium sapphire systems can only produce (manage) near transform limited pulses with 15-20 fs FWHM.

Immediately, it is obvious that such systems lack the necessary bandwidth to support few cycle pulses, even with the proper phase management. To solve this problem, nonlinear processes in self-guided filaments are used [36]. These filaments are created when the laser is weakly focused in a gas. At some point, as the beam is focusing down, a critical intensity is reached that prevents the beam from focusing further. The reason behind this is plasma defocussing, and it takes place because the beam starts to ionize the gas (typically through multiphoton ionization). The gas at the center of the beam is ionized more that at the edge of the beam, and since

the plasma has a smaller index of refraction than the neutral gas, in effect the beam creates its own negative lens. However, if this would be the whole story, filaments would not be created, as plasma defocussing would always win. Another process takes place at the same, a process we mentioned in how mode-locking is achieved: the Kerr effect. This effect is due to the fact that the nonlinear index of refraction depends on the intensity. If this index is positive, the center of the beam, where the intensity is higher sees a larger index of refraction than the edge of the beam. The net result is a positive lens due to the Kerr effect. When the two lenses from the two processes are compensated, the beam is not focusing nor defocussing. Instead, it moves along a so-called self guided filament. These filaments are truly spectacular, reaching lengths on the order of kilometers (!) in some cases [40].

But how is the bandwidth increased, since lenses usually don't create new colors? As it turns out, the one based on the Kerr effect does. Since the nonlinear index of refraction also depends on time through the intensity, it necessarily generates new colors (the reader can easily check this by taking the time derivative of the time dependent phase). This nonlinear effect is called self-phase modulation (SPM) and it is at the origin of spectral broadening. Because the new colors are generated by the change in the instantaneous phase of the original colors, the phase relationship between the new and old colors is preserved. Without preserving this relation between the original colors and the newly generated ones filamentation would not provide a way to generate few-cycle pulses. However, dispersion is always present (what else is new?) and after the filament additional dispersion management is necessary, usually using chirped mirrors. These mirrors have a specially engineered thick dielectric stack so that different colors penetrate to different thicknesses before being reflected back, so that these devices are in effect miniaturized stretchers or compressors. As a final word, it is worth mentioning here what causes filamentation to end. In practice, various mechanisms cause losses, and when these losses become large enough, the balance between focusing though Kerr effect and plasma defocussing can no longer be achieved and filamentation ends. Additionally, instabilities in the medium can cause filament breakup, creating multiple filaments (which in general are unstable since themselves were cause by transient instabilities). This is a problem usually encountered with filaments launched over large distances in air.

A typical setup for creating and characterizing such filaments is depicted in Fig. 2.11 and it was previously used to spectrally broaden and temporally compress 800 nm pulses [41]. In our case [42], we focused the 5 mm diameter 2 μm pulse with a weak 1 m radius of curvature silver mirror in a xenon filled glass tube at 1 to 2 bars. For 800 nm the working gas was argon, but because the photons at 2 μm are weaker, we were forced to use the much more expensive xenon due to its lower ionization potential. This was necessary because the minimum number of photons required for multiphoton ionization of xenon at 2 μm is around 20, large even compared to

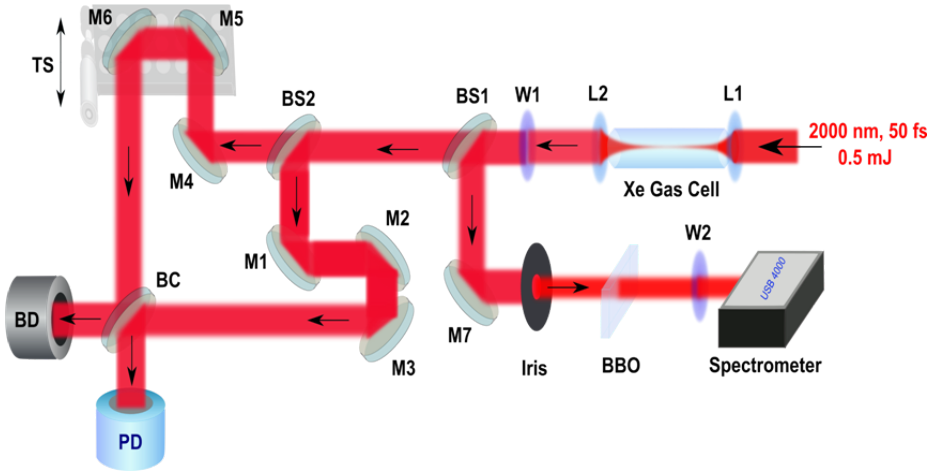

Figure 2.11: **Filamentation setup for infrared pulses.** Pulses from the OPA are weakly focused with the lens L1 into a xenon filled glass tube and recollimated with the lens L2. After the beam splitter BS1 part of the beam is sent into a Michelson interferometer (left) and part into a f-2f spectral interferometer (right). The role of each section is described in the text. The remaining elements are mirrors (M1-7), various windows or notch filters (W1,2), beam combiner (BC), translation stage (TS), photo diode (PD), beam dump (BD) and a beta barium borate nonlinear crystal (BBO).

the minimum number required for argon at 800 nm (10). This was also the reason why our working pressure was 2-3 times higher than in the other case. Despite all this, enough ionization was driven to generate a filament about 5 cm in length (the exact length depends on the pressure). Although this filament length is a far cry from the few kilometers cited above, the spectral broadening of the pulse was truly amazing. At the input of the tube we had invisible mid infrared light, while at the output a bright, beautiful white spot resembling a small LED was observed. In effect, filamentation broadened the spectrum to two octaves (!), in theory capable of supporting a pulse with a pulse duration at the quantum limit (1 cycle). The output energy after filamentation was 270 μJ.

To investigate the behavior of the spectrally broadened pulse, after the glass tube the light was split in two beams, one used to measure the power spectrum and pulse duration in a Michelson interferometer/autocorrelator, while the other was used to measure the spectrum directly in a regular spectrometer. Additional dispersion control is usually necessary for light coming out of filaments, but at the time due to a lack of commercially available chirped mirrors we were limited to use thin windows of various materials, some with positive dispersion (germanium) some with negative

dispersion (fused silica).

As mentioned above, for the spectral measurement two different methods were employed. The first method used was a direct spectral measurement, using a mid-infrared spectrometer, whose linear array is made of extended InGaAs, a material with a linear (single photon) response from 1.2 μm up to 2.5 μm. To calibrate the spectrometer (in wavelength), several pen lamps (Hg, Kr and Xe) as well as a red helium-neon laser (633 nm) and the green (527 nm) from the pump laser was used, the last two diffracted in higher orders. The second method was based on an interferometric measurement that was taken using a Michelson design and a linear InGaAs photodiode. The result of this second method, taken from [42] is presented in Fig. 2.12.

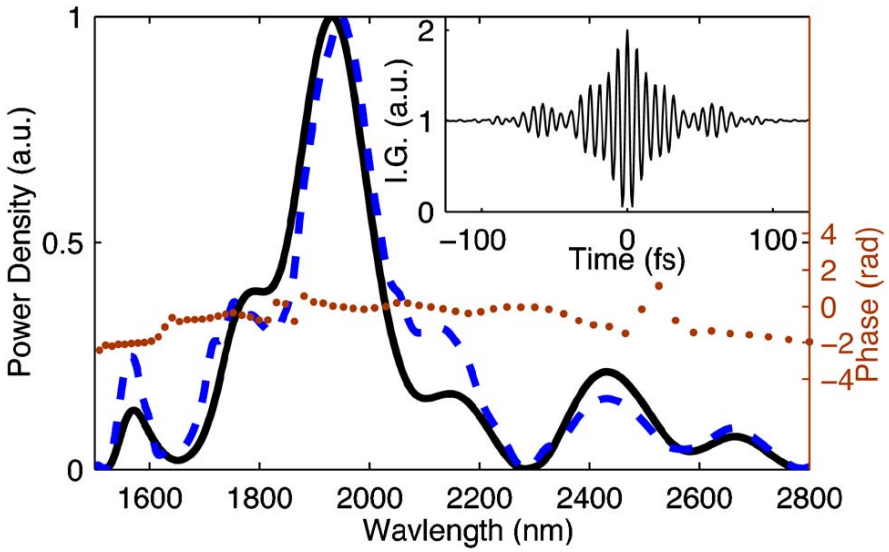

Figure 2.12: **Power spectrum after the 2 μm filament.** (from [42]) The power spectrum (solid black) was measured from the measured interferogram (inset), while the best fit power spectrum (dashed blue) and the best fit spectral phase were calculated in conjunction with the autocorrelation trace by the PICASO adaptive algorithm (see text for details).

The autocorrelator was the same Michelson interferometer, while the nonlinear element necessary for the autocorrelation was the detector itself, the same InGaAs photo diode. At first sight, the InGaAs photo diode could not be used to measure an autocorrelation trace, since it has a linear response to the 2 μm photon (its band gap is smaller than the photon energy, and hence a single photon is enough to promote electrons from the valence band to the conduction band). However, it was shown

before that if driven well into saturation, the photo current will have a small, but measurable two-photon component that can be used to perform the autocorrelation [43]. The result of the best autocorrelation trace is presented in Fig. 2.13, also reproduced from [42].

Combining the power spectrum with the autocorrelation trace and using the PICASO method, based on an adaptive genetic algorithm [44], the pulse duration was estimated to be 17.9 fs, while the transform limited pulse based on the power spectrum was estimated to be 12.2 fs. Although the measured pulse duration is 50% off from the transform limit, it is still a remarkable short pulse (less that 3 cycles), suggesting that after the filament the pulses are self-compressed (one has to remember that our few-cycle oscillator puts out 8 fs pulses centered at 800 nm, which is slightly more that 3 cycles at this wavelength).

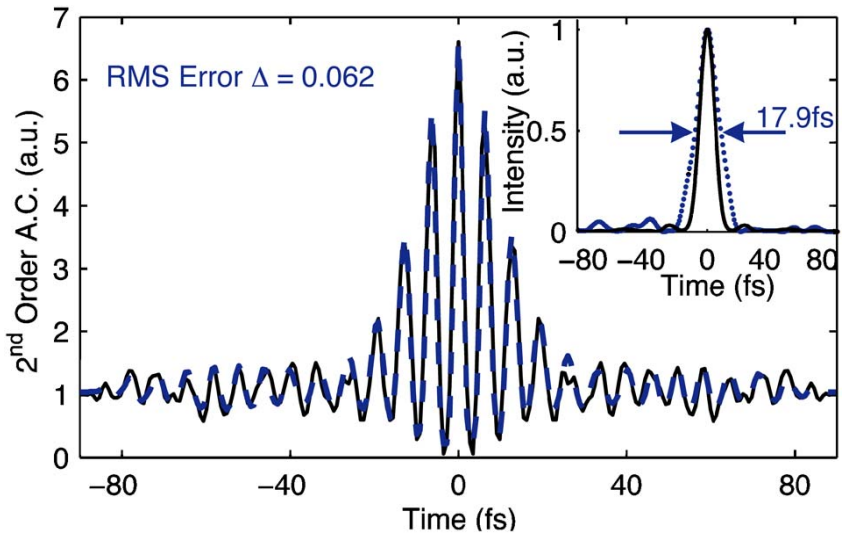

Figure 2.13: **Autocorrelation of the 2 μm pulse after the filament.** (from [42]) The measured trace (solid black) was used in conjunction with the spectrum from the interferogram is compared with the autocorrelation from the PICASO algorithm (dashed blue). Inset, transform-limited intensity profile (solid black) and best-fit intensity profile (dashed blue).

During the first few days of accomplishing filamentation at 2 μm, while literally playing with the white light of the beam, a remarkable characteristic of the idler was discovered: passive carrier envelope phase stabilization. In short, we put the white light (visible) part of the spectrum into a USB spectrometer capable of seeing in the 550-1100 nm range, and to understand its behavior we inserted various optics into the beam and look at the resulting spectrum. At first, when the white light was coupled

in, the spectrum was smooth across the entire range of the spectrometer, testimony of the fact that white light has all visible colors in it (as opposed of being generated by HHG, for example). However, when a doubling crystal (BBO, 0.5 mm thick and 1 by 1 cm) was inserted and angle tuned to maximize the frequency doubling of the 2 μm part of the spectrum (and hence generating light at 1 μm), stable modulations were observed in the spectrum when overlapped with the 1 μm generated in the filament, as it can be seen in Fig. 2.14. In effect, this is a f-2f spectral interferogram [45]. Quickly, it was realized that the only way possible for this phenomenon to occur is if the fundamental light that generated the filament (the 2 μm idler from the TOPAS) was CEP stabilized itself (the f-2f technique is a standard way to actually measure the CEP).

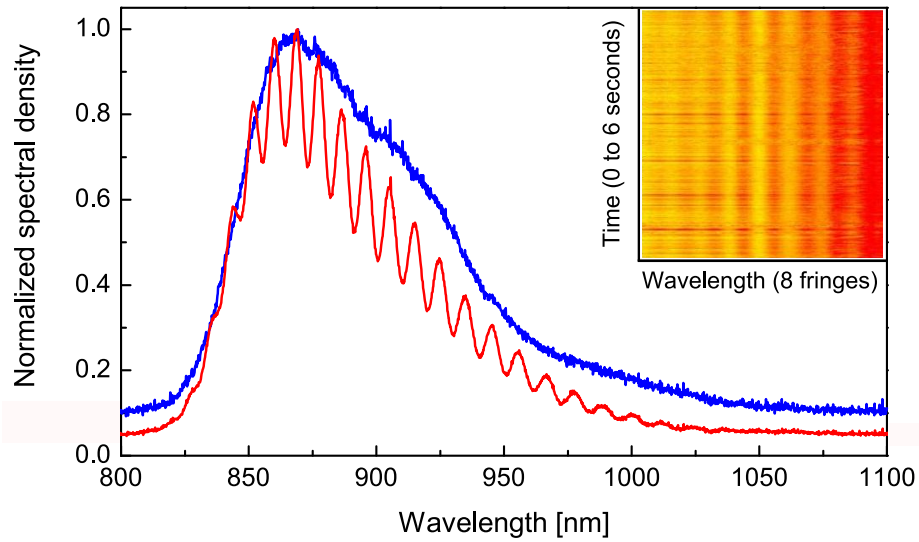

Figure 2.14: **Resulting spectra for the f-2f interferograms after filamentation.** Blue: the spectrum after the filament around 1 μm shows no modulations. Red: Doubling the 2 μm portion and overlapping it with the the 1 μm portion results in spectral fringes, an indication of CEP stabilization (see text for details). In the inset, a series of f-2f interferograms (10 ms exposure time) taken over 6 seconds displaying the near perfect stability of the CEP offset (estimated to less than 1 mrad).

How is this possible since our 800 nm does not have its phase stabilized? The answer is how superfluorescence takes place. As discussed above, when the OPA was described, a part of the pump itself is used to generate the signal in the OPA. Because during superfluorescence the strong dipoles induced by the pump couple to the pump itself, the superfluorescence pulse is phase-locked to the pump. When the generated signal is difference frequency mixed to the same pump in the second BBO,

any random phase in the pump will also be present in the signal, so when DFG takes place, they exactly cancel out, generating an idler free of any phase randomness. For this reason the idler is CEP stabilized. As a proof that this is indeed the case, we also created a filament using the signal, and the f-2f spectral interferogram showed no modulations, as expected. However, if desired in principle it is possible to generate CEP stabilized pulses at around 1.3 μm, if one selects using the grating in Fig. 2.7 the 2 μm portion of the superfluorescence spectrum and uses the 2 μm as the seed in the TOPAS's last DFG section. Finally, because the CEP stabilization is passive, it is much more stable than any active technique used so far. In Fig. 2.14 the fringe stability is remarkable, and it is preserved over long periods of time (probably hours if no laser adjustment is necessary). This should allow us to perform experiments that require long ours, such as high resolution angular distributions or photoelectron spectra if the plateau electrons are to be studied.

2.2 Apparatus for Electron-Ion Spectrometry

In the previous section, when it was described how filamentation takes place, it was said that plasma defocussing in gases (air) prevents the laser beam from focusing very tight. If this was not enough, charged particles interact strongly with air molecules, quickly losing their energy. It is then no surprise then that electron and ion spectroscopy are exclusively performed in high and ultrahigh vacuum chambers. In this section I will describe our electron and ion spectrometers and the associated electronics.

2.2.1 Vacuum chambers

In general, the encountered contaminants in ultrahigh vacuum (UHV) systems are water (H_2O), molecular hydrogen (H_2) and to a lesser degree various oils if the pumps used to generate the vacuum are oil-based. The water is usually present from the very beginning, being hard to pump out due to the fact that its polar molecules like to stick to the walls of the chamber via van der Waals interactions. The source of molecular hydrogen is a bit more subtle [46]. Atomic hydrogen is soluble in most metals (basically protons zipping inside the metal) and as such it can pass through the walls of the vacuum chamber. However, before desorption, these hydrogen atoms must combine together forming molecular hydrogen *on the surface*. To limit the amount of molecular hydrogen and lower the ultimate pressure in UHV systems, coating the inside walls of these vacuum chambers with various substances successfully limited the amount of hydrogen recombination and/or diffusion. Oils from pumping units can be reduced using scrubbers or eliminated altogether using non-oil based pumps.

The coincidence machine

The majority of the work presented in this dissertation was performed using the electron-ion spectrometer (to be described in the next subsection) sitting in the so-called coincidence machine. This name is used because the spectrometer has the capability of detecting ions and electrons in coincidence. A top view and a side view of this vacuum chamber are given in Figs 2.15 and 2.16, respectively. Two oil-based

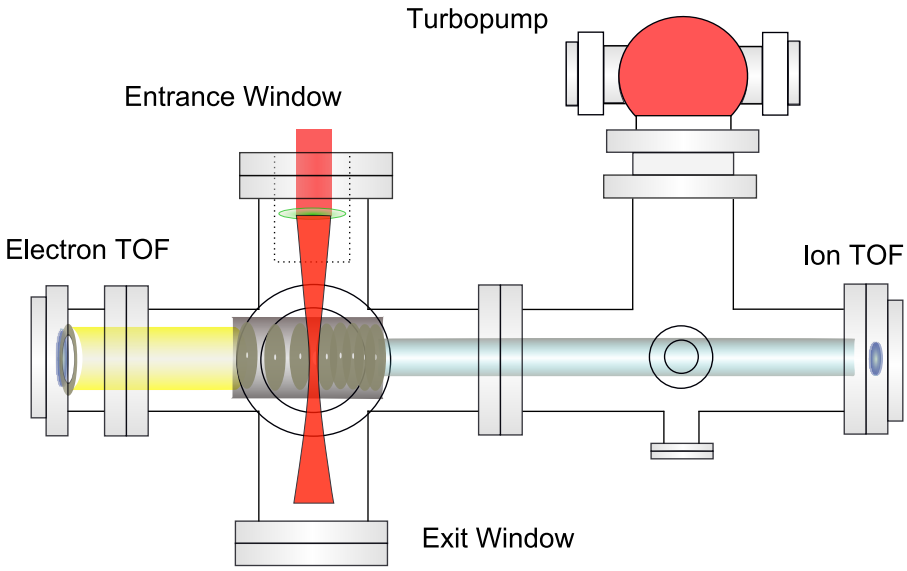

Figure 2.15: **Top view of the coincidence machine.** The oil-based turbomolecular pump mounted on the side of the chamber has a 510 liters/sec pumping speed (TPU510 from Pfeiffer-Balzers). To focus the collimated light on the spectrometer's axis (the details of the spectrometer are presented in Fig. 2.17), the recessed entrance window allows the use of lenses (green) with focal lengths 100 mm or longer.

turbomolecular pumps are used to generate the vacuum. The bigger of the two is a double barrel 500 liters/sec Pfeiffer-Balzers, model TPU510, while the smaller is a Leybold Turbovac TMP150 with 150 liters/sec. Both turbomolecular pumps are backed by a single dual-stage rotary vane mechanical vacuum pump (model SD300 by Varian). The volume of the vacuum chamber is roughly 50 liters. The vacuum pressure is measured with a nude ionization gauge (Varian, Model 580, range $1*10^{-3}$ -$4*10^{-10}$ Torr, calibrated for N_2). The gases to be studied are slowly leaked into the vacuum chamber with a variable leak valve. Without baking, pumping from atmospheric pressure (1 bar), the pressure reached by the two turbomolecular pumps after few hours is in the 10^{-7} Torr range, with H_2O the dominant contaminant. After

24-48 hours of baking at 100-130 degrees Celsius, the pressure decreases below 10^{-9} Torr if the chamber was exposed to air for a long period of time. To go below 10^{-10} Torr (an accurate number cannot be given due to the limit of the ionization gauge used), a 15 minutes run with a titanium sublimation pump (TSP, by Varian) with cryopanel (liquid nitrogen cooled jacket) is usually required. The sublimation pump is also used every time the base pressure in the chamber increases after long runs due to the water present in the gas lines.

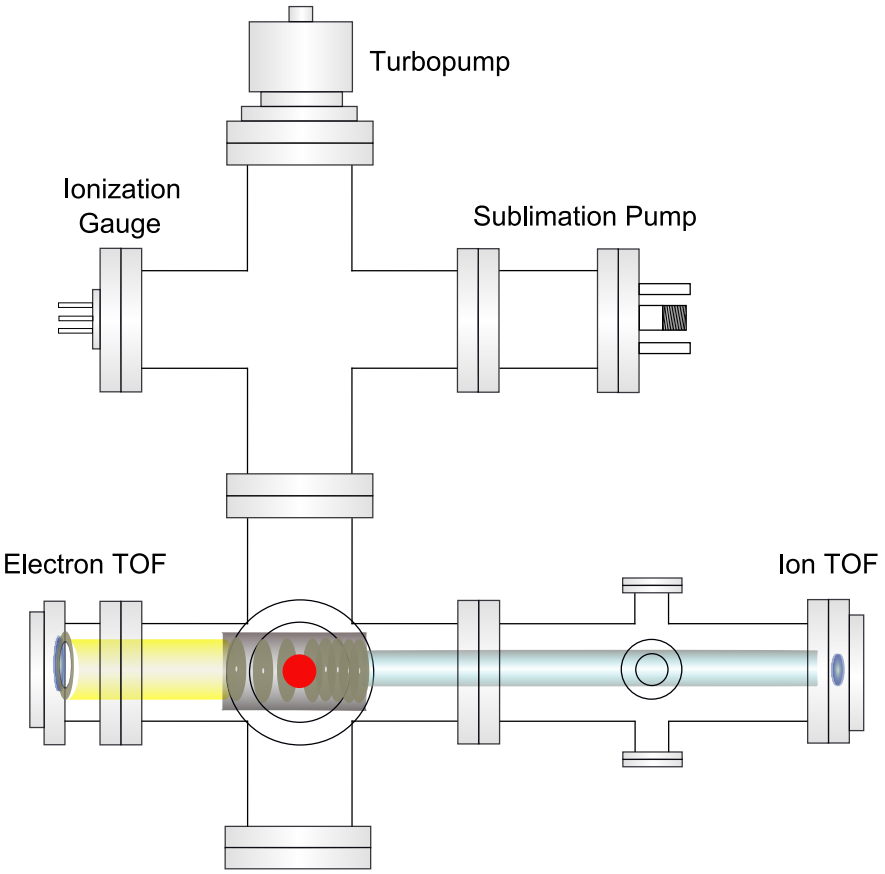

Figure 2.16: **Side view of the coincidence machine.** The turbomolecular pump on the top of the chamber has a 150 liters/sec pumping speed (Turbovac TMP150 from Leybold). The sublimation pump uses titanium filaments (50A of current) and it's jacket is liquid nitrogen cooled. The ionization gauge is a two filaments nude gauge (model 580 from Varian). The details of the spectrometer (Ion and Electron TOF) are presented in detail in Fig. 2.17)

The alkali machine

The alkali machine is also a time of flight spectrometer, built to study metal vapors and gases. Compared to the coincidence machine, it does not have coincident detection capabilities. However, it's flight tube is longer by more than a factor of two (50 cm versus 22 cm), giving it an superior energy resolution. Because this machine uses the same technology as the coincidence machine, a full description of the apparatus and associated electronics is not necessary. A detailed presentation of this machine is however available [48, 49].

2.2.2 The time of flight spectrometer

The time of flight (TOF) spectrometer's details are depicted in Fig. 2.17. It operates in two modes. For ions, it is a simple mass spectrometer. After ionization, the resulting ions are extracted from the interaction region and accelerated towards the multichannel plate (MCP) detector using static electric fields generated between the field plates. At first sight, a single plate to extract the ions should suffice. However,

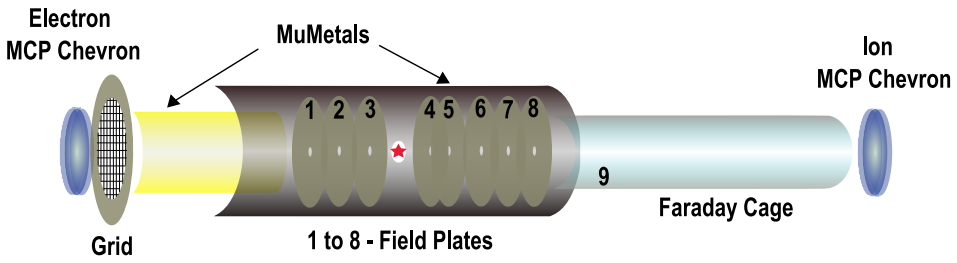

Figure 2.17: **Time of flight spectrometer for coincident ion-electron detection.** For electron detection, all plates are grounded. For ions, plates 1-3 are grounded, while the rest sit at various negative voltages to satisfy the Wiley-McLaren condition. In coincident mode, plates 2 and 4 are pulsed (see text for details). The MCP detector is depicted in detail in Fig. 2.18.

this would lead to poor resolution, primarily due to a spread in the initial kinetic energy of the ions as well as focal volume effects. Wiley and McLaren observed that stepping up and/or down the electric field can compensate this unwanted effects, for a given q/m ratio. This is the so-called Wiley-McLaren condition and in our case the plates 3,4 and 5 serve this purpose. The plates 6,7 and 8 together with the Faraday cage form an electrostatic lens, called the Eizel lens, whose purpose is to focus the ions onto the MCP detector.

For electrons, the spectrometer functions in a field free mode, with all plates grounded. Because the electrons can have very low energies, special care has to be

taken to assure that their kinetic energy is not modified from birth to detection by residual electric fields that might be present along the spectrometer. For this all field plates are made of molybdenum, a paramagnetic metal, and are coated with graphite to minimize patch effects. While magnetic fields cannot alter the kinetic energy of the electrons, it modifies their angular distribution. To assure that this does not happen, the entire spectrometer is surrounded with a cylinder made of mu-metal, gold and/or graphite coated.

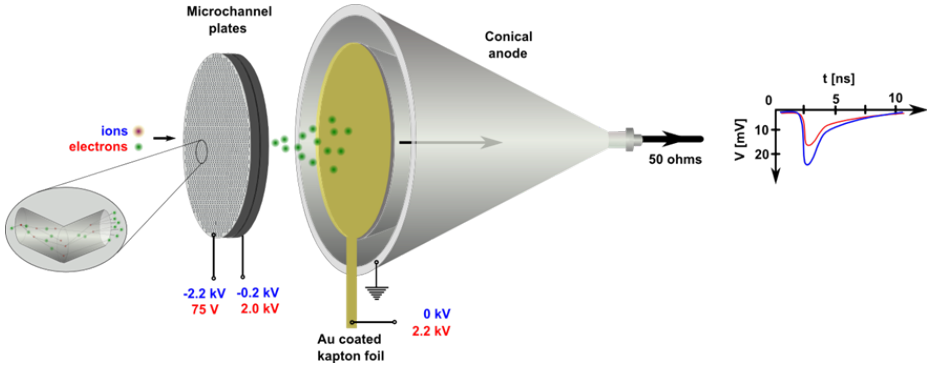

Figure 2.18: **The multichannel plate detector.** Ions and electrons are accelerated inside the channel (inset), releasing secondary electrons in a cascade fashion, generating a measurable signal. The typical voltages for electrons (red) and ions (blue) are shown. The role of the Au-coated kapton foil is to DC decouple the conical anode for electron detection. Without it, in electron mode the anode would sit at 2200 V. The angle of the conical anode is chosen for impedance matching.

The schematic of the MCP detector is presented in detail in Fig. 2.18, with the corresponding voltages for electron and ion detection. It consists of two impedance matched multichannel plates, aligned anti-parallel in a so-called Chevron configuration. The plates are made of a special lead-based glass and are coated with a substance developed to maximize secondary electron emission. The total resistance of the Chevron stack is quite high, around 20 MΩ and the electrostatic voltage applied is around 2 kV. Because the plates are quite thin (around 1 mm), the electric field inside is large (2 MV/m). As a consequence, when a charged particle enters one of the channels, it releases secondary electrons upon impact, which in turn are quickly accelerated and release tertiary electrons and so on, in a cascade, chain-reaction fashion. After passing through the channels, the initial particle becomes a shower of tens or hundreds of millions of electrons that when collected generate a measurable signal. For electrons, a grounded grid is placed right in front of the detector, to prevent the electric field lines of the detector penetrating into the field-free region of the spectrometer. Additionally, the potential on the front face of the detector in electron mode is

kept as low as possible (+75 V as indicated in Fig. 2.18), but high enough to flatten the detector's response as a function of the electron's kinetic energy, thus assuring that the measured spectrum does not present an artificial roll-off at low energies. For ions, this problem does not exist, and the front of the detector sits at 2.2 kV. For this reason, the signal generated in ions mode is about twice as large as the one generated for electrons. On average, the ion signal is around 20 mV, while for electrons is around 10 mV. The electron shower generated at the back of the MCP stack is collected on a gold coated thin Kapton foil and dumped to the ground through a resistor R, thus capacitively coupling the electron shower to the conical anode. This is necessary because the Kapton collector sits at 2200 kV, a voltage that cannot be fed directly into the electronics for signal processing. The Kapton foil together with the glue that holds it in place (Thorseal) in effect form a capacitor C, which together with the resistor R form an RC circuit. The time constant of this circuit gives the response time of the detector, typically around few hundred picoseconds (rise time). Finally, it worth mentioning that the MCP detector is a particle detector, and therefore two coincident particles will be detected as one, leading to pulse pile-up (this is not true if the MCP detector is used for imaging in conjunction with a phosphor screen, but this configuration was not used in our experiments). To prevent this effect, the detection count rate must be kept low, typically few hits per laser shot. For a more detailed presentation about MCP detectors the reader is encouraged to see the review article by Wiza [47].

The electronics setup employed to measure the time of flight signal is presented in detail in Fig. 2.19. The main component of the setup is the time to digital (TDC) converter, a device that as its name suggests measures the elapsed time between two events and then converts the result from an analog form into a digital form, suitable for subsequent computer processing. The technology employed is based on CAMAC (Computer Automated Measurement and Control), an old but reliable technology. To function properly, the TDC needs four inputs. One pair of signals is used to start and stop "the clock". Obviously, the start signal (called START) is a signal that must be generated by the laser when ionization occurs, while the stop signal (called COMMON) is the signal generated by a charged particle at the MCP detector after "flying" a distance L along the spectrometer. Because the TDC cannot accept for the START and COMMON the unconditioned signals generated directly by the photodiode and the MCP detector, the last two must be preprocessed first. The MCP signal is amplified by a fast amplifier (Model 574 by Ortec) and then sent into a pico-timing discriminator (Model 9307 by Ortec). The discriminator produces fast negative NIM pulses with negligible time shift as a function of the input signal (one has to remember that MCP signals can vary considerably in amplitude from event to event). These NIM pulses provide the COMMON for the TDC. The photodiode signal (we use 1 ns rise time photodiodes, various models as a function of the wavelength used)

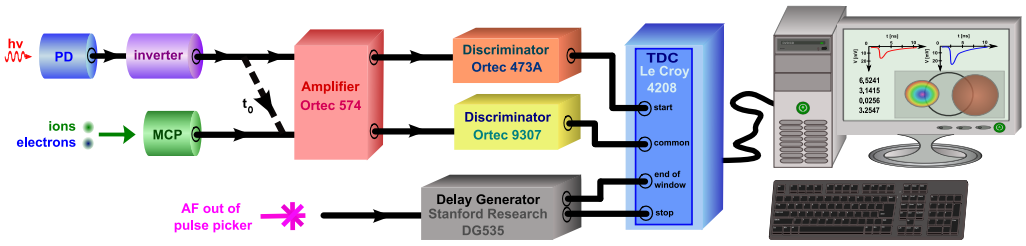

Figure 2.19: **Detection electronics for time of flight measurements.** The AF signal triggers the delay generator, which in turn determines in which mode the TDC is: in listening mode, the TDC measures the time elapsed between the arrival of the laser and the arrival of the charged particle, while in communication mode the measured time is sent to the computer for analysis.

is first inverted and then amplified by the same fast amplifier (the model 574 by Ortec has four identical channels). In principle, the amplification is not necessary, since the photodiode signal can be made large enough. However, the amount of light falling on the photodiode was reduced using neutral density filters so that the photodiode signal has the same amplitude as the average amplitude for the MCP signal (we will see below why this is necessary when we discuss the calibration of the spectrometer). After amplification, the photodiode signal is fed into a constant fraction discriminator (Model 473A by Ortec), whose fast negative NIM output provides the START signal. In addition to the START and COMMON signals, another pair of signals are necessary to control the state of the TDC. In essence, the TDC needs to know if it should expect to measure a time between the START and the COMMON, or to be ready to communicate to the computer. To switch between the two states (listening or communication), an audio frequency (AF) signal at the repetition rate of the laser is sent prior to ionization to a delay generator (Stanford Research, model DG535). The delay generator, triggered by the AF pulse, produces two NIM signals, separated in time. The first, called EOW (end of window), is generated 120 μs after the trigger, while the second, called CLR (clear) is generated 300 μs after the trigger. The EOW signal puts the TDC in communication mode, while the CLR signal puts the TDC in listening mode. The time delays quoted above assures that the TDC receives the signals in the right sequence: START, COMMON, EOW and CLR. Because we want to detect as many events per laser shot as possible, the TDCs used in the experiments presented in this thesis all have multi-hit capabilities. The two TDC models used were LeCroy 4208 and LeCroy 2228A, both operating in a single channel multi-hit configuration. In this mode all eight independent channels are cascaded, with each channel hit enabling the next one. The 4208 model is a 23+1 bit TDC, with a dynamic range of 8.3 ms and 1 ns resolution, making it suitable for measuring the time of flight

of slow particles (ions and slow electrons). The 2228A model has only 11 bits and three selectable full-scale time ranges (100, 200 and 500 ns) with the corresponding resolutions (50, 100 and 250 ps). These numbers are only approximate, and therefore each individual TDC was calibrated by sending dummy signals from a delay generator at controlled time intervals. Due to its reduced time ranges, the 2228A model was only used to measure the TOF of fast electrons. Finally, the CAMAC controller, not depicted in Fig. 2.19, is a model CC32 by Wiener.

As it was mentioned earlier when the spectrometer details were presented, for ions only a simple isotope identification is required for calibration. If uncertainties persist, the chamber can be fitted with a residual gas analyzer, that also functions as a mass spectrometer. Therefore, in the subsequent discussion we will focus solely on the electrons.

Due to the fact that the energy of the electrons produced in our experiments do not exceed 1% of their rest mass energy (0.51 MeV), a kinematic description within the framework of classical mechanics is enough to treat their motion. Therefore, an electron with an energy E at the end of the pulse will arrive at the MCP detector in a time t_{TOF} after "flying" through the field-free region of the spectrometer of length L according to the formula:

$$E = \frac{m}{2}\left(\frac{L}{t_{TOF}}\right)^2, \tag{2.3}$$

where m is the electron mass.

From Eq. (2.3), if one knows t_{TOF} and L one can find the energy E (or the momentum p). But is t_{TOF} the time measured by the TDC between the START and the COMMON? The answer is no, for two reasons. First, because the pulses from the photodiode and the pulses from the MCP detector travel through different electronics, each introducing its own delay. And second, because even if we would use identical electronics and identical cables, the photodiode will never be able to sit in the interaction region where the intensities reach levels many orders of magnitude above its damage threshold. All is not lost, since this artificial delay is just a constant that does not depend on the energy of the electron. Therefore, we can modify Eq. (2.3) by writing $t_{TOF} = t_{detection} - t_0$, with $t_{detection}$ being the measured time by the TDC and t_0 the delay we have to yet to determine:

$$E = \frac{m}{2}\left(\frac{L}{t_{detection} - t_0}\right)^2, \tag{2.4}$$

To determine the two unknown parameters in Eq. (2.4), we use the fact that the ATI spectrum presents a long series of peaks each separated by a photon energy. First, we perform a spectral measurement for our pulse, finding the central frequency. This

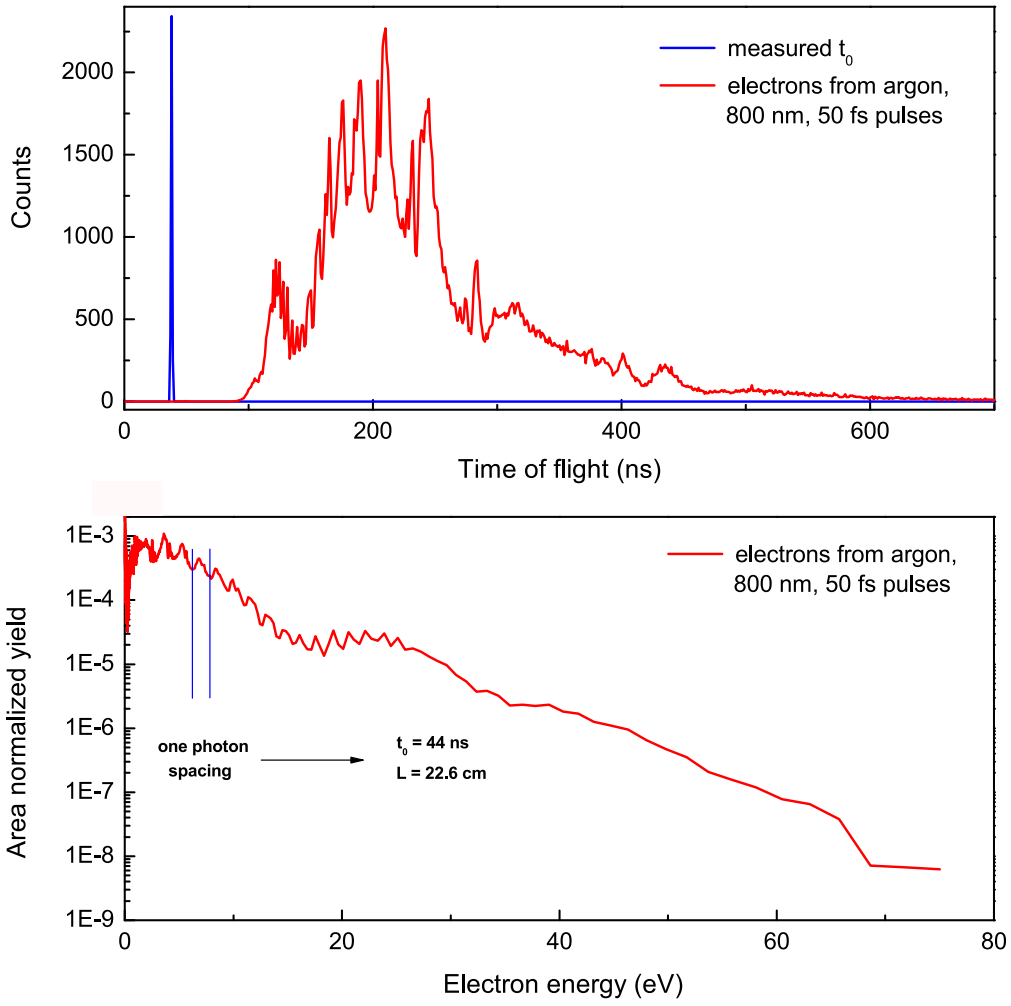

Figure 2.20: **Electron spectrometer calibration.** Upper panel: raw time of flight data (red) and measured t_0. Lower panel: processed data, with the spectrometer length (L) and fitted t_0 so that the ATI spectrum has the correct one photon spacing (see text for details).

can be accomplished using a USB spectrometer (Model USB4000, by Ocean Optics), with an accuracy of 0.2%. In the second step, we split the photodiode signal and feed one part in the usual electronic chain for this signal, while the other is fed into the chain for the MCP detector. In effect, this simulates the arrival of "instantaneous" electrons at the MCP detector. This allows us not only to measure the electronic delay (remember, this not enough to determine t_0), but also to assure that we use the entire time range of the TDC. If these "instantaneous" electrons do not produce a signal at the very beginning of the time range of the TDC, additional delay (BNC cables) is inserted in the photodiode signal's path.

In the upper panel of Fig. 2.20, the raw time of flight measurements for the electronic delay (blue) and the ATI spectrum of argon at 793 nm (red) is presented, using the 4208 TDC. The width of the electronic delay is only 2 ns, corresponding to just 2 time bins. For the ATI spectra, for calibration purposes, no intensity estimation is necessary. What it is desirable, however, is for the series to extend as far as possible. In this case, at least 18 peaks are visible, providing enough data points to allow a fit for the two parameter function from Eq. (2.4).

Naively, one can attempt to handpick (or use a peak finding program) the positions in time of the peaks in the ATI spectra and then fit the Eq. (2.4) to find t_0 and L. Although this would probably provide a result within the experimental uncertainties, it is not a rigorous approach. The reason for this is the fact that a correct transformation from time to energy must take into account the Jacobian of the transformation, which up to a constant for energy is $E^{-1.5}$. This constant can be omitted since we are only dealing with a relative measurement, not an absolute one. If, for example, absolute ionization rates are to be measured, thus taking into account the detection efficiency of the detector, then this constant must be included. In the lower panel of Fig. 2.20, we present the time to energy transformation of the spectrum from the upper panel, with the correct Jacobian taken into account. The fitted values for $L = 22.6$ cm and $t_0 = 44$ ns quoted in the graph were obtained by varying both to get the correct energy spacing for the ATI peaks. From Eq. (2.4), we can easily find the relative error for the energy as a function of the relative error for the two parameters:

$$\frac{\Delta E}{E} = 2\frac{\Delta L}{L} + 2\frac{\Delta t_0}{t_{detection} - t_0} \tag{2.5}$$

For very low energy electrons, their time of flight $t_{detection}$ is very large, and from the above equation it can be seen that the calibration fit is mostly determined by the relative error determining the spectrometer's length. For very fast electrons, the opposite is true, as the denominator of the last term on the right hand side of Eq. (2.5) can be quite small. In addition, the relative error for energy is not a constant across the spectrum, due to the presence of the quantity $t_{detection}$ in Eq. (2.5). However,

the contribution of the relative error coming from L is constant for all electrons and its value is around 1%. For these reasons, when dealing with the detection of fast electrons the choice of the right TDC is important, not only for the resolution, but also for the relative error.

The performance of the spectrometer can be seen in Fig. 2.21. For ions (upper panel), we measured the mass spectrum of xenon, using 2 μm, 50 fs pulses. The isotopes are beautifully separated, for single as well double ionization, with a corresponding resolving power better than 0.3 % Additionally, the integrated counts for each peak reflect the natural abundances for all isotopes. For electrons, a zoomed in plot for the plot given in the lower panel of Fig. 2.20 is given in the lower panel of Fig. 2.21. The entire spectrum covers only the first ATI peak, with its corresponding Rydberg structure. Below 0.2 eV, the transfer function of the spectrometer is decreasing, reaching 0 at 0 eV, as discussed before. For the Rydberg peak indicated in the graph, the relative energy resolution is 1.4 %, in line with the accuracy determining the length of the spectrometer.

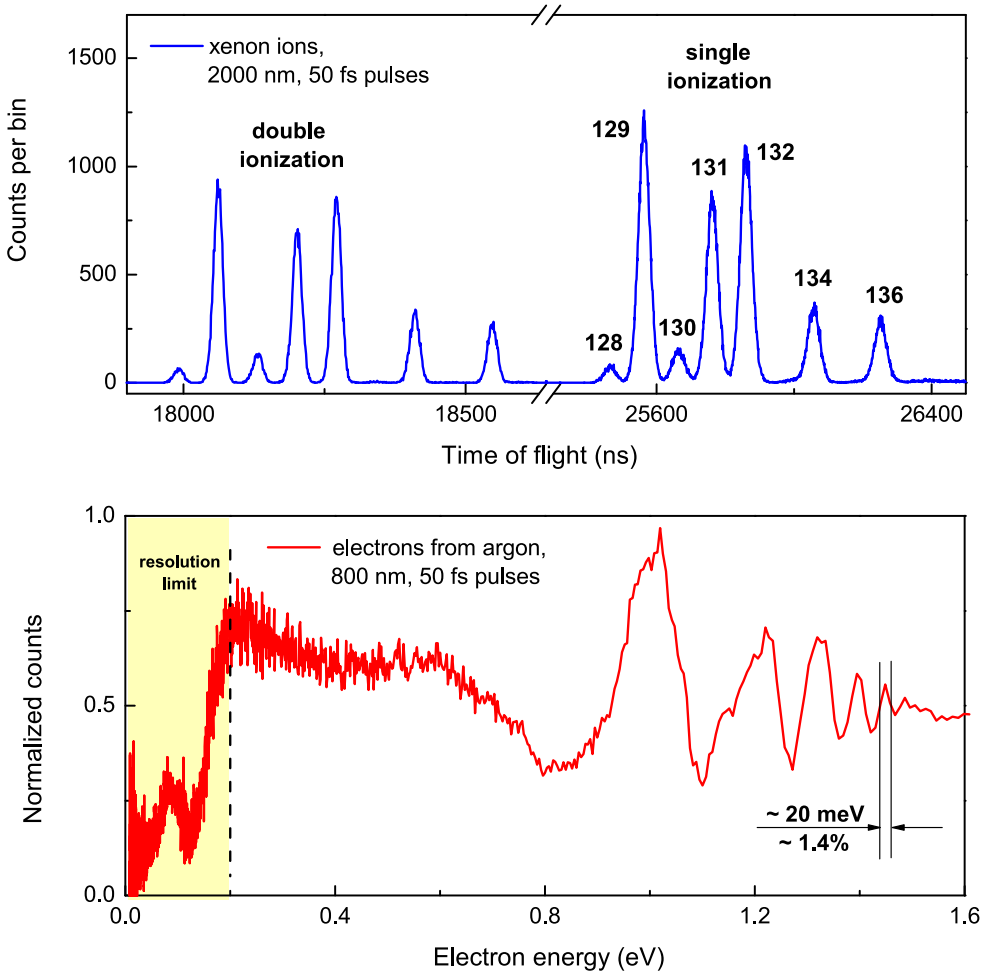

Figure 2.21: **Spectrometer Performance.** Upper panel: for ion detection mode, a simple isotopic identification is enough (in this case xenon). Lower panel: the first ATI peak in argon, displaying its clear Rydberg structure. For the lowest energies (yellow) the transfer function of the spectrometer approaches zero, a characteristic of all field free time of flight spectrometers.

Chapter 3

Experimental Findings

In the theoretical background chapter we briefly touched on the importance of the ponderomotive potential U_P in strong field physics. In particular, we saw that U_P governs three very important cutoffs: the $2U_P$ cutoff for direct electrons, the $10U_P$ cutoff for the rescattering plateau and the $3.17U_P$ cutoff for the return energy of an electron when/if driven back at the core. From a fundamental, physical perspective, it can be argued that all three cutoffs are of equal importance. From a technological perspective however, the $3.17U_P$ is probably the most important, primarily for its role in high harmonic generation (HHG), molecular tomography or any other processes that stem from the interaction of the laser-driven electron wave packet with its parent ion.

However, we can also view the process non-energetically, from Louis de Broglie's point of view, if we treat the electron as a wave, rather than a particle. The two perspectives are, of course, fundamentally linked by de Broglie's formula, $\lambda_{dB} = 2\pi/p$, where λ_{dB} is the associated de Broglie wavelength and p is the electron's momentum. This is not just a mere exercise. In one laboratory assignment taught as a Teaching Assistant, from the diffraction pattern created by a helium-neon laser the students were asked to determine the thickness of their own hair. The purpose of this laboratory work was to realize how diffraction can be used to determine the size (structure) of a given object when a wave of comparable wavelength diffracts on it. Can we do the same with the returning electron, essentially photographing an atom or a molecule? The answer is yes, but why bother with very expensive lasers when a much cheaper electron gun can do the trick? There are two main reasons to go through all this trouble. First, unlike an electron from an electron gun, the returning wave packet is *coherent* with the wave packet left in the ground state, HHG being a direct manifestation of this fact. More, the coherence should be preserved for inner shell electrons as well, since in an atom all electrons "know" about each other (that is why we write the wave function as a Slater determinant and we have selection rules for atomic transitions). And second, the dynamics of the electron wave packet is on

a *sub-cycle* scale of the driving field, comparable perhaps with the orbital period of a bound electron. This provides a "clock" for the process, which together with the "ruler" provided by a short de Broglie wavelength would form an atomic or molecular camera.

In this chapter, I will present some of the steps we believe are required in the development process of such a camera. At first, a new, unexpected and not fully understood phenomenon present in the tunneling limit will be presented. Then, we will move towards coherent laser-driven electron diffraction on atoms, alignment of molecules and diffraction on molecules. In the last part of the chapter, I will discuss more from a point of view of further projects than standalone results, electron wave packet interferences and coherent electron-driven Auger decay.

3.1 Classical or Quantum Electrons?

In the theoretical chapter we saw that treating the electron as a classical particle gave us the possibility to explain the two cutoffs present in the photoelectron spectra in the tunneling regime: the $2U_P$ cutoff for the direct electrons, as well as the $10U_P$ cutoff for the rescattered ones. In addition, we have identified the birth phases for those electrons that give the two cutoffs. Despite this success, a more rigorous proof for a classical treatment is desirable. In the subsequent sections I will use extensively the hypothesis that in the tunneling regime the electron can, indeed be described as a point-like object for arbitrary birth phases, whose motion can be determined using nonrelativistic classical mechanics. This will allow us not only to get an intuitive picture of the processes involved; but more importantly, due to its deterministic nature, the classical treatment will allow to follow back in time the motion of a detected electron all the way to its moment of birth. In fact, we have already done so when the origin of the $2U_P$ and $10U_P$ cutoffs was presented.

There are several approaches to justify the classical treatment. One would be to compute the time-dependent electron wave function and show that the expectation values for electron's position and momentum follow the classical trajectories. In addition, one might want to compute the quadratic mean as well to determine the deviation from the mean. Given that the above approach will have to start from the Schrödinger equation employing certain approximations for computational reasons, another approach is to solve the Schrödinger equation numerically. This would have the advantage that at least in the single active electron approximation the effects of excited states, realistic pulse shapes and the Coulomb potential of the atom are properly accounted for. If the time dependent wave function $\Psi(\vec{r},t)$ is computed numerically, then one can make a movie by plotting $|\Psi(\vec{r},t)|^2$ on a spatial grid as a function of time and comparing the quantum and classical results. Such a compu-

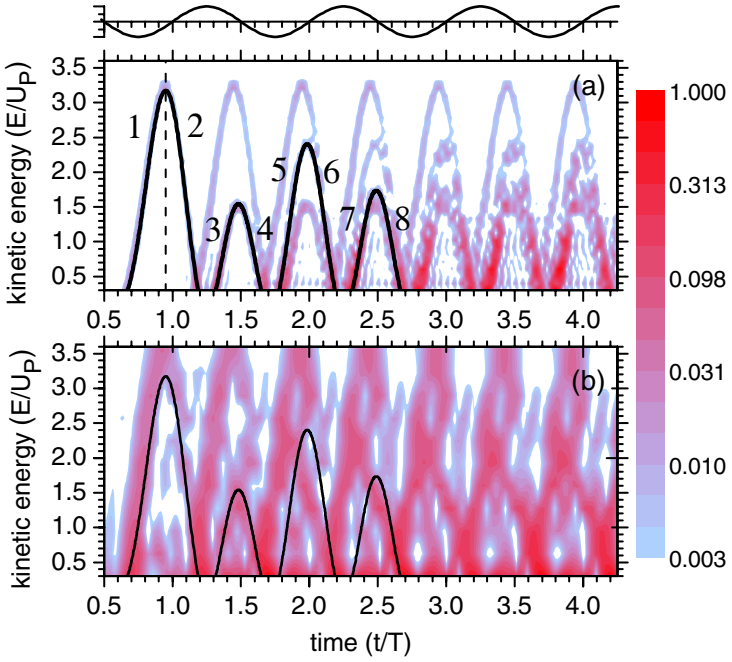

Figure 3.1: **TDSE history of HHG emission.**(from [52]) The numerical computation was done in the case of argon, using 8-cycle flat-top pulses (with its electric field pictured at the top) at 2.0 μm (a) and 0.8 μm (b). The two history plots were found using the windowing technique described in [51]. The black curves are the classical returns predicted by the Simpleman's model. Curves 1 and 2 are the first return for the long and short trajectory, respectively. The pair of curves (2n-1, 2n) are for the n-th classical return.

tation was performed by Muller [50] for helium, where the evolution of the tunneled wave packet was followed many cycles after ionization when "numerically" irradiated by 0.8 μm radiation at 600 TW/cm^2 (giving a $\gamma \sim 0.6$). The paper dealt however with certain resonances attributed by the author to the long range nature of the Coulomb potential and a comparison to the classical prediction was not given. Several movies were supplied electronically, available for download as supplemental supportive information for the print version and the reader is encouraged to see them. The third approach is to study the TDSE time history of HHG emission as first reported by Yakovlev and Scrinzi [51], obtained by using a windowing technique. In short, the authors multiply the acceleration of the atomic dipole obtained from the TDSE numerical computation with a Gaussian window and taking the square of the Fourier transform of the result the harmonic spectrum emitted in the time-window can be

found. Finally, the HHG history can be found by scanning the window along the pulse duration.

A similar computation was performed by Tate et al. [52] adapting the recipe form [51]. First, the HHG was obtained from the acceleration of the atomic dipole by a direct Fourier transform. Then, selecting only a spectral window $\Delta\omega$ around the frequency ω and inverse Fourier transforming it back to the time domain the emission history for the photons with the frequency ω was found. Finally, repeating the procedure scanning the window for all frequencies the entire HHG history was obtained. Their result for argon at 160 TW/cm^2 with both 0.8 μm and 2.0 μm flat top pulses is reproduced in Fig. 3.1. The corresponding Keldysh parameters for the two wavelengths are 0.9 and 0.35, respectively.

The result from [52] was chosen for several reasons. First, although the 0.8 μm has a sub unitary Keldysh parameter, in the vicinity of $\gamma = 1$ the ionization is expected to be rather balanced between tunneling and multiphoton whereas in the 2.0 μm case tunnel ionization dominates. This fact gives us the opportunity to see the differences between the two regimes, this time for HHG. Second, because the wavelengths used in the calculation are the ones extensively used in this dissertation (the attentive reader should not be surprised here, since the theoretical paper was a product of a collaboration driven by our group and we did have in mind at the time our experimental capabilities). Finally and most importantly, the classical prediction is conveniently overlapped with the quantum calculation for an easy comparison. The classical result is given by the black curves. The curves 1 and 2 represent the first classical return for the long and short trajectories. Subsequent classical returns are represented by the curves labeled 3 and 4 (second return), 5 and 6 (third return) and so on. As it was explained in the theoretical chapter, multiple returns are children of the long trajectory.

Several conclusions can be drawn from the information-rich plots depicted in Fig. 3.1. The classically predicted $3.17U_P$ cutoff (the offset equal to the ionization potential in both bases was subtracted for an easier comparison) for the first return is not clearly observed for the mixed regime at 0.8 μm, whereas the 2.0 μm result is spot on. Also, the quantum calculation coalesces around the classical prediction at 2.0 μm, whereas for 0.8 μm the result is more diffuse. For 2.0 μm, as many as four classical returns can be seen, although as the emission moves to higher times interferences between different trajectories start to blur the picture. We also observe that for the long wavelength the higher returns have a large HHG emission amplitude. This is a puzzling effect, given that the long time spent in the continuum by the ionized wave packet from birth to recombination should reduce its overlap with the ground state due to ballistic expansion. As possible explanations for this effect population trapping in excited states and Coulomb focusing were proposed by the authors. If indeed responsible, these excited states would likely have to be close to the continuum (Rydberg states),

because it is hard to believe that wave packets trapped in tighter bound states could follow the classical prediction which assumes the electron free. Coulomb focusing is due to the well-shape of the potential of the ion with the returning wave packet "falling" into it as it revisits the core. This is a long-range effect, with the electron wave packet experiencing the same hydrogenic-like potential for both wavelengths. Contrary to the quantum finding, due to the much larger ponderomotive energy for the long wavelength, one expects Coulomb focusing to actually be less important at 2.0 μm, since the electron wave packet's kinetic energy is many times over the electrostatic potential energy of the coulombic well. There are however trajectories for which the returning wave packets posses low kinetic energies at recollision even at long wavelengths, in which case Coulomb focusing could be responsible for the importance of these low kinetic energy multiple returns in HHG emission. Finally, we note that the quantum result supports the assumption made in the Simpleman's model that the classical electron is born at $\vec{r} = 0$ with zero kinetic energy, since the black curves in Fig. 3.1 were computed with these approximations. In addition, the Coulomb potential, neglected in the Simpleman's model, does not cause a discrepancy between the classical and quantum calculations for the longer wavelength.

To summarize, at long wavelengths deep into the tunneling regime the quantum computation coalesces around the classical prediction, allowing us to model the motion of the ionized wave packet using classical mechanics. At no point however I will argue that the electron is truly classical. Instead, we should view the classical "motion" as resulting from the statistical nature of quantum mechanics. In the experiment, the statistical nature is de facto built in, since the spectra are comprised of 10^5-10^6 ionization events. In the subsequent sections we will see the quantum nature of the electron wave packet directly when we will discuss its diffraction on the parent ion upon recollision and interferences between wave packets launched at different times during the laser pulse.

3.2 The Low Energy Structure (LES) in the Photoelectron Spectra in the Tunneling Regime

Shortly after the optical parametric amplifier (OPA) was installed (2006), we began taking photoelectron spectra in noble gases. The main goal at the time was to study the so-called wavelength scaling law for the plateau electrons, paying particular attention on the height of the plateau, since it is directly linked to the wave packet ballistic expansion which together with phase matching determine the conversion efficiency of HHG. The results of this study were subsequently reported in [53].

Despite the fact that overall the newly obtained spectra at 2 μm in xenon looked like one would expect (as was presented in the first chapter of this work), there was something peculiar at very low energies: a prominent spike-like structure. At first, knowing that low energy electrons are the most susceptible to stray fields in the spectrometer, we had to convince ourselves that the machine was performing as normal. This was done by taking a known spectrum in argon using the 0.8 μm titanium sapphire laser. The result was immediate: the spectrometer was performing flawlessly, with the spectrum presenting both the unmistaken ATI peaks as well as Rydberg resonances due to the large AC Stark shift of highly excited states (see Fig. 2.21). Convinced that the new feature was real, it was named the Low Energy Structure (LES) for publication purposes [54], while for in-house use we fondly refer to it as "the pickle" (the short story about this name was given in [48]). For a graphical definition, the LES together with the classical looking remainder of the spectrum are depicted in Fig. 3.2 for xenon, 2.0 μm, 50 fs pulses generating $6.5 \cdot 10^{13}$ W/cm^2.

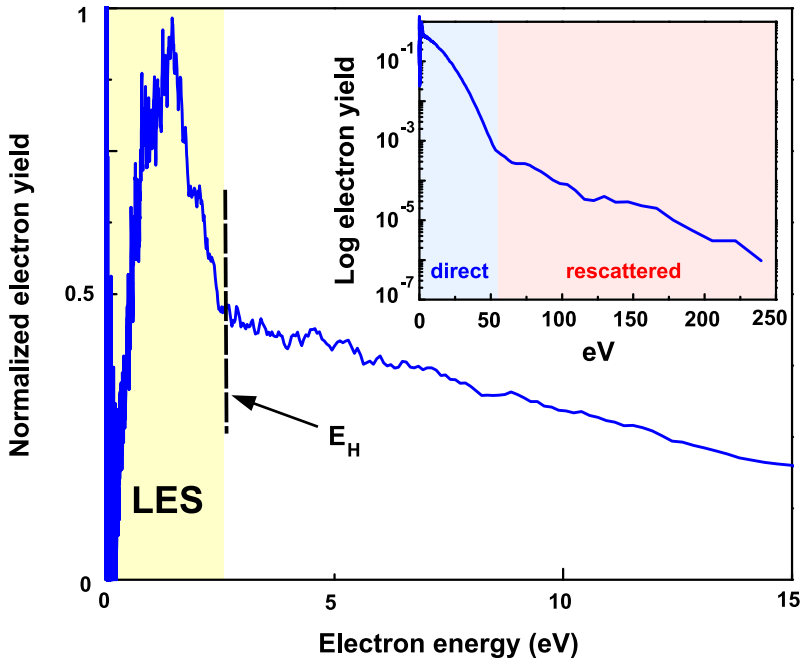

Figure 3.2: **Definition of the LES.** The low energy photoelectron distribution in xenon at $6.5{\cdot}10^{13}$ W/cm^2 with 2.0 μm, 50 fs linearly polarized pulses along the polarization axis. E_H denotes the extend of the LES region (in yellow). In the inset, the entire distribution is shown, displaying the well known "direct" and "rescattered" electrons. Both graphs are normalized to the maximum value. (see text for details)

Within a short period of time, one of the main characteristics of the LES became

evident: its universality in the tunneling regime. If the Keldysh parameter was slightly below unity the LES was present regardless of wavelength, intensity or target. One should remember here that the separation between multiphoton and tunneling is not an abrupt passage. In fact, the intensity distribution in the focal volume guarantees that while in the center we have tunnel ionization, the ionization in the outer regions is multiphoton, due to their lower intensities. Additionally, due to the temporal profile of the pulse, at and near the peak of the pulse envelope tunnel ionization dominates while in the beginning and the end of the pulse multiphoton does. In Figs. 3.3 and 3.4 we present the low energy spectra for various atoms and molecules, respectively. Similar spectra were obtained for alkali atoms, as well as normal and heavy water. To date, the LES is present in virtually all atoms and molecules studied in our laboratory if the tunneling condition is fulfilled.

The immediate consequence was obvious: due to its universality, the LES needed to be treated and understood fully for any type of experiment in this regime. To deal with this new effect, a kitchen sink strategy was employed. We have used various theoretical tools, as well as numerous experimental techniques, taking advantage of the fact that we had a tunable mid-infrared laser system capable of saturating any atomic or molecular targets for wavelengths in the 1-2 μm range.

On the theoretical front, it was immediately apparent that the analytical models at our disposal fail to predict the LES. In Fig. 3.5 we plot the measured low energy part of the photoelectron spectrum in argon ionized by 2.0 μm, 50 fs pulses generating $1.5 \cdot 10^{14}$ W/cm^2 and compare it with SFA-KFR as well as 3D single active electron TDSE. Both theoretical curves were obtained using the proper intensity average to account for the realistic focal volume. As opposed to KFR-SFA, the full 3D TDSE accurately reproduces the LES, but as it was mentioned in the theoretical chapter, the mechanism responsible for the LES is not immediately evident, since this is an all-encompassing calculation. However, we can already conclude that the LES is a single electron effect, so multi electron effects such as electron-electron correlations can be neglected. Based on the above considerations, the origin of the LES had to be linked to at least some of the ingredients missing in the SFA-KFR models but present in the 3D TDSE. The main ingredients missing in the SFA-KFR models are: excited states and the long range Coulomb potential during ionization and rescattering of the electron wave packet. To investigate these effects, a more thorough experimental investigation of the LES was needed.

In Fig. 3.6 we plot the low energy photoelectron spectra in xenon at saturation ($8 \cdot 10^{13}$ W/cm^2) for 0.8 μm, 1.5 μm, 2.3 μm and 3.6 μm, corresponding to the Keldysh parameters 1.13, 0.6, 0.4 and 0.25, respectively. For the shortest wavelength, the ionization is multiphoton, as can be seen from the presence of sharp ATI peaks, while for the two longest wavelengths the ionization is tunneling in nature and a prominent LES is present. In fact, at the lowest wavelength, the LES seems to have

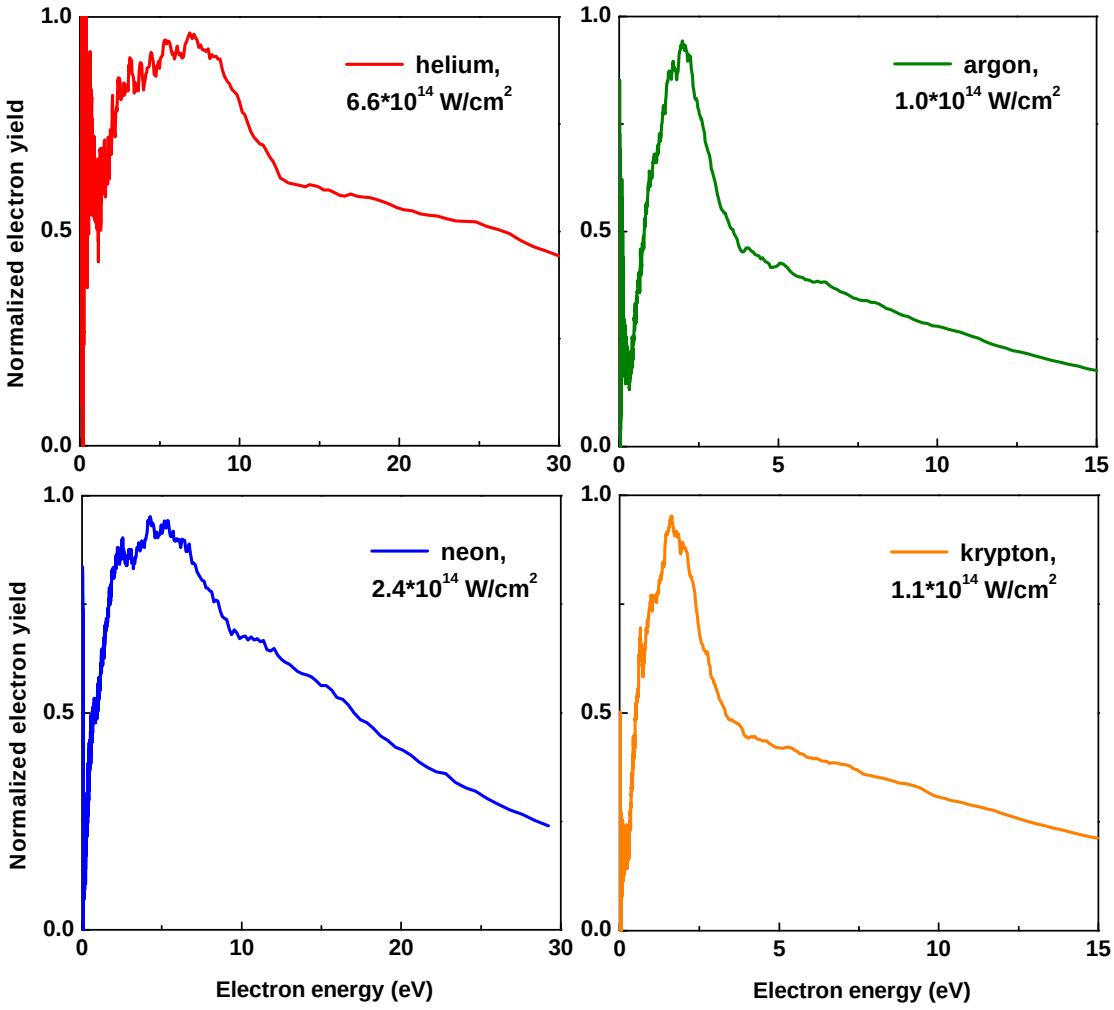

Figure 3.3: **The LES in atoms.** All targets were irradiated at the indicated intensity with 2.0 μm, 50 fs linearly polarized pulses. The spectra were collected for electron emission along the laser polarization within a solid angle of 0.65 mrad. Coupled with the result presented in Fig. 3.2 it can be seen that the LES is present over a large range of intensities (10^{13}-10^{15} W/cm^2).

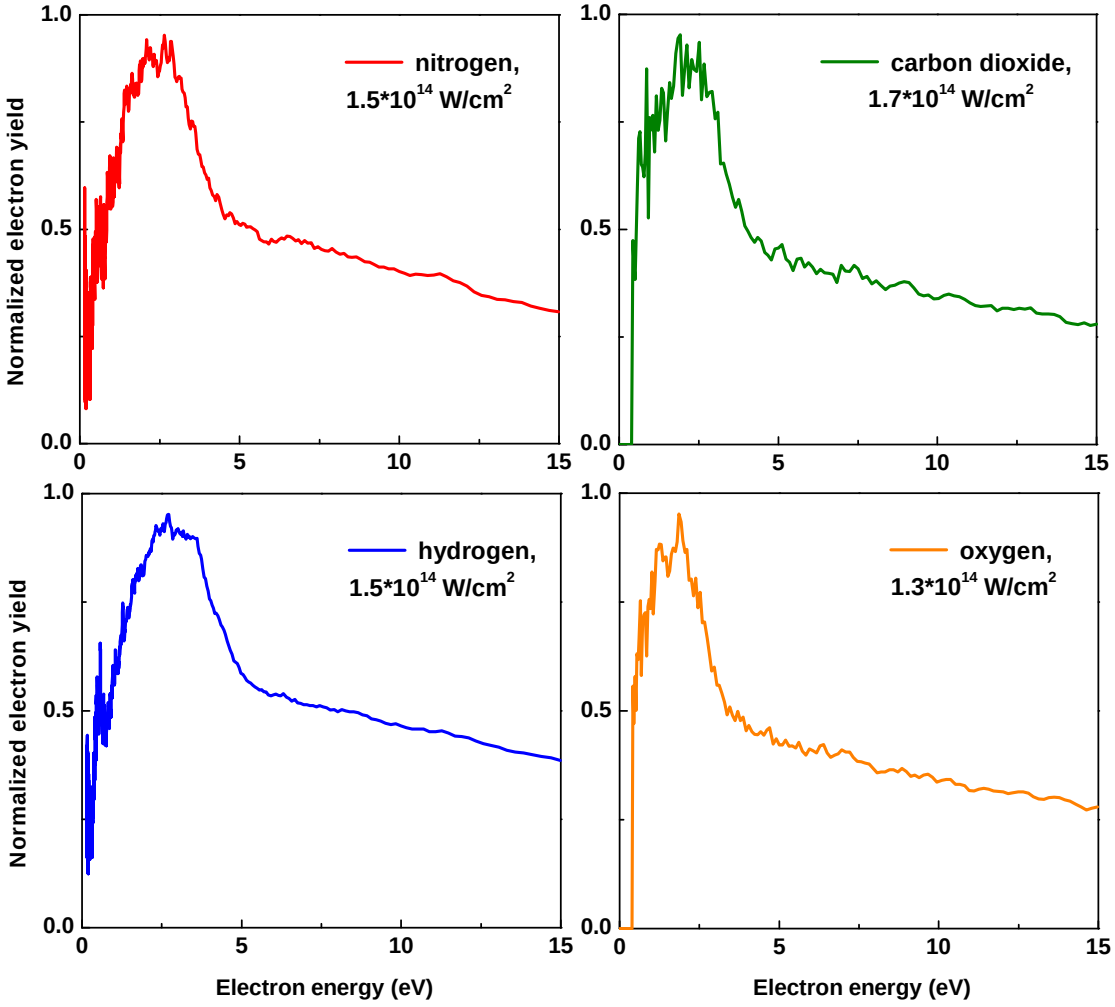

Figure 3.4: **The LES in molecules.** All targets were irradiated at the indicated intensity with 2.0 μm, 50 fs linearly polarized pulses. The spectra were collected for electron emission along the laser polarization within a solid angle of 0.65 mrad. For molecules, the intensity range covered in the above plots is narrower than that for atoms, the limiting factor being the low ionization potential for molecular targets.

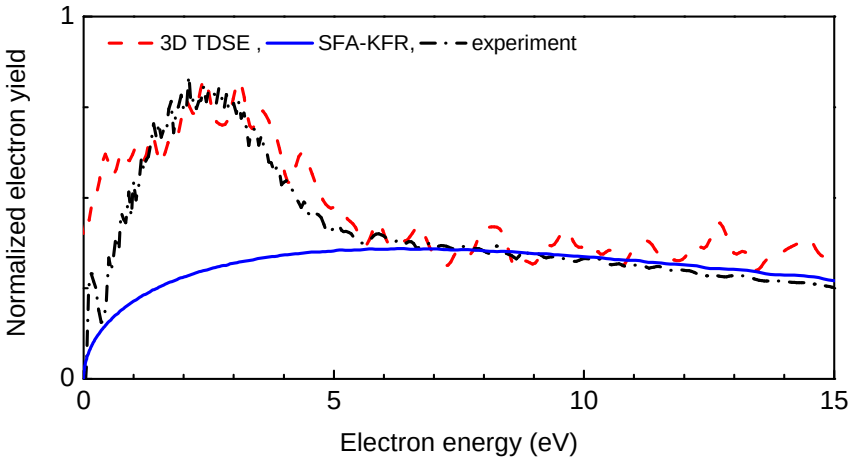

Figure 3.5: **The LES versus theoretical predictions for argon at $1.5{\cdot}10^{14}$ W/cm^2 using 2.0 μm, 50 fs linearly polarized pulses.** The experiment is remarkably well reproduced by the three-dimensional TDSE. For comparison, the SFA-KFR theory using Volkov states fails in this region. The calculated distributions are obtained using intensity averaged, 10-cycle flat-top pulses.

a double peak structure. The intermediate 1.5 μm case is less clear, as it seems that in addition to the ATI peaks there could be a small LES extending up to 1 eV. Unfortunately, the width of the LES is comparable with the photon spacing, making the distinction between the LES and ATI peaks difficult. Additional data taken at intermediate wavelengths (from 1.2 to 2.0 μm) does show a gradual emergence of the LES as a function of wavelength for a given intensity.

In Fig. 3.7 we plot the dependence of the LES with intensity in the case of argon, ionized with 2.0 μm, 50 fs pulses. Obviously, the ionization rate varies greatly over the intensity range covered in the experiment, so each curve was normalized to unity for an easy comparison. The immediate conclusion is that the width of the LES increases with intensity (or the ponderomotive potential for a fixed wavelength) and decreases with the Keldysh parameter.

However, Fig. 3.7 still cannot answer the question if the LES is linked to the act of ionization itself or the electron wave packet dynamics in the continuum since both depend on the electric field strength. To shed some light on this issue we measured the electron spectra of xenon for a given ponderomotive potential by varying simultaneously the wavelength and the intensity (one has to remember that $U_P \sim I\lambda^2$). The result is present in Fig. 3.9. Since the LES is virtually identical in the three cases, the implication is that the origin of the LES must be linked to the dynamics of the electron wave packet in the continuum and not to the ionization process itself,

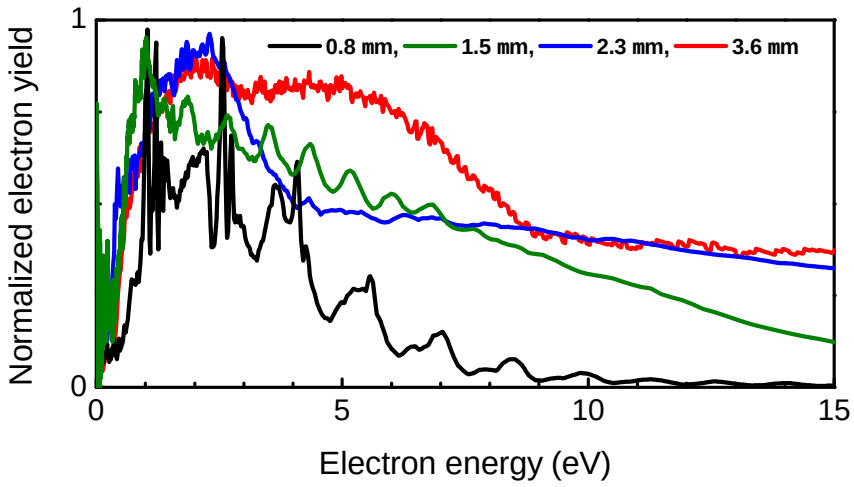

Figure 3.6: **The behavior of the LES versus wavelength.** All four spectra were taken in xenon near saturation ($8{\cdot}10^{13}$ W/cm^2), using 50 fs linearly polarized pulses for the wavelengths indicated on the figure. The emergence of the LES at longer wavelengths is linked to the disappearance of the ATI structure indicating that the LES is a phenomenon characteristic to the tunneling regime.

since the three different intensities correspond to three different thicknesses for the tunneling barrier.

From mid nineties, it was found that the HHG signal as well as the rescattering plateau depend strongly on the polarization of the light (citations here). Following this recipe in Fig. 3.8 we plot the photoelectron spectra for linear polarization (LP) and circular polarization (CP) in xenon at 2.0 μm, 50 fs pulses for a peak vector potential of 1.8 atomic units.

Due to the fact that the LES is present only in the case of linear polarization but it is absent in the case of circular polarization, one can be tempted to conclude that rescattering is responsible for the LES, since in circular polarization the ionized electron is driven by the external field away from the core and rescattering cannot happen. This assumption however, seems to be at odds with Figs. 3.7 and 3.9. As we have mentioned earlier, after tunneling the wave packet undergoes a ballistic expansion. This expansion is expected to have a linear dependence in time. For example, a wave packet that returns at the core after half a period of the driving field is expected to expand more for 2.3 μm than for 1.7 μm. This wavelength scaling law states that the wave packet expansion in terms of volume expands for equal phases

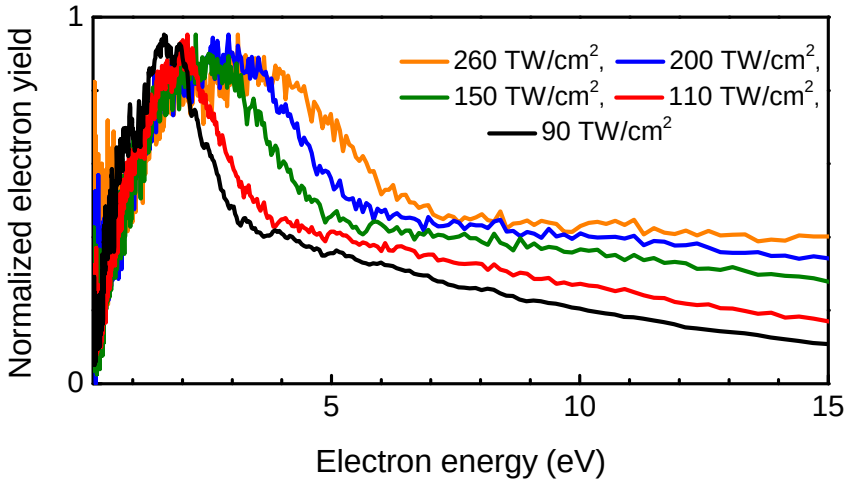

Figure 3.7: **The behavior of the LES versus intensity.** The spectra were taken in argon, using 2.0 μm, 50 fs linearly polarized pulses along the laser polarization. The LES region expands increasing the intensity, as the ionization process moves deeper into the tunneling regime.

as $V \sim \lambda^3$. Therefore, one would expect that the height of the LES would become smaller with increasing wavelength, contrary to what was found experimentally and presented in Fig. 3.9.

One possible explanation for this discrepancy is the fact that perhaps at birth the wave packets are different for the three wavelengths. This is to be expected, since the three cases correspond to three different thicknesses of the barrier through which the wave packet tunnels out and in general, the thinner the barrier the more divergent the tunneled wave packet should be. To illustrate this effect, using the dependence given by Eq. (1.18), in Fig. 3.10 we plot the ADK tunneling rate as a function of electron's perpendicular momentum (with respect to the laser polarization) for the three data sets from Fig. 3.9. From Fig. 3.10 we can quickly estimate that the half width at half maximum for 1.7, 2.0 and 2.3 μm are given for electron momenta located at 0.078, 0.073 and 0.067 au, respectively. Since in the direction perpendicular to the laser polarization the electron's motion is uniform (if the Coulomb potential is ignored), after half a cycle when recollision takes place, the three wave packets will have the following radii: 9.1, 10.0 and 10.6 au. To estimate the radii, the assumption $m_e = 1$ was made in $p = m_e v$ so that $r = \pi v/\omega = \pi p/\omega$. While the effect of the barrier

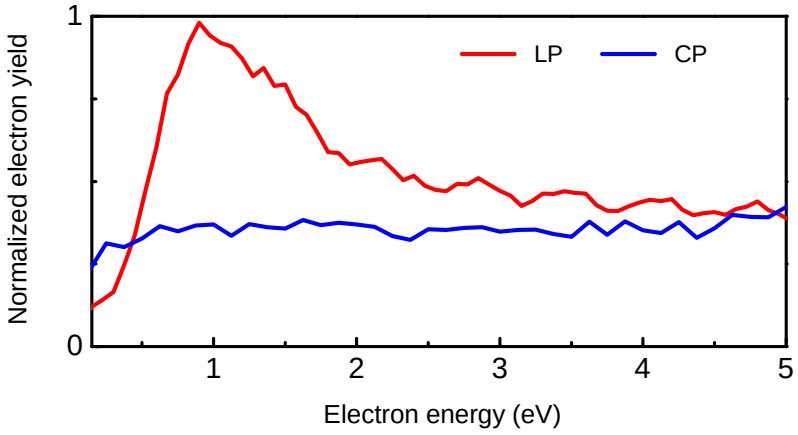

Figure 3.8: **The behavior of the LES versus the polarization of the light.** The spectra were taken in xenon, using 2.0 μm, 50 fs pulses for linear polarization (LP) and circular polarization (CP). The absence of the LES for circular polarization indicates a rescattering event is responsible for the LES (see text for details).

thickness alone cannot explain the result from Fig. 3.9, it does seem to partially compensate the ballistic spread, so that the increase in the wave packet radius from 1.7 to 2.3 μm is only 16%, and not 35%, as expected from the wavelength scaling relation.

To investigate these effects further, we can also look back at the behavior of the LES versus intensity at constant wavelength. One might be tempted to use Fig. 3.7, but since for various intensities a given measured photoelectron energy corresponds to different birth phases, it would be desired to plot the electron yield as a function of birth phase and not as a function of energy. When such a transformation is performed, we can find when the LES electrons were born. This can be easily accomplished if we convert the raw time of flight data to momentum and with the assumptions made in the theoretical chapter when the Simpleman's model was presented we have $p_{detection} = A_{max}(\phi_{birth})$. This equation has an infinity of solutions, but due to the periodicity of the laser field we can consider only the interval $(0, \pi)$. In this interval, there are two solutions, one in the first quadrant and another in the second quadrant. Since we suspect recollisions to be responsible for the LES, we will retain only the solution found in the interval $(\pi/2, \pi)$, as it is the only one that allows the electron to revisit the core. Plotted as a function of the phase at birth, we can compare the above distributions for equal excursion times (in the theoretical chapter we saw that

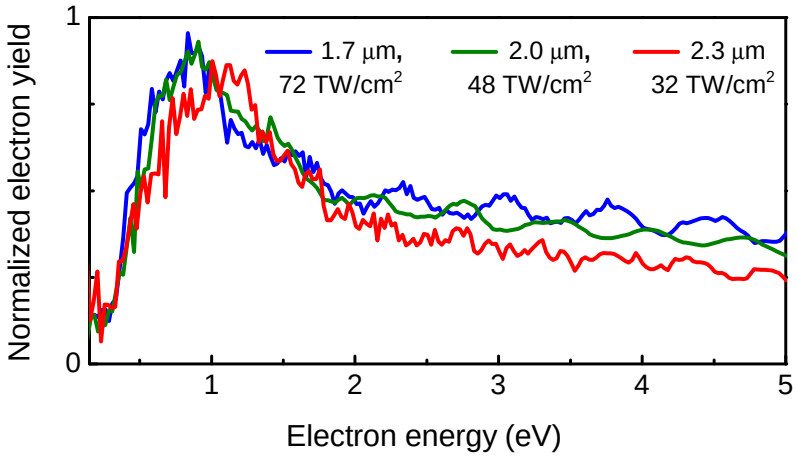

Figure 3.9: **The behavior of the LES at constant ponderomotive energy.** The spectra were taken in xenon, using 2.0 μm, 50 fs linearly polarized pulses. Remarkably, the LES is identical in all three cases, pointing to a field-driven process for the origin of the LES.

the excursion times are only a function of the phase at birth and do not depend on intensity for a given wavelength - *if* the assumptions of the model are valid). After applying the Jacobian of the transformation, the result is presented in Fig. 3.11.

Two conclusions can be drawn immediately. First, the relative height of the LES versus the rest of the distribution at a given wavelength becomes larger for smaller amplitudes of the vector potential. Whereas the barrier thickness does play a role here, the wave packets return with different energies for a given phase so at this point we cannot attribute the above conclusion solely on it. The second observation is the intriguing overall invariance of the LES distributions as a function of birth phase. For all intensities presented in the plot, the LES region extends up to 1.79 radians with its maximum corresponding to a birth phase of 1.74 radians.

These phases correspond to the second classical return. This can be seen from Fig. 3.12 where we plot the photoelectron yield as a function of birth phase for xenon at saturation driven by 3.6 μm, 90 fs linearly polarized pulses together with the number of classically allowed returns. The number of classical returns were computed numerically using a simple one dimensional model of a free electron in an alternating electric field. The electron was treated nonrelativistic, so the magnetic field was ignored. The electron was placed in the origin with zero initial momentum, as in the Simpleman's model. For every birth phase, the electron was followed for 10 periods of the driving

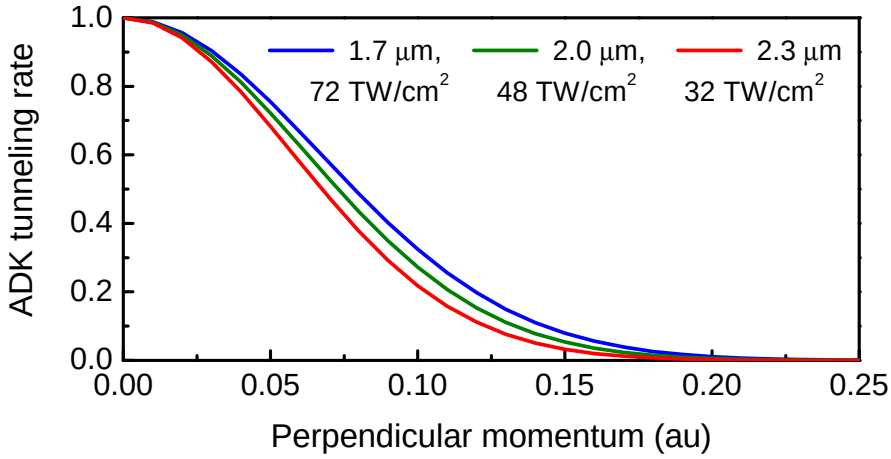

Figure 3.10: **The spread of the electron wave packet after tunnel ionization in the direction perpendicular to the laser polarization.** The three lines are computed using Eq. (1.18) for the intensities indicated, without averaging over the pulse duration. Due to the very different overall tunneling rates for the three cases all curves are normalized to unity for an easy comparison. The result indicates that at the highest intensity, in which case the tunneling barrier is thinner, the wave packet expands more rapidly.

field and at each crossing of the origin a counter was incremented by one unit. To study the second return it is desired to perform a strong field scattering calculation in the third order Born approximation, thus allowing the electron wave packet to scatter twice on its parent ion, upon the first and the second return. However, to my knowledge, no such calculation currently exists (at least not for laser parameters close to the ones used here). Perhaps a second order Born approximation (which does allow a single rescattering event, regardless the phase) would suffice. For the second order Born approximation to succeed in reproducing the LES, it should be required that the wave packet will not suffer significant alteration during the first classical return. In Fig. 3.13 we plot for the same data as in Fig. 3.12 the associated de Broglie wavelength in atomic units for the returning electron wave packet during the first return as a function of birth phase. Since xenon's calculated atomic radius is around 2 au [55], a returning electron wave packet with an associated de Broglie wavelength of 1.5 au is expected to undergo significant diffraction. Under these circumstances, if the second order Born approximation is capable to quantitatively reproduce the LES is unknown.

At this point it is perhaps instructive to present some of the peculiarities of

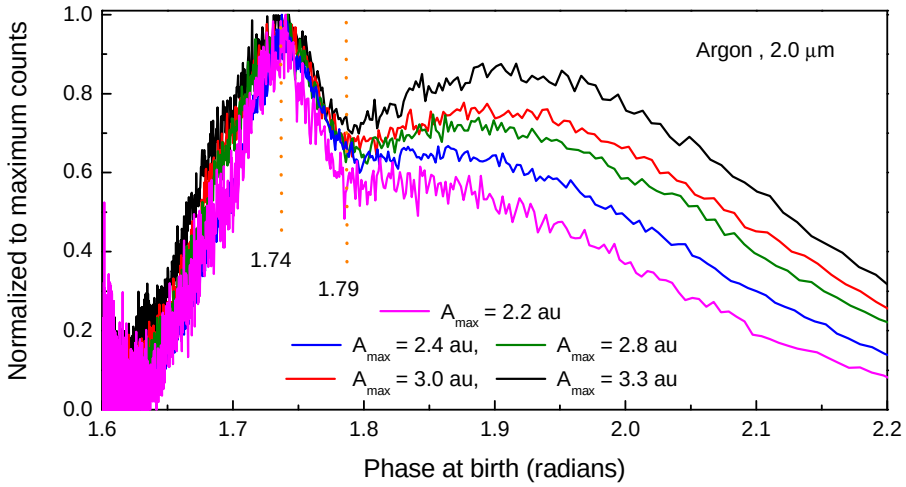

Figure 3.11: **The behavior of the LES as a function of birth phase**. The spectra are the same as in Fig. 3.7. The LES extends up to a phase of 1.79, which is the threshold of the second return and it peaks at 1.74 which is the average phase for the second return. Additionally, the relative height of the LES becomes higher at longer barrier thicknesses indicating an influence of the ballistic electron wave packet spread (see text for details).

the second classical return. The first characteristic of the second return is that of all returns, it is the one that returns at the core with the smallest kinetic energy. Although this fact can be observed in the quantum calculation presented in Fig. 3.1, a simpler explanation can be found from the classical rescattering model, by solving Eq. (1.33). According to this equation, it can be clearly seen that of all returns, the second one returns at the core for the smallest value of the vector potential. Additionally, in terms of electric field strength (which is out of phase with the vector potential) of all classical returns the second one takes place at the highest value of the electric field. There are two immediate consequences. First, due to its lowest kinetic energy, the second classical return is the most susceptible (or "vulnerable") to Coulomb focusing. And second, due to fact that at recollision the electric field is at 80-90% of its maximum value F_0, a new, significant electron wave packet is expected to burst out of the barrier, perhaps interfering with the returning one. If these interferences are strong, their signatures can perhaps be seen in the angular distribution of the photoelectron spectra.

The angular distribution of the LES in the plane perpendicular to the propagation axis of the laser is plotted in Fig. 3.14 for the nitrogen molecule, irradiated with 2.0 μm, 50 fs linearly polarized pulses generating 260 TW/cm^2. To achieve a good

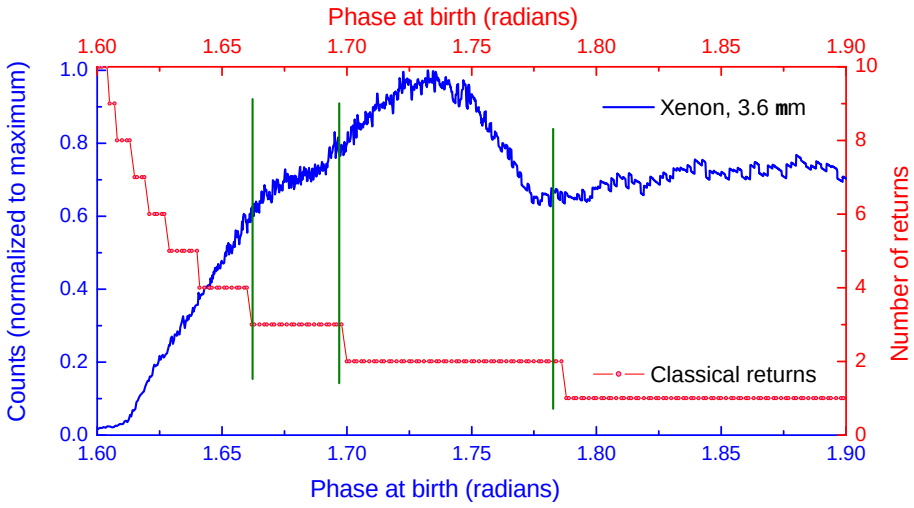

Figure 3.12: **The LES versus the number of returns.** The data is the 3.6 μm spectrum from Fig. 3.6. The graph indicates that the double dip structure of the LES stems from the number of returns the electron wave packet experiences, with the main contribution stemming from the second classical return.

angular resolution, a 1/4 inch pinhole was placed in front of the MCP detector to restrict the collection angle to 1.6 degrees. Then, using a half wave plate designed for 2.0 μm (Foctek Photonics), 300,000 laser shot photoelectron spectra were recorded for each orientation, randomly rotating the laser polarization with respect to the spectrometer axis to cover the range (0,90) degrees in steps of 2 degrees. Prior to this experiment, the wave plate was thoroughly characterized and it was found that covering the range (-90,90) degrees the plot was symmetric around 0 degrees. As a consequence, it was only necessary to cover the (0,90) degrees range and symmetrize the data during analysis. Because we were interested in the plateau photoelectrons as well (which have a low production probability), the symmetrization process was done to improve their statistics and not only for convenience. The result presented in Fig. 3.14 shows a remarkable narrow LES as a function of angle, with its HWHM of approximately 5 degrees. All other targets investigated (atoms and molecules alike) display a similar narrow LES. At the moment, no credible explanation exists for this finding. Purely speculative, perhaps the interference between the plane wave-like wave packet returning at the core for the second time and the more spherical one that is freshly produced plays a role.

To summarize all the investigations performed to clarify the LES and to reinforce its universal nature, in Fig. 3.15 we plot the extent of the LES region given by E_H as a function of the adiabacity parameter γ for helium, argon and xenon at various

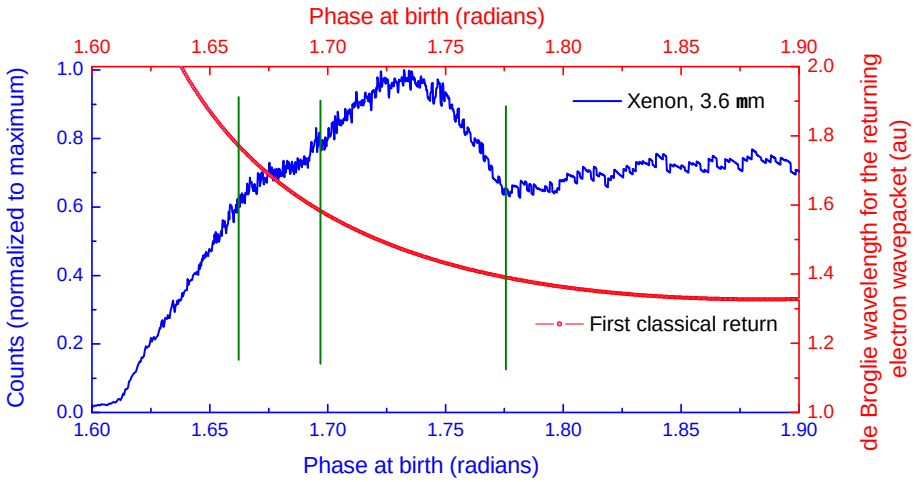

Figure 3.13: **The LES as a function of the phase at birth plotted against the associated de Broglie wavelength at recollision for the first classical return.** The data is the 3.6 μm from Figs. 3.6 and 3.12. The de Broglie wavelength range for this case is comparable with the atomic size, and therefore significant diffraction is expected after recollision.

wavelengths. Over the entire range, the logarithmic plot suggests the LES obeys a simple scaling law $E_H \sim \gamma^{-\alpha}$ with $\alpha \sim 1.8 \pm 0.1$. For $\gamma \leq 0.5$, deep in the tunneling regime, the scaling is excellent despite the strikingly different experimental conditions, e. g. xenon at 3.6 μm scales identically with helium or argon at 2.0 μm. For $\gamma > 0.5$, the data is more scattered, probably because of the gradual passage from tunneling to multiphoton, but the scaling is still a reasonable fit. Once more, the TDSE calculations for helium at 0.8 μm and argon at 2.0 μm closely match the experimental results.

In conclusion, in this section the existence of a new, universal feature was discovered in the tunneling regime, whose existence was not predicted by theoretical models. Based on our extensive investigations the nature of this effect seems connected to rescattering events, perhaps with the Coulomb potential of the ion playing a role. Many questions remain however, necessitating further studies, especially concerning the angular distributions and the universality of the LES. From a practical perspective, the amount of information contained in the LES is not known. Extracting this information could in principle be extremely fruitful. In the case of high harmonic generation for example, it took many years from its discovery to the generation of first isolated attosecond pulses or imaging of molecular orbitals. Since both the LES and HHG are fundamentally linked to rescattering, perhaps it is not too big of a stretch to expect the LES to prove as valuable as HHG. Of course, it has been long

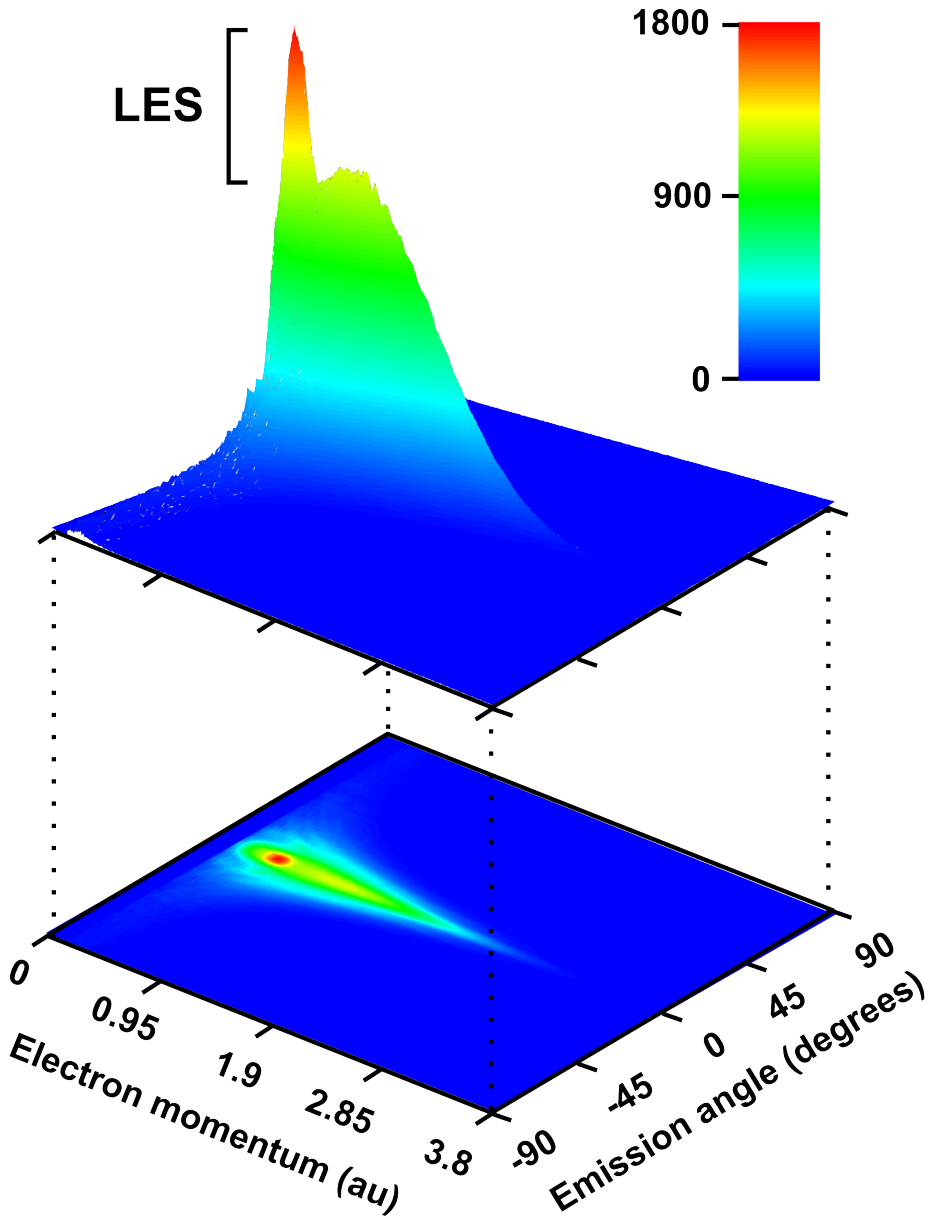

Figure 3.14: **The LES angular distribution in nitrogen.** The intensity is $2.6{\cdot}10^{14}$ W/cm^2 using 2.0 μm, 50 fs linearly polarized pulses. The angular distribution was obtained rotating the polarization of the light in steps of 2 degrees while the collection angle was 1.6 degrees. The angular distribution of the LES is as narrow of $\pm$ 5 degrees (HWHM).

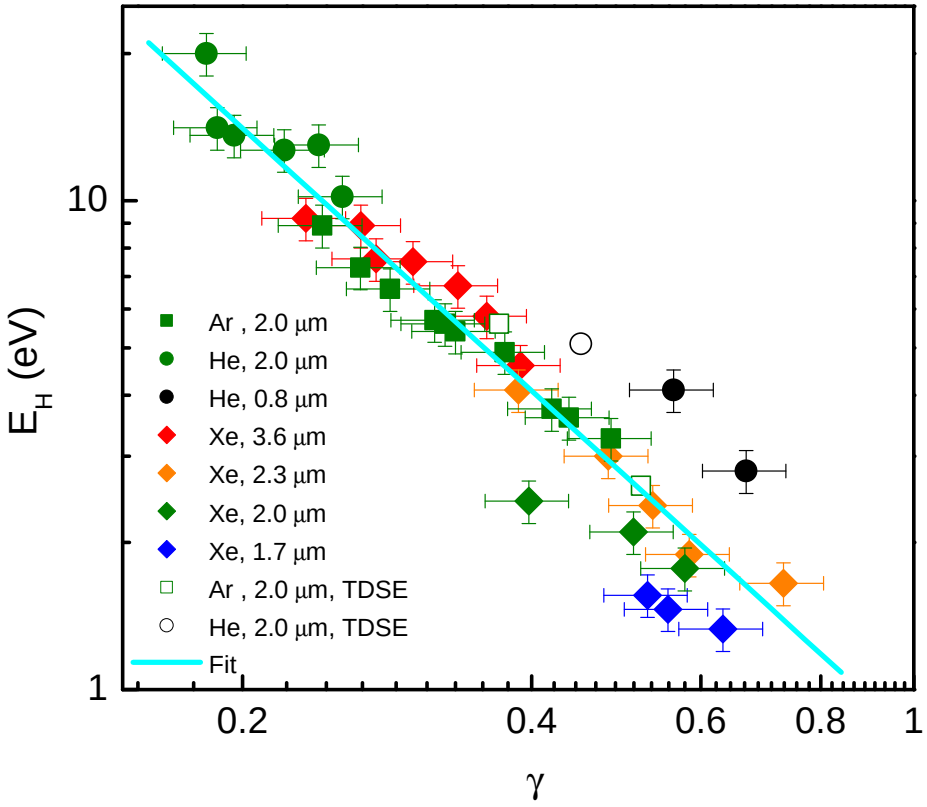

Figure 3.15: **LES mapping for various targets and wavelengths.** The solid line is a linear fit to the data and suggests a scaling law $E_H \sim \gamma^{-\alpha}$ with $\alpha = 1.78 \pm 0.1$. The abscissa error bars are due to a 20% accuracy estimating the laser intensity while the ordinate error bars account for the spectrometer calibration as well as the error in determining the extent of the LES region.

known that the plateau electrons themselves are connected to HHG, but unlike them, the high collection efficiency LES has the potential to be applied in cases where the collection efficiency of the plateau electrons pose practical problems.

****

After this section was written and five months after we reported the LES, Quan et al. [56] experimentally found an LES in xenon, thus confirming its existence. Moreover, the authors' independent analysis using the semi-classical model but including the effect of the Coulomb potential determines that the electron trajectories giving rise to the LES are born after the peak of the field (hence revisiting the core) with initial phases between $\pi/2$ and 1.79 rad for which multiple returns are possible, thus confirming our analysis. However, issues such as the universality and the angular distribution of the LES remain unsolved.

3.3 Laser-driven Electron Diffraction on Atoms and Molecules

In 2004, Itatani et al. [57] reported for the first time the tomographic reconstruction of the highest occupied molecular orbital (HOMO) in the case of N_2 using high harmonic generation (HHG) spectra. Their impressive tomographic technique was based however on certain presumptions, which subsequently came under intense scrutiny, most notably by Le at al. [58]. As outlined in [58], the three main issues that needed further clarifications are i) the limited spectral range, which raised spatial resolution concerns, ii) the limitations stemming from the three-step model for HHG (ionization, propagation and recombination - for an extensive presentation the review article [59] and the references therein is a good starting point) and finally iii) macroscopic effects, since it was assumed that the sample was perfectly aligned and perfect phase matching was achieved.

In [58], the authors suggested that using mid-infrared driving laser fields (as opposed to near-infrared 0.8 μm as it was done in [57]) some of the limitations listed above might be mitigated. Spatial resolution concerns in particular depend on the kinetic energy of the returning electron and we have already seen that due to the λ^2 dependence of the ponderomotive potential the HHG spectral range can be greatly extended, thus improving the spatial resolution. The most intensely scrutinized assumption made in [57] was the critical ingredient consisting of approximating the returning electron wave packet with a plane wave for reconstructing the HOMO of N_2. There are two main reasons to doubt the validity of the plane wave approximation. First, the electron wave packet was born from the HOMO to begin with, so after its return only half a laser cycle later its spread might not have been enough to consider it a plane wave over the volume occupied by the HOMO. And second, even

if during propagation at large distances away from the ion it is a plane wave (say at its turning point), as it approaches the ion the plane wave will be distorted by the electrostatic attraction (Coulomb focusing). At longer wavelengths both effects are likely to be relaxed. The first one, because the propagation time from birth to recollision is longer and therefore the wave packet will spread more. But most importantly, as the kinetic energy of the electron wave packet increases relative to the electrostatic potential at longer wavelengths, Coulomb focusing effects are expected to be smaller and therefore the plane wave approximation should hold water better.

Regardless the correctness of the reconstruction method (and hence the result) as reported by Itatani et al. in [57], the potential scientific rewards for developing the necessary technology to directly view molecular orbitals during chemical reactions cannot be underestimated. The time constraints posed by a camera capable of viewing chemical reactions have been addressed already with the advent of attosecond pulses (Hentschel et al. [60]). As recent as 2008, Li et al. [61] reported time-resolved dynamics in N_2O_4 using HHG. Therefore, the tools required to roll the tape and controlling the frame sequence so to speak have been already developed. From the above discussion however, it is not yet clear how the structural information needs to be recorded on each frame. What is clear though is that since most molecules have low ionization potentials and therefore cannot be submitted to large intensities to generate electron wave packets with large energies (and hence small de Broglie wavelengths), achieving the necessary spatial resolution would require the use of lasers with long wavelengths.

In the introduction to this chapter it was mentioned how diffraction can be used to extract structural information. In the case of ionization in strong fields, since the returning electron wave packet diffracts on its parent ion, the structural information should be embedded in the photoelectron angular distribution. The aim of this chapter is to present high resolution angular distributions at mid-infrared wavelengths and investigate the possibility to extract structural information from them, perhaps as an alternative route (or complementary) to the HHG. The spectra were only recorded at 2.0 μm, for two main reasons. For practical reasons, at the moment we only have half wave plates for this particular wavelength. However, we anticipate that extending our current experimental capabilities should not pose any technological problems, since wave plates for other mid-infrared wavelengths are commercially available. The second limitation is also practical in nature. For a given intensity and target, to obtain spectra with adequate statistics it is necessary to collect data sometimes in excess of 6 hours. Coupled with a similar warm up time for our laser system and the additional time spent on beam alignment, in general it takes a full working day to record a single angular distribution. As we wanted to cover as many targets as possible, we restricted ourselves to only two wavelengths, 0.8 and 2.0 μm. In the future, we plan to extend this wavelength range even further using our 3.6 μm laser system as well.

This section is organized as follows. First, I will briefly present a new theory

whose predictions can be successfully deployed to understand most of the experimental results. Second, I will give the experimental details about how the data was recorded. Third, the method to retrieve electron yields for a given electron momentum (or energy) at rescattering will be presented. Fourth, I will compare the results obtained at 0.8 μm with the ones reported in the literature, proving not only some of the theoretical predictions, but also the robustness of the retrieving method. Finally, the new results at 2.0 μm will be presented for atomic and molecular targets. In connection to the 2.0 μm results, I will reveal a limitation of the 3D TDSE code in the case of argon arising from the choice of the atomic potential. This limitation should not be viewed as a critique or failure of the numerical code, but rather as a testimony to the fact that at its conception by Muller [14] the code was designed with the wavelength of the titanium sapphire in mind. Puzzled at first by this limitation, we quickly realized that the answer opens the door to the exciting world of inner shell atomic and molecular orbitals.

3.3.1 The Quantitative Rescattering Theory

Half a year ago (March, 2009), Chen et al. [69] proposed a new quantitative rescattering theory (QRT) to predict the production and the angular distribution of rescattered photoelectrons as well as HHG spectra. Our research group is involved in studying both phenomena, but since the work performed and reported in this document only dealt with the former, the theoretical background for the latter will not be provided here.

According to the new theory the observed angular distributions for linearly polarized light in momentum space $D(k, \theta)$ are given simply by the product of the momentum distributions for the returning electrons $W(k_r)$ and the elastic differential cross sections (DCS) of free electrons scattering on ions $\sigma(k_r, \theta_r)$:

$$D(k, \theta) = W(k_r)\sigma(k_r, \theta_r), \tag{3.1}$$

where k is the measured electron momentum (after the pulse ended) at an angle θ with respect to the polarization of the light and k_r is the electron momentum at rescattering at an angle θ_r with respect to its direction of propagation before the collision. For linearly polarized light, the electron propagates before the collision along the laser polarization. In the above formula the returning electron distribution can be viewed as a rescattering wave packet (RWP), as the authors suggested in the original paper, thus making the connection with diffraction directly.

Using TDSE calculations for realistic laser pulses at 0.8 μm the behavior of the quantities entering Eq. (3.1) were determined by comparing them with their corresponding counterparts extracted from the second-order strong field approximation

(SFA2) and quantum scattering theories. For RWP, it was found that it changes little from target to target, so for a fixed set of laser parameters differences in the angular distributions of different targets will arise predominantly from differences in the cross sections. In addition, the shape of the RWP is almost identical if extracted from TDSE or SFA2, so whereas the first takes many days to extract RWP given its computation requirements the latter takes minutes. However, the relative amplitude of the two wave packets (TDSE vs. SFA2) is not the same, due to differences in the overall ionization rate. For comparison with experiment however, if one can live with relative values then RWP can be quickly computed with SFA2. The last conclusion about the behavior of RWP is that when averaged over the different intensities present in a real laser focus, the fast oscillations and the complex structure observed for $W(k_r)$ at a fixed intensity flatten out to such an extent that over a wide range of k_r it can be approximated with a constant. The immediate consequence is that from the experimentally determined angular distribution $D(k, \theta)$ a relative elastic cross-section can be extracted (these predictions were also reported by the same team in [62] and [70] and verified experimentally at 0.8 μm by Okunishi et. al in [63]). Alternatively, in [69] the authors also suggest that measuring angular distributions for the same target with different lasers one can attempt to extract relative differences in RWP. To compute the elastic cross section for the collision between a free electron and the ion the authors use the well-known method of partial waves [71] incorporating the long range Coulomb potential ($V_C = 1/r$) as well as a short range potential to account for the multi electronic ionic core. If the plane wave Born approximation was used instead of the partial waves one, the authors warn us that the cross section would be incorrect even at large energies due to the long wave Coulomb potential. However, in SFA2 (which is only used to compute the wave packet and not the cross section) the scattering is taken into account using the Born approximation, which ultimately produces the accuracy limit for the QRT computation as used by its authors.

3.3.2 Experimental details for recording high resolution angular distributions

The setup used to record high resolution angular distributions is presented schematically in Fig. 3.16 (upper left panel). The laser is focused using standard alignment procedures on the time of flight spectrometer's axis with a calcium fluoride (CaF_2) lens with a focal length of f = 100 mm. To control the intensity generated in the focus, the beam is attenuated using neutral density (ND) filters, as opposed to the traditional way of using a power attenuator formed by a polarizer and a half wave plate. The reason for using neutral density filters is that given the wide range of wavelengths we record data at (from 0.8 up to 3.6 μm with a continuous portion between

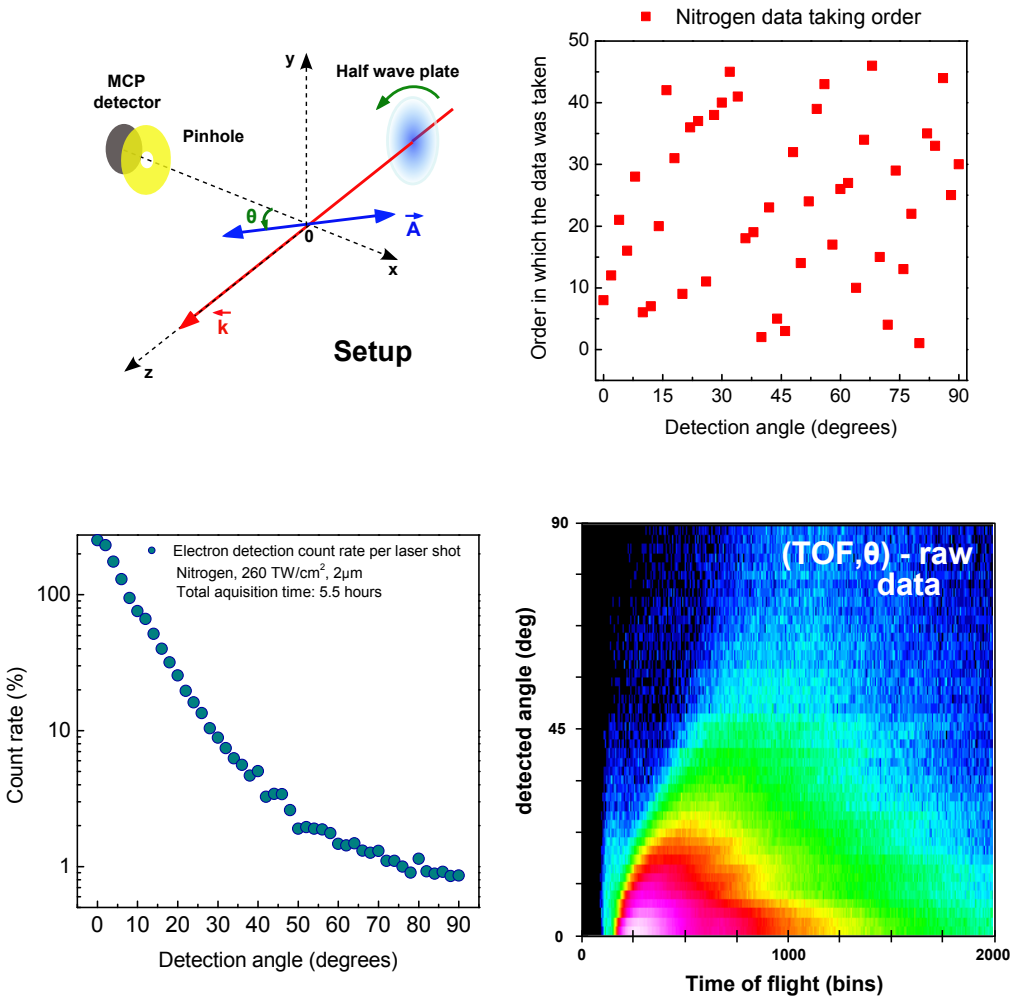

Figure 3.16: **Setup for extraction of laser-driven electron diffraction.** Upper left panel: the experimental setup used for recording time of flight spectra in the x-y plane for different angles θ between the spectrometer axis and the polarization of the light. Upper right panel: the order in which data was collected for each angle (the data at 2.0 μm taken in N_2 is used as an example only). Lower left panel: For the same data set, the count rate was plotted as data was taken. Smooth curves indicate stable experimental conditions. Lower right panel: the raw TOF angular distribution data set, in logarithmic scale.

1.2 to 2.3 μm) power attenuators are not only problematic for handling pulses with very large spectral widths (especially the polarizer) but also costly. Using a known gas as target (usually argon) an electron calibration spectrum is taken at high enough attenuation factors so that saturation is not reached. Then, by the appropriate choice of ND filters, the desired intensity is selected. To rotate the polarization of the light which is in our case by default along the spectrometer's axis we use a half wave plate as indicated in Fig. 3.16. Using the entire area of the MCP detector, the collection angle would have been ± 5.5 degrees (40 mm diameter detector and a flight tube 22.5 cm long). For a better angular resolution, a 0.25 inch pinhole drilled into a molybdenum plate that was subsequently coated with graphite was installed in front of the detector, restricting the collection angle to ± 0.8 degrees. This allowed us to rotate the polarization of the light in steps of 2 degrees without counting twice electrons emitted at any given angle for different orientations of the wave plate in the interval (0,90) degrees. Smaller pinholes are possible to install, but since this will sacrifice the counting rate, the current one provided us with a good compromise. Obviously, given the geometry of the setup, the angular distributions were recorded only for those electrons that are emitted in the plane perpendicular to the laser propagation direction (taken along the z-axis in the upper left panel of Fig. 3.16). The emission however has cylindrical symmetry along the laser polarization if linearly polarized light is used, so the distribution in the x-y plane looks identical to the one in x-z. With the wave plate previously inspected to assure that the count rates at negative angles equal those at positive angles, we recorded spectra from 0 to 90 degrees in steps of two degrees. To remove systematic errors associated with slow drifts in the laser power (usually to the downside) or changing experimental conditions, the order in which the data was taken was randomized using the random function generator supplied with the data analyzing software Origin 7 (by Origin Lab) and the result is plotted in the upper right panel in Fig. 3.16. Plotting the counting rate for each angle as data was taken, smooth curves like the one plotted in Fig. 3.16 (lower left panel) were obtained. Very different count rates for consecutive angles usually meant that experimental conditions had changed and if such an event occurred the entire setup was checked again for consistency. Finally, after the angular distribution was taken for all angles, the TOF data was plotted on an intensity graph in logarithmic scale for a final consistency check before analysis, as it can be seen in the lower right panel in Fig. 3.16.

3.3.3 Procedure for obtaining 2D angular distribution momentum plots and extracting electron yields for a given recollision momentum

Angular-resolved photoelectron spectra in the strong field limit are, of course, nothing new. As early as 1993, our research group (Yang et al. [17]) reported angular distributions in xenon and krypton at 1.05 μm, using 50 ps pulses. The "rings" observed in the angular distribution of xenon at 45 degrees were correctly attributed to rescattering, but since this work came at the same time as the rescattering model was just being developed (also by our group [19] followed by Corkum [20]), in retrospect the choice to plot the recorded distributions in energy rather than momentum hid somewhat the true significance of the result. To understand why momenta plots are a better way to look at angular distributions it is perhaps best to just do so first and discuss the advantages afterwards. The details are illustrated graphically in Fig. 3.17, this time for the case of argon, taken at 170 TW/cm^2 with 0.8 μm.

After the data was collected for each angle, the time of flight data was converted to momenta (in the upper panels of Fig. 3.17 going from left to right). For this transformation, the necessary Jacobian is $J_1 = p^2$, where p is the measured momentum. Next, the data was converted from a (p, θ) plot to a (p_x, p_y) plot, using again the appropriate Jacobian J_2 (which can be easily shown to be $J_2 = p$) and interpolating the angular dependence for all momenta. Different interpolation methods were employed (linear, spline and cubic Hermite - all supplied with the LabVIEW distribution), yielding essentially the same result. This transformation is depicted in the lower left panel in Fig. 3.17. As it was mentioned before, the (p_x, p_y) plot is given for all four quadrants, but the data was only recorded for one and symmetrized for displaying purposes (this was possible only after we checked that each wave plate produces symmetric distributions over the entire range).

Using the rescattering model (with the Simpleman's model included in it), the (p_x, p_y) plot offers us with the possibility to extract the electron yield for a given momentum at rescattering, depicted in the lower right panel of Fig. 3.17. According to the model, direct electrons can have a maximum energy of $2U_P$, residing inside the partially drawn blue circle in the (p_x, p_y) plot. Outside the blue circle, the model predicts that we only have rescattered electrons. The rescattered electrons are also present inside the blue circle, but they are few compared to the direct ones so to extract the angular distribution of rescattered electrons the electrons below $2U_P$ should not be used. The history of the rescattered electron inside the orange square detected with momentum $\vec{p}$ can be easily explained within the framework of the rescattering model. First, following ionization the electron moves to the right, then it is turned around by the laser and impacts the ion with a momentum $\vec{p_r}$ at a phase of the laser field for which the vector potential is $\vec{A}_r$ and finally, it elastically backscatters

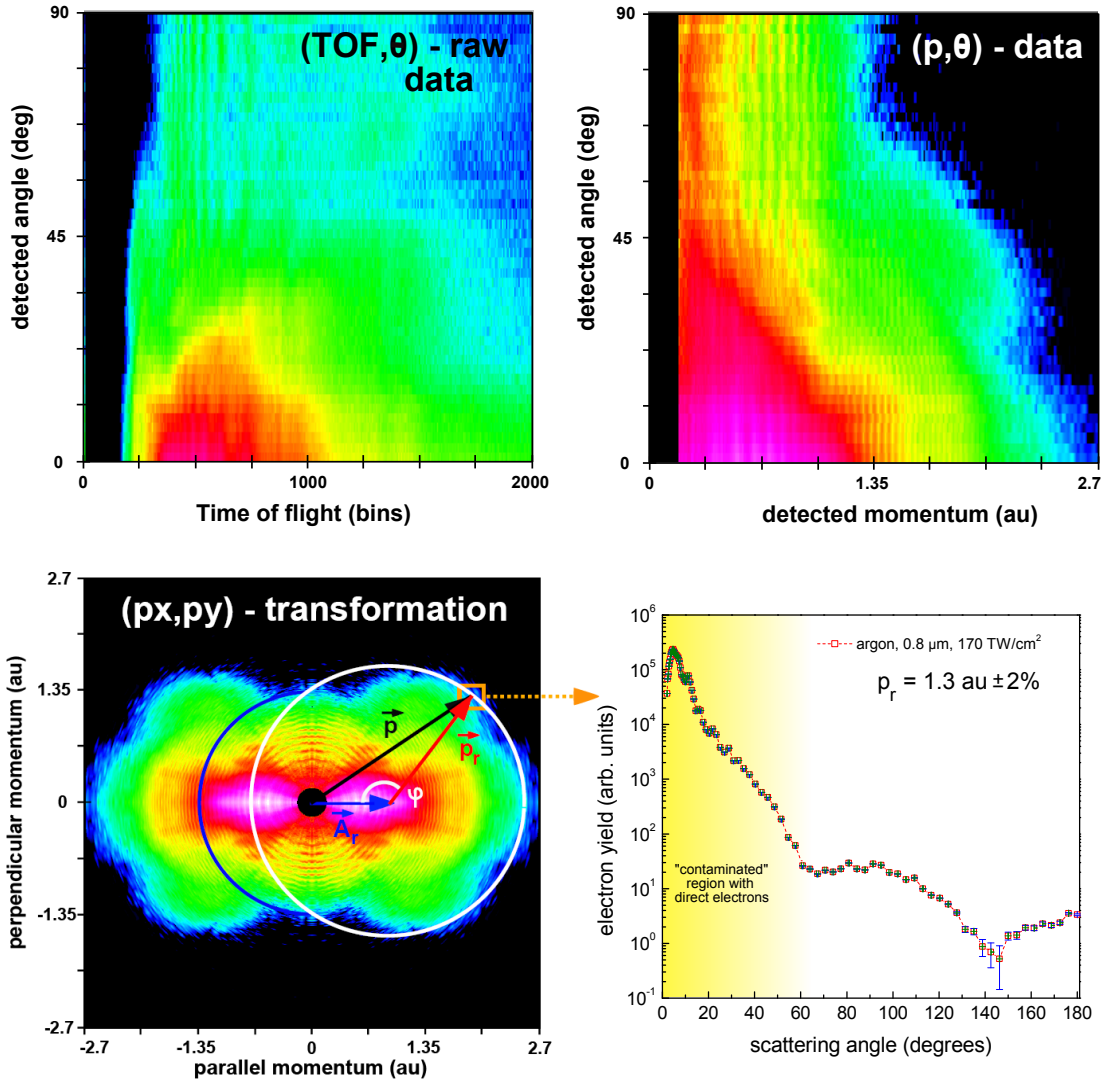

Figure 3.17: **Graphical illustration of the procedures used to extract 2D (p_x, p_y) momentum plots and electron diffraction curves from the TOF data.** Upper panel, left: the measured raw TOF spectra illustrated for the case of argon, 170 TW/cm^2 at 0.8 μm. Upper panel, right: the (p, θ) distribution obtained from the TOF data for the same target. Lower panel, left: the resulting (p_x, p_y) plot after transformation from (p, θ). The electrons inside the orange square are due to rescattering. Their history can be explained assuming an elastic rescattering event with momentum $\vec{p_r}$ during the laser pulse at the instant at which the vector potential is $\vec{A}_r$. Lower right panel: the resulting angular distribution for electrons rescattering with momentum $\vec{p_r}$ at an angle φ.

at an angle φ. Within the rescattering model, assuming that at ionization all electrons are born with the same momentum which is taken to be zero, there is a one to one correspondence between $\vec{p_r}$ and $\vec{A_r}$. In fact, both quantities are uniquely determined by the phase at which the electron was born. As a consequence, counting the detected electrons along the white circle as a function of the rescattering angle we can extract the differential elastic cross-section for the electrons that rescattered with momentum p_r on their parent ion in the presence of the laser field. For this reason, the momentum plots offer a richer picture compared to the energy plots. As suggested by Morishita [62], the quantum equivalent of this simple classical model is a diffraction mechanism, with the returning electron wave packet diffracting on its parent ion. Finally, repeating the above procedure for all birth phases, we can extract 2D diffraction patterns for a given range of rescattering momenta.

Two caveats do exist, however. From the rescattering model, we saw that for the first classical return there are two trajectories (one long and one short) that give the same rescattering momentum. Similarly, for a given final momentum $\vec{p}$, different ($\vec{p_r}$,$\vec{A_r}$) pairs can exist corresponding to long and short trajectories. Additionally, the contribution of multiple returns was also neglected. Fortunately, because not all birth phases are made the same, choosing the right ones can, at least partially, mitigate these two issues. First, as it can be seen from Fig. 3.1, the highest return energy for multiple returns does not cross the $2.5U_P$ level. Therefore, counting for our diffraction pattern only electrons that rescatter with energies above this level, we can completely remove the contributions given by multiple returns. Two options exist to alleviate the uncertainty stemming from the existence of two classical trajectories for the first multiple return. The first and best option is to only count electrons which return with the maximum kinetic energy of $10U_P$, since only one trajectory exists for them. However, at the cutoff the measured yield is very low, so to obtain spectra with good statistics in this region very long data runs are required. The second option is to make use of the exponential law for the tunneling ionization rate. Long trajectories are born near the maximum of the electric field, whereas the short ones are born at later times, when the field is smaller. The ratio between the yields for the long trajectories versus the short trajectories increases with the birth phase difference. Neglecting the preexponential factors in Eq. (1.16), this ratio which will be labeled R is proportional to:

$$R \sim \exp\left[-\frac{2Z^3}{3n^{*3}F_0}\left(\frac{1}{\sin(\phi_{long})} - \frac{1}{\sin(\phi_{short})}\right)\right]. \tag{3.2}$$

For electrons born near the $2.5U_P$ level, the birth phase difference between the long and short trajectories is approximately 0.4 radians, so that the quantity in parenthesis in the above equation is approximately -0.15. In the case of the hydrogen atom, assuming $Z = 1$, $n^* = 1$ and $F_0 = 0.058$ (so that an intensity of 10^{14} W/cm^2

is reached) the ratio R can be estimated to be 5.6. As a consequence, one can only consider long trajectories, since the number of electrons launched along them outnumber the electrons launched along short trajectories by almost 6 to 1. If the intensity is dropped even further, say by a factor of 4, the number of electrons on long trajectories will outnumber the ones on short trajectories by 30 to 1. This effect can actually be observed in Fig. 3.1, comparing the strength of the HHG signal at $2.5U_P$ for the long (curve 1) and short (curve 2) trajectories. To summarize, at intensities below saturation, using only long trajectories with the approximations made in the rescattering model we can extract (or at least attempt to) elastic electron-ion differential cross sections for electrons that return with a kinetic energy slightly above $2.5U_P$.

The procedure used to extract the electron yield as a function of rescattering angle φ for a given momentum at recollision p_r is as follows. First, the desired uncertainty Δp_r is selected, typically few percents. From the rescattering model, assuming the electron is born at rest, for $p_r^{min} = p_r - \Delta p_r$ and $p_r^{max} = p_r + \Delta p_r$ the corresponding vector potentials at rescattering A_r^{min} and A_r^{max} are extracted for the long trajectories alone. Then, from the triangles determined by $(p_r^{min}, A_r^{min}, \theta)$ and $(p_r^{max}, A_r^{max}, \theta)$ the quantities (p^{min}, φ_{min}) and (p^{max}, φ_{max}) are extracted using the law of sines:

$$\frac{p^i}{\sin(\varphi^i)} = \frac{A_r^i}{\sin(\pi - \theta - \varphi^i)} = \frac{p_r^i}{\sin(\theta)}, \tag{3.3}$$

where we used the index $i = min, max$. From the raw TOF file recorded at the angle θ the number of counts $N(\theta)$ detected in the time interval $\Delta t(\theta)$ corresponding to the momentum interval $\Delta p(\theta) = p^{min}(\theta) - p^{max}(\theta)$ is extracted. Again using the appropriate Jacobian $J_3(\theta) = [p(\theta)]^3$ the electron yield for an electron with momentum p_r scattering at an angle $\varphi(\theta) = (\varphi_{min} + \varphi_{max})/2$ is found. Finally, using all TOF files the angular dependence for the yield of elastically rescattered electrons at momentum p_r is found.

The result of this procedure for electrons scattering on argon ions with a momentum equal to 1.3 au and uncertainty ± 2 % is shown in the lower right panel of Fig. 3.17. The plotted error bars on the x-axis are given by $\Delta\varphi = \varphi_{max} - \varphi_{min}$ alone and do not take into account the 1 degree uncertainty associated with the orientation of the wave plate. However, the maximum $\Delta\varphi$ is only 0.64 degrees, which is realized for a rescattering angle of 29 degrees. This angle should actually be ignored in this case, since it is inside the region where direct electrons dominate (the yellow area in the figure). The error bars for the y-axis account only for the number of detected electrons in the interval Δt which in turn is a function of the uncertainty set initially for p_r. Due to the fact that the count rate was low (below 1 hit per shot for most angles) the electrons detected in the above interval come from different laser shots. Consequently, the detection has Poissonian statistics and the relative uncertainty is

simply $\Delta N = 1/\sqrt{N}$ for the N electrons detected in the interval Δt. Experimentally one can record data longer or increase the counting rate by working at higher gas pressure to obtain better statistics. In our case, working at higher pressures was not an option, due to the fact that we were concerned of charge effects in the focal volume since the pressure was already high given the low counting rates imposed by the use of the pinhole. As far as the analysis is concerned, better statistics on the y-axis are possible by increasing the uncertainty in p_r, but this will blur the diffraction pattern increasing the uncertainty on the x-axis. Therefore, for a given distribution a compromise between Δp_r and ΔN was found by a trial and error search.

3.3.4 0.8 μm results

In Figs 3.18 and 3.19 we present a comparison between the reported results of Okunishi et al. [63] against those obtained in our laboratory, following the recipe described above. In [63], the authors had also performed TDSE calculations for both targets using soft Coulomb potentials (taken from Tong and Lin [65]) and compared them against the experimental results. The details of the numerical method are presented in Morishita et al. [66].

In the case of argon, we first note that despite the fact that four different spectra were recorded at four different intensities (230 TW/cm^2 in [63] and 170, 190 and 290 TW/cm^2 in our laboratory) the angular distributions for electrons rescattered with a momentum of 1.3 au look nearly identical, all four presenting the same minimum around 140 degrees. Since the same minimum can also be found in the theoretical model which is a fully quantum mechanical treatment, we can conclude that the simple method based on the classical treatment of the electron is a powerful tool for extracting diffraction minima present in the elastic electron-ion cross sections in strong fields. Although all experimental plots are nearly identical, the theoretical curve does not provide a perfect fit away from the diffraction minimum. There are several reasons why this is the case. As far as the theoretical curve is concerned, it should be remembered that the result is only a single active electron calculation. Since the returning energy of 23 eV is close to the threshold for double ionization (27.63 eV), electron-electron correlations can be at play here. The experimental curves can also be at fault, since to extract them we have used a simple classical model that neglects the effect the ionic Coulomb potential has on the ionized electrons. At this wavelength, the returning electrons have kinetic energies comparable with the strength of the electrostatic Coulomb field, so this is probably a poor approximation. More, for these laser parameters the ionization regime is a mixture of multiphoton and tunneling, so the assumption that the electron is born with zero kinetic energy is also problematic. However, these concerns should not have come as a surprise for the careful reader, since from the HHG history plot (Fig. 3.1) we already knew that at 0.8 μm the

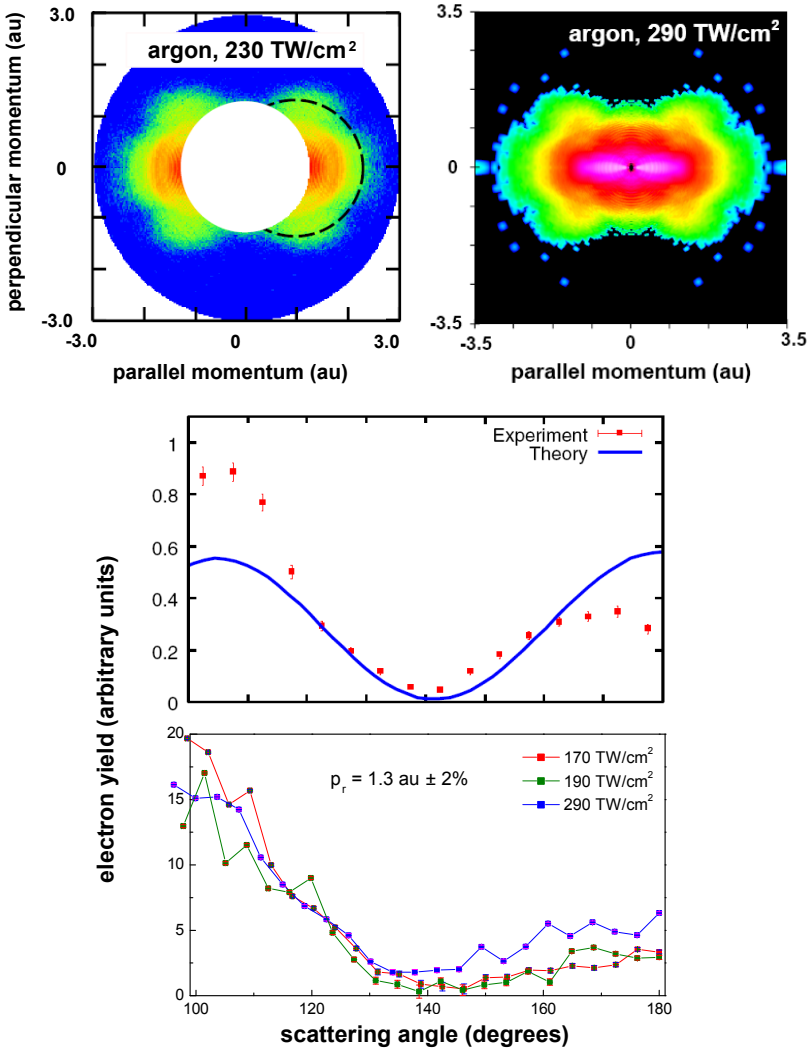

Figure 3.18: **Laser-driven electron diffraction in argon at 0.8 μm.** Upper left panel: the (p_x, p_y) distribution as reported by Okunishi [63]. Upper right panel: the (p_x, p_y) distribution recorded in our laboratory for comparison. Middle panel: the electron diffraction pattern for an electron wave packet rescattering with a momentum of 1.3 au extracted from the distribution given in the upper left panel versus the theoretical curve based on 3D TDSE (also from [63]). Lower panel: electron diffraction patterns for electron wave packets each rescattering with a momentum of 1.3 au extracted from data recorded in our laboratory at three different intensities. The minimum observed at 140 degrees in all experimental curves is a testimony of the robustness of the method.

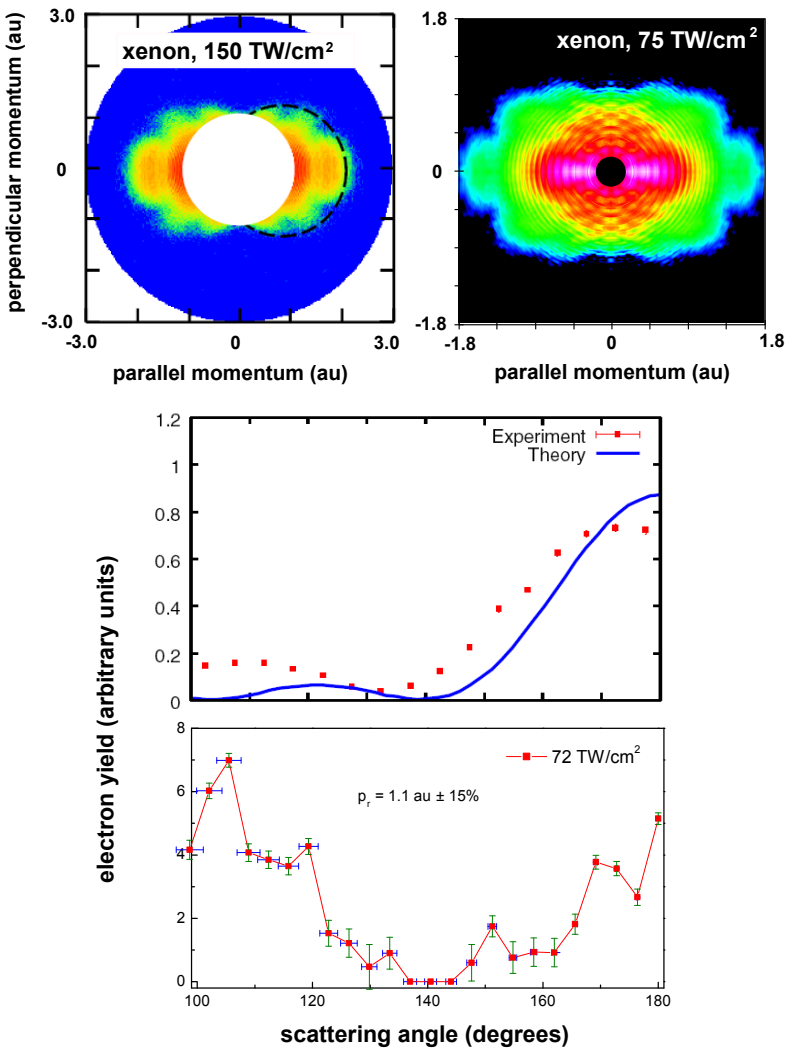

Figure 3.19: **Laser-driven electron diffraction in xenon at 0.8 μm.** Upper left panel: the (p_x, p_y) distribution as reported by Okunishi [63]. Upper right panel: the (p_x, p_y) distribution recorded in our laboratory for comparison. Middle panel: the electron diffraction pattern for an electron wave packet rescattering with a momentum of 1.1 au extracted from the distribution given in the upper left panel versus the theoretical curve based on 3D TDSE (also from [63]). Lower panel: the electron diffraction pattern for an electron wave packet rescattering with a momentum of 1.1 au extracted from data recorded in our laboratory. The position of the minimum observed at 140 degrees in our data as well as the theoretical curve but missed by the experimental curve from [63] is probably due to the fact that in [63] the intensity was above saturation.

classical returns match only qualitatively the quantum result and at the time we have used this finding to justify the use of longer wavelengths. Finally, we also note that each of the four experimental curves were obtained for four different vector potentials at recollision but the same electron momentum at recollision, which is identical with saying that all four curves were obtained using electrons born at different phases of the laser field. As a consequence, the returning electron wave packets are slightly different at recollision, so small changes in the four angular distributions are to be expected. The quantitative rescattering theory presented earlier supports this conclusion and in the original paper [69] the authors show wave packets computed for argon, hydrogen and xenon at two different intensities (100 and 200 TW/cm^2).

This last observation however raises the interesting possibility to try to extract (or reconstruct) returning wave packets from the small changes observed in the experimental curves computed for the same returning momentum but recorded at different intensities (this idea was also suggested in the QRT paper [69]). Another approach is to add a 2ω component (the frequency double of the fundamental driving field) to the fundamental driving field and record angular distributions as a function of delay between the two colors. This last technique was successfully used for HHG when it was shown by Ishii et al. [72] that the returning electron wave packet can be controlled as a function of delay . In principle at least, the $\omega + 2\omega$ technique should work even better for photoelectron angular distributions than for HHG since no macroscopic effects exist.

For xenon, plotted in Fig. 3.19, the conclusions drawn from argon also apply. We have recorded the angular distribution for 75 TW/cm^2, while the experimental curve from Okunishi [63] was recorded at 150 TW/cm^2. In our plot the oscillations are due to the presence of ATI peaks, a testimony of the fact that the Keldysh parameter for our experiment was $\gamma = 1.17$ and therefore a significant multiphoton contribution is present. The multiphoton part also limits the applicability of our method to extract the diffraction pattern for xenon at 0.8 μm, since we assumed a zero kinetic energy for the electron at birth and in the multiphoton regime this is not a good approximation. Regardless, comparing the two experimental curves with the theoretical curve for electrons that return with $p_r = 1.1$ au, we found that our result is actually closer to the theoretical calculation than that of Okunishi [63] for the position of the minimum around 140 degrees. This is probably due to the fact that the experiment in [63] was performed well above the saturation intensity ($I_{sat}^{\mathrm{Xe}} \simeq 80$ TW/cm^2), so their result could be "contaminated" by electrons that rescattered on the Xe^{2+} ion instead of the Xe^+ ion. This "contamination" can take place even below saturation for all targets (atomic hydrogen being the exception), due to nonsequential double ionization. In general however, even for a large atom like xenon, at 0.8 μm the production of the doubly charged ion is rather small, rarely amounting to more than few percent (from Fig. 1.5 for helium near saturation at 0.8 μm it is $\sim 2\%$). The disagreement at angles

closer to 100 degrees also comes from the strong multiphoton component and a close inspection of our (p_x, p_y) plot reveals that the concentric ATI rings extend far beyond the estimated $2U_P$ break.

In conclusion, we have seen that from high resolution angular distributions the diffraction minima for laser-driven electron scattering on ions can be extracted. What is truly remarkable about this technique is that to obtain the experimental diffraction curves only electrons emitted within a window of 0.05 radians were considered (in terms of birth phase). At 0.8 μm, for which the period of the EM wave is 2.5 fs, this time window is only 20 attoseconds, even shorter than the atomic unit of time of 24 attoseconds, representing the period associated with the ground state of the hydrogen atom. It is this time information that is de facto built in that sets laser-driven electron diffraction apart from traditional methods based on electron guns. Additionally, the electron does not only diffract on its parent ion, it self-diffracts, so coherence is also de facto built in (HHG being its direct manifestation).

3.3.5 2.0 μm results

Taking advantage of our experimental capabilities we recorded high resolution angular distributions in several noble gases and molecular targets in the regime where the quantum computation (TDSE) predicts that treating the returning electron classically is a very good approximation. Since from our earlier studies we knew that the number of electrons in the plateau is very low relative to the number of direct electrons for helium and neon at mid-infrared wavelengths, we restricted our study to argon, krypton and xenon (radon was not an option being radioactive). To probe even further into the tunneling regime, in the near future we plan to record angular distributions using the even longer wavelength provided by our 3.6 μm laser system, a system that due to its lower achievable maximum intensity also limits us to the use of argon, krypton and xenon.

In Fig. 3.20 the angular distribution recorded in argon subjected to an intensity of 200 TW/cm^2, generated by 2.0 μm, 50 fs pulses is shown. In the upper panel, the (p_x, p_y) distribution in logarithmic scale is presented, in which the maximum electron momentum of 7.4 au corresponds to the classical (literally and figuratively) $10U_P$ cutoff. In the lower panel, following the same recipe described above the plot on the right presents the extracted angular distribution for electrons that return with a kinetic energy of 100 eV. Since at the moment no theoretical curves based on TDSE or QRT for these laser parameters are available for a direct comparison with the experiment, in Fig. 3.20 (lower panel, left side) the differential electron-neutral elastic cross section (DCS) is plotted directly in the case of argon for the same kinetic energy. The DCS plot was taken from the compilation by Salvat [67], where all experimental data quoted by the author were obtained using the usual electron gun

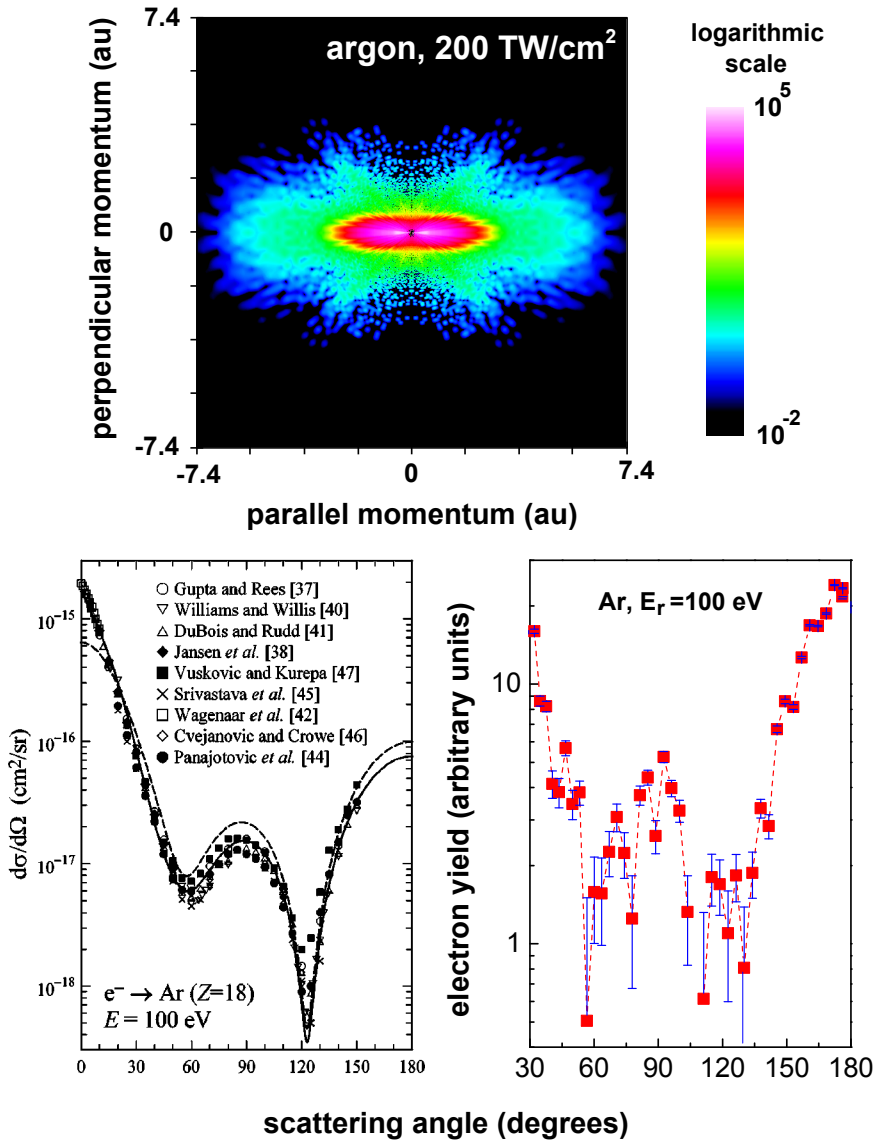

Figure 3.20: **Laser-driven electron diffraction in argon at 2.0 μm.** Upper panel: the (p_x, p_y) plot in logarithmic scale. For direct electrons (red area) the distribution is squeezed along the laser polarization to a higher degree than it was the case at 0.8 μm. The small white region near zero is the LES. Lower panel, left: differential cross sections for field-free e^-+Ar for electrons impacting with 100 eV (taken from [67]). Lower panel, right: laser-driven result for an electron wave packet also returning with 100 eV. The positions of the maxima at 180 and 90 degrees observed in the field-free DCS are perfectly matched in the laser-driven result, stemming from the short-range nature of the collision (see text for details).

(the reader is encouraged to consult the extensive list of references from [67] for details). Surprisingly, the positions of the maxima at 180 and 90 degrees present in the DCS data are also present in the diffraction data retrieved from our angular distribution. The exact positions of the minima around 60 and 120 degrees are not very clear, due to the fact that the statistics in these regions are poor, as it is evident from the vertical error bars. Obviously, the statistics can be improved by taking longer overall runs (one has to remember that the plot presented here took almost 15 hours) or recording data for longer at these particular angles.

In fact, the agreement between the experiment and the differential cross section data is more than just qualitative. In Fig. 3.21 the extracted electron yield obtained for electrons returning with 100 eV from the recorded angular distribution is plotted against the relative differential cross section for elastic scattering of electrons on neutral argon as reported by DuBois and Rudd [68].

The conclusions drawn from argon also apply for krypton, as it can be seen from Fig. 3.22. Except for the different target and intensity, all things are equal for the argon and krypton plots. Once again, the positions of the maxima at 180 and 120 degrees are in the same location for the DCS and laser-driven cases (the maximum at 60 degrees is not clear due to contamination of direct electrons). The statistics are unfortunately not great at large angles so little can be said conclusively about the relative heights corresponding to the maxima (this was also the reason why the error bars were not included but as it can be seen from the (p_x, p_y) plot the maxima are real). At best, integrating over a range of 10 degrees around 180 and 120 degrees a relative ratio $R = \text{yield}(180)/\text{yield}(120) = 1.0 \pm 0.3$ can be found, which is close to the theoretical DCS calculation.

In Fig. 3.23 the data in the case of xenon is displayed. However, no tabulated DCS data at 30 eV was found, but based on the argon and krypton data it is perhaps a reasonable assumption not to expect surprises. A clear minimum around 140 degrees was found for an electron wave packet returning with 30 eV, as it was the case at 0.8 μm for an electron wave packet impacting on the ion with only 16 eV. At 2.0 μm there is however another minimum around 80 degrees, which is not visible at 0.8 μm, most likely because in the later case it was obstructed by direct electrons.

The obvious question that at this point is begging for an answer is why is the rescattered electron yield extracted from the angular distributions so similar with the DCS data since for the former the scatterer was the ion while for the latter it was the neutral atom? The likely explanation rests on the fact that since the kinetic energy of the incoming electron at rescattering (100 eV for argon and krypton) is considerably larger than the binding energy of both the ions and the neutrals, the electron actually penetrates into the ion/neutral in the region of small r where the Coulomb potential is strong. In effect, it is the short not the long range of the Coulomb potential that is responsible for rescattering of the plateau electrons at these energies. As a corollary,

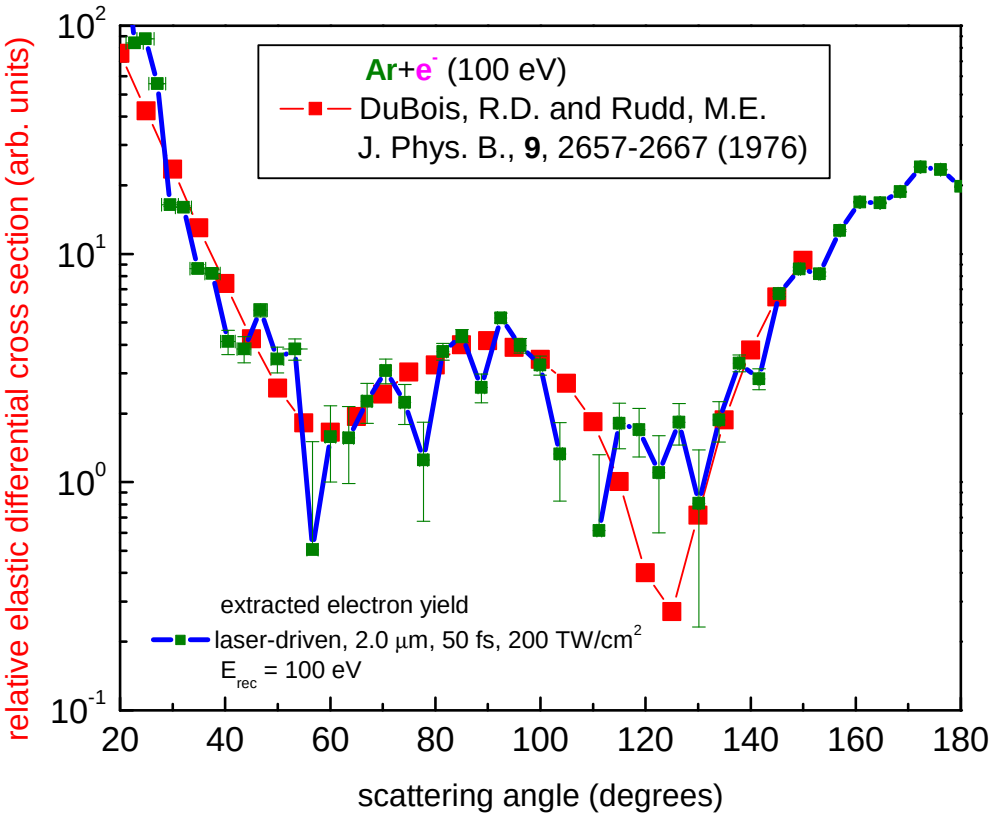

Figure 3.21: **Comparison between the differential cross section for a free electron scattering on neutral argon with 100 eV and the electron yield for laser-driven electron rescattering with the same energy.** The striking similarity is proof that laser-driven electron diffraction at long wavelengths can be used to measure relative elastic cross sections. The laser-driven plot was extracted using the rescattering model for electrons that were emitted and recollided in time windows less than 300 attoseconds. For long wavelengths, due to the fact that the (p_x, p_y) distribution is highly peaked around the laser polarization the contamination with direct electrons manifests itself only at very low scattering angles, thus allowing us to extract elastic cross section over a large range of scattering angles.

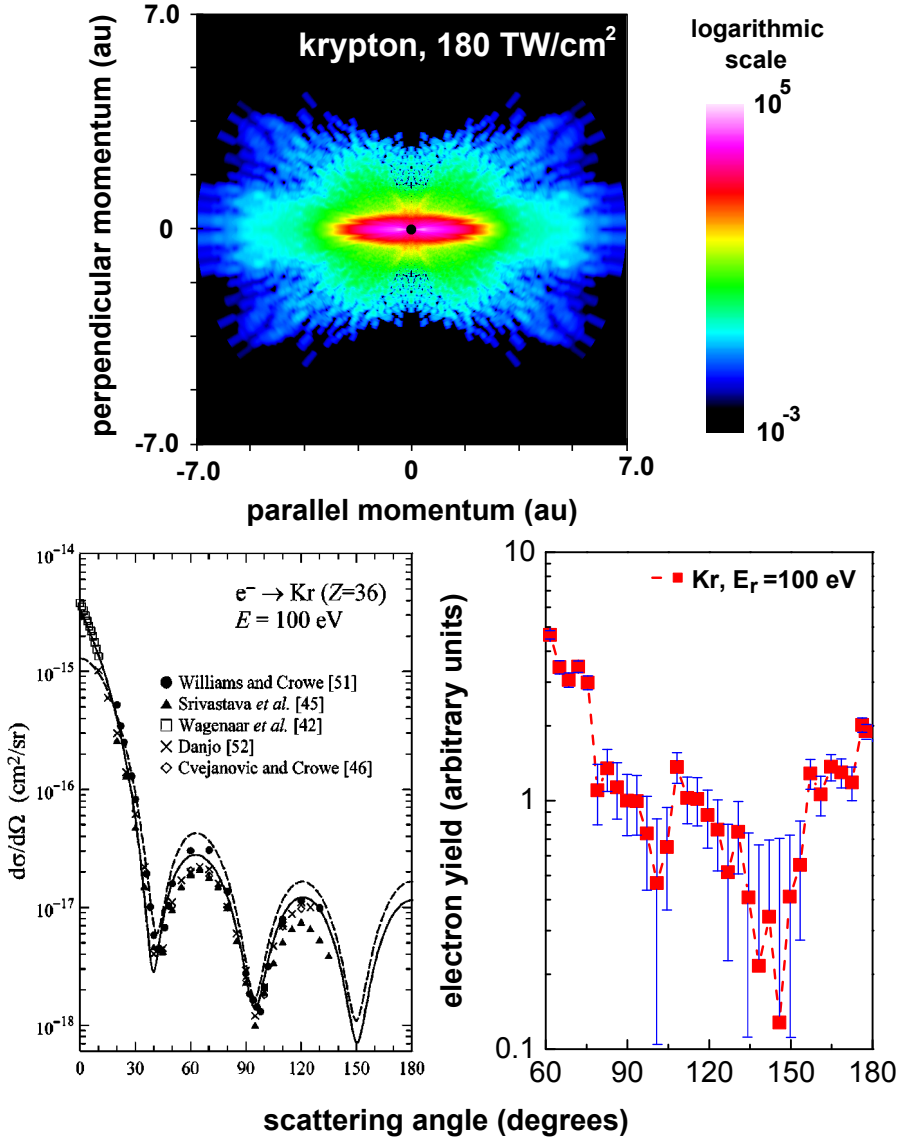

Figure 3.22: **Laser-driven electron diffraction in krypton at 2.0 μm.** Upper panel: the (p_x, p_y) plot in logarithmic scale. The small white region near zero is the LES. Lower panel, left: differential cross sections for field-free e^-+Kr for electrons impacting with 100 eV (taken from [67]). Lower panel, right: laser-driven result for an electron wave packet also returning with 100 eV. The positions of the maxima at 180 and 120 degrees in the field-free DCS are perfectly matched in the laser-driven case, stemming from the short-range nature of the collision. The position of the maximum at 60 degrees is not reproduced, due to contamination with "direct" electrons (see text for details).

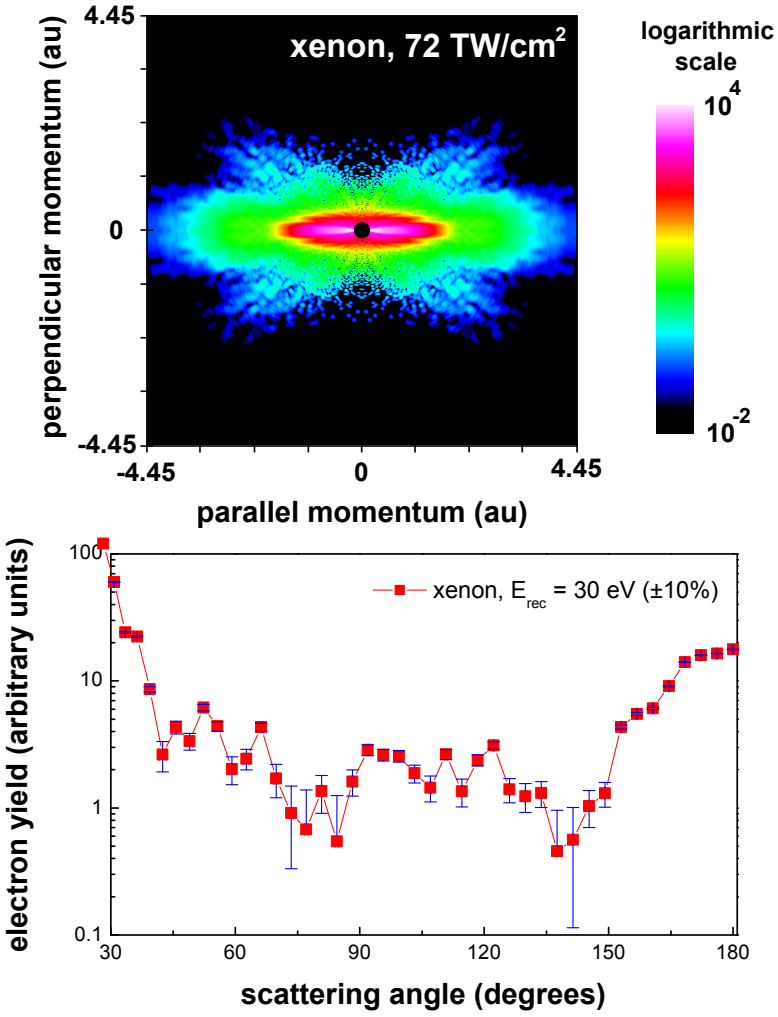

Figure 3.23: **Laser-driven electron diffraction in xenon at 2.0 μm.** Upper panel: the (p_x, p_y) plot in logarithmic scale. The small white region near zero is the LES. Lower panel: laser-driven for an electron wave packet returning with 30 eV.

if the short range of the Coulomb potential is indeed responsible for the shape of the angular distribution at large kinetic energies for the returning electron, then one expects that the presence of the laser field during the collision to have a small effect in determining the shape of the angular distribution, except in determining the shape of the incoming wave packet. In other words, for incoming electrons with large kinetic energies weakly bound orbitals (which are also more delocalized than the inner shell ones) are "transparent". These "transparent" orbitals do however play the role of a Faraday cage, so that tighter bound orbitals which are localized at small r are largely unaffected by the field of the laser, looking identical for both the ion and the neutral with or without the laser. For electrons that return with small kinetic energies, because they are expected to rescatter at larger r, the neutral-electron DCS data and the data from laser driven diffraction should look different, given the fact that weakly bound outer orbitals have large polarizabilities so the laser will "distort" them. Even the incoming electron itself will induce distortions in outer orbitals due to its own Coulomb field, an effect that has been known (and studied) for a long time and theorists have used modified potentials to fit experimental DCS data taken with low energy electrons (reference [67] being one example).

Support for the assumption that the short range of the Coulomb potential is responsible for the observed angular distributions recorded at 2.0 μm was found when the experimental electron yields recorded with linearly polarized light in argon at $0.75{\cdot}10^{14}$ and $1.7{\cdot}10^{14}$ W/cm^2 were compared with the numerical calculation based on 3D TDSE. The comparison is depicted in Fig. 3.24. The experimental curves were taken along the laser polarization using the entire area of the MCP detector, giving a collection angle of ± 5.5 degrees. The numerical result computed for 20-cycle, $\sin^2$ pulses was integrated over ± 6 degrees and spatially averaged over the focal volume of the real laser. For direct electrons (low energy part with the exponentially decreasing electron yield) the agreement between the experiment and the TDSE is excellent for both intensities. For the rescattered electrons (the flat portion in both graphs) the agreement is only reasonable for the lowest intensity whereas at the highest intensity the plateau present in the experimental curve is one order of magnitude higher than for TDSE.

To understand why the TDSE code severely underestimates the production of backscattered electrons at the highest intensity it is necessary to look closer at the numerical details, in particular at the form of the argon atomic potential used in the calculation. As it was mentioned before in the theoretical chapter, the numerical code was designed with the wavelength of titanium sapphire in mind (0.8 μm). At this wavelength, the ponderomotive potential near saturation for argon (250 TW/cm^2) is only 15 eV and therefore the returning electron can have a maximum kinetic energy of 50 eV at rescattering (or a minimum de Broglie wavelength of 3.35 au). When the first numerical results were obtained, the electron spectra were found to have

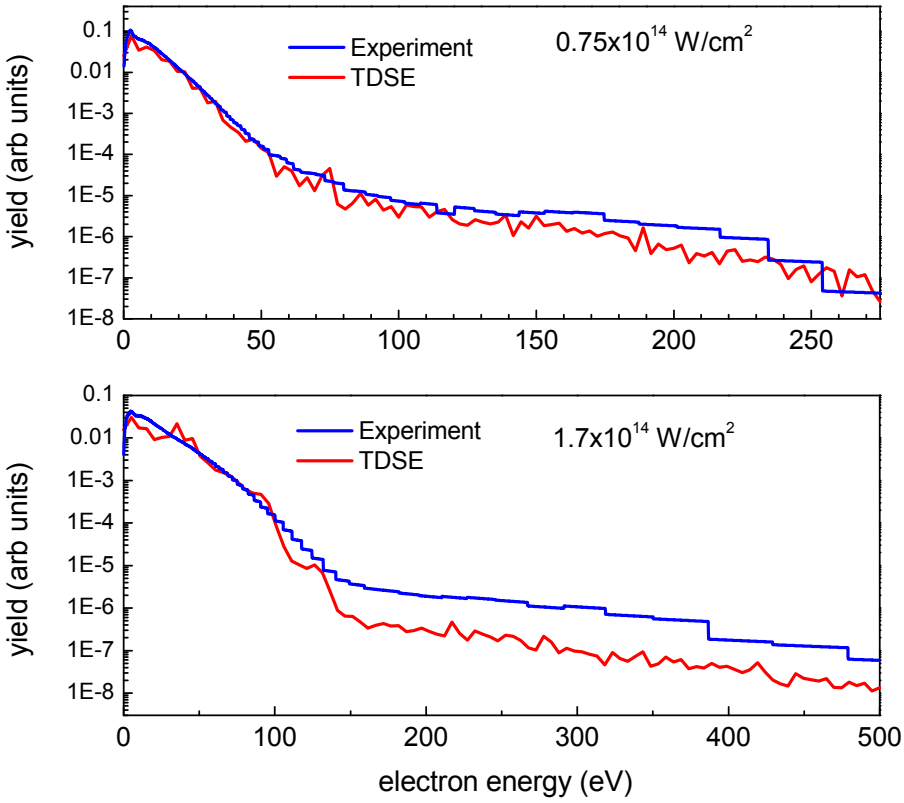

Figure 3.24: **Photoelectron spectra in argon at 2.0 μm along the laser polarization displaying the role of the short range part of the Coulomb potential.** Upper panel: at $0.75{\cdot}10^{14}$ W/cm^2 the 3D TDSE computation matches the experiment very well for direct electrons and fairly well for the rescattered ones (the long plateau region). Lower panel: at $1.7{\cdot}10^{14}$ W/cm^2 the 3D TDSE computation also matches the experiment very well for direct electrons but underestimates the experiment by an order of magnitude in the plateau region. This effect is attributed to the fact that the TDSE employs an atomic potential that does not allow electrons to penetrate the region near the nucleus, so the diffraction of high energy electron wave packets is not properly accounted for (see text for details). The TDSE result was performed using sin^2, 20-cycle pulses and it was spatially averaged over the focal volume and angle-integrated from 0 to 6 degrees to replicate experimental conditions.

very rapid oscillations. These oscillations were attributed to the very short range (and strong) dependence of the atomic potential. To remove these oscillations the potential was cut for $r < 0.5$ au so that the electron wave packet is not allowed to enter this region. Because the de Broglie wavelength associated with the returning electron wave packet at this wavelength is large compared to this restricted zone, the now oscillation-free numerical results matched perfectly the experimental curves. At 2.0 μm however, at the highest intensity presented in Fig. 3.24 the maximum electron return energy is 200 eV, with an associated de Broglie wavelength of 1.6 au. Given that the size of the restricted region ($2r = 1$ au) is larger than half the de Broglie wavelength (0.8 au), not allowing the electron wave packet to enter this region will severely frustrate the diffraction of the electron wave packet and lower the number of backscattered electrons. For the lowest intensity in Fig. 3.24 the maximum electron kinetic energy at recollision is 100 eV giving a de Broglie wavelength of 2.3 au. In this case the diffraction should be more efficient ($2r <$ half the de Broglie wavelength) so the number of backscattered electrons is expected to be closer to the experimental result, which is actually the case. As a future study, it is desirable to properly include the short range of the potential in the TDSE code. This is easier said than done, since it has to be performed carefully so that any modification of the atomic potential will reproduce the positions of the ground state as well as excited states. In addition, thoroughly testing the new potential will take a long time for computational reasons.

To finish the discussion about the accuracy of the TDSE in reproducing experimental results at long wavelengths it should be noted that for HHG the short range part of the Coulomb potential should not prevent one from using the numerical prediction for comparison with the experiment. For HHG, it is the overlap between the wave functions of the returning wave packet and that of the weakly bound ground state that determines the strength of the signal. Since the ground state is delocalized, the short range and diffraction should not be important. There is however one notable exception: the case of multiple returns. For them, during the first return diffraction on the short range does take place, so at subsequent returns the wave function of the returning wave packet should contain the fingerprints of short range diffraction. Most HHG experiments however phase-match only short trajectories and not the long ones (which are the only ones that have multiple returns). Perhaps as future projects, it would be interesting to phase-match long trajectories with their multiple returns and actually look for these short range effects in the HHG spectra (such an experiment might prove quite fruitful for aligned molecules).

3.3.6 Laser-driven Electron Diffraction on Molecules

In 2008 Morishita et al. [64] provided the theoretical proof that for aligned molecules the differential cross section depends on the orientation of the molecu-

lar axis with respect to the direction of propagation of the rescattering electron wave packet. In addition, it was also demonstrated that for a given orientation, the position of the diffraction minima and maxima depend strongly on the internuclear separation. This led the authors to suggest that given the temporal resolution that is built in by default in the sub-cycle electron wave packet dynamics that laser-driven electron diffraction could be used to study molecular transformations as they happen in real time. On the experimental side, Meckel et al. [73] have recently shown (2008) that using the laser-driven electron diffraction method the aligned and antialigned nitrogen and oxygen molecules produce at intermediate rescattering angles diffraction minima and maxima at different positions as a function of molecular alignment. However, the theoretical model used in [73] for predicting the positions of the molecular nuclei agreed rather poorly with their data, again a testimony of the fact that at 0.8 μm the plane wave approximation for the returning wave packet has serious issues.

The goal of the current section is to report angular distributions for molecular targets at 2.0 μm and show that in this case the diffraction pattern extracted from the data agrees remarkably well with the field free cross section for neutral molecules, as it was the case for argon. This is important because if this is the case, then the plane wave approximation at longer wavelengths could be successfully used. The last statement is based on the observation that since neutrals do not have the long range Coulombic tail, if the cross sections in their case agree with the ones from laser-driven diffraction which is an ion-electron process, than in the latter case the effect of the long-range potential is minimal. As a consequence, the tomographic technique employed by Itatani [57] can potentially be used without the suspicions raised at shorter wavelengths.

With the setup and method used for atomic targets, we recorded angular distributions at 2.0 μm for molecular nitrogen, molecular oxygen and carbon dioxide. The resulting (p_x, p_y) distributions are presented with their corresponding intensities in Fig. 3.25. Since the highest intensity was achieved in nitrogen, the statistics for 100 eV rescattering electrons are much better than it was the case for oxygen and carbon dioxide. Therefore, I will restrict our discussion to nitrogen.

In the same paper by DuBois [68] where the absolute differential cross sections for argon were tabulated, the same data was also supplied for molecular nitrogen. Just as was done for argon, in Figs. 3.26 and 3.27 we compare the relative differential cross sections for electrons scattering on neutral nitrogen molecules [68] at 100 and 50 eV with the diffraction patterns obtained in the laser-driven case. Once again, the similarities are striking, proof that relative elastic differential cross sections can be extracted from laser-driven diffraction for molecules, just as it was the case for atoms. The 100 eV result in particular is near picture perfect from 20 degrees to 180 degrees just as it was for argon, whereas the 50 eV result is a bit more qualitative, a testimony once again of the fact the at low energies the long range Coulomb tail

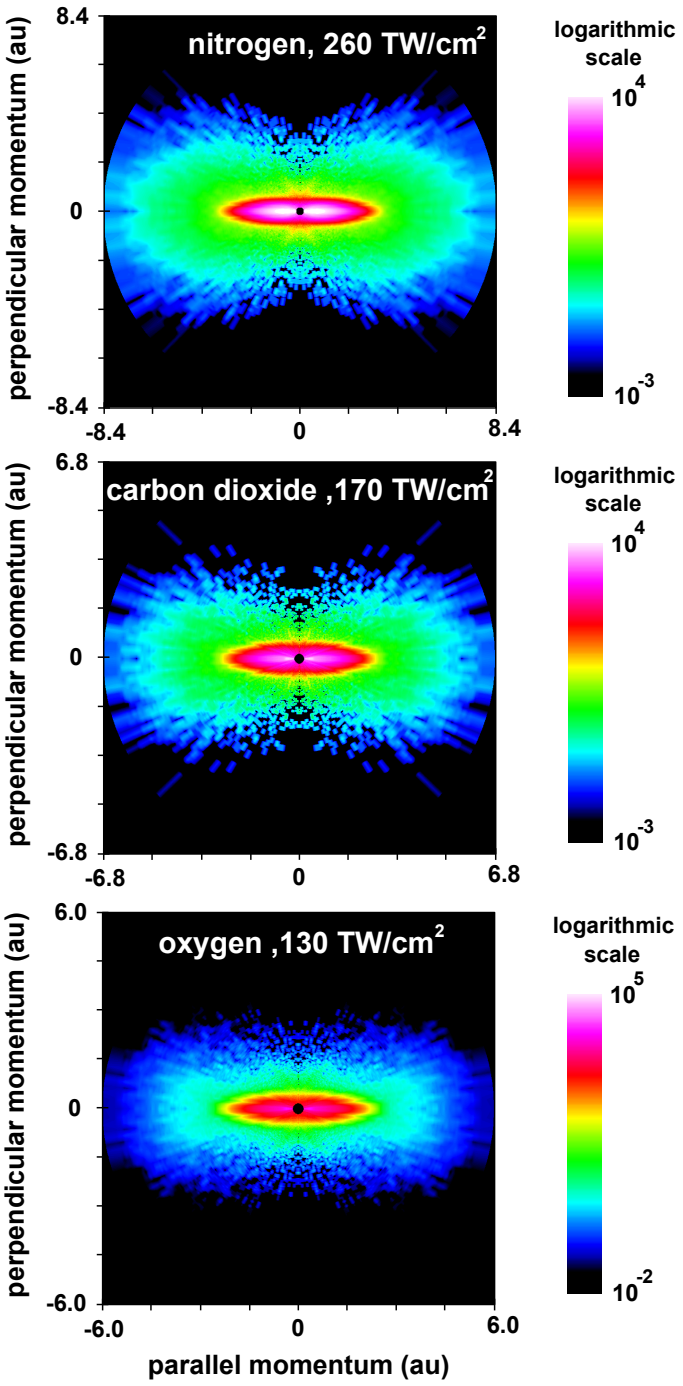

Figure 3.25: **Recorded angular distributions for molecular targets.**

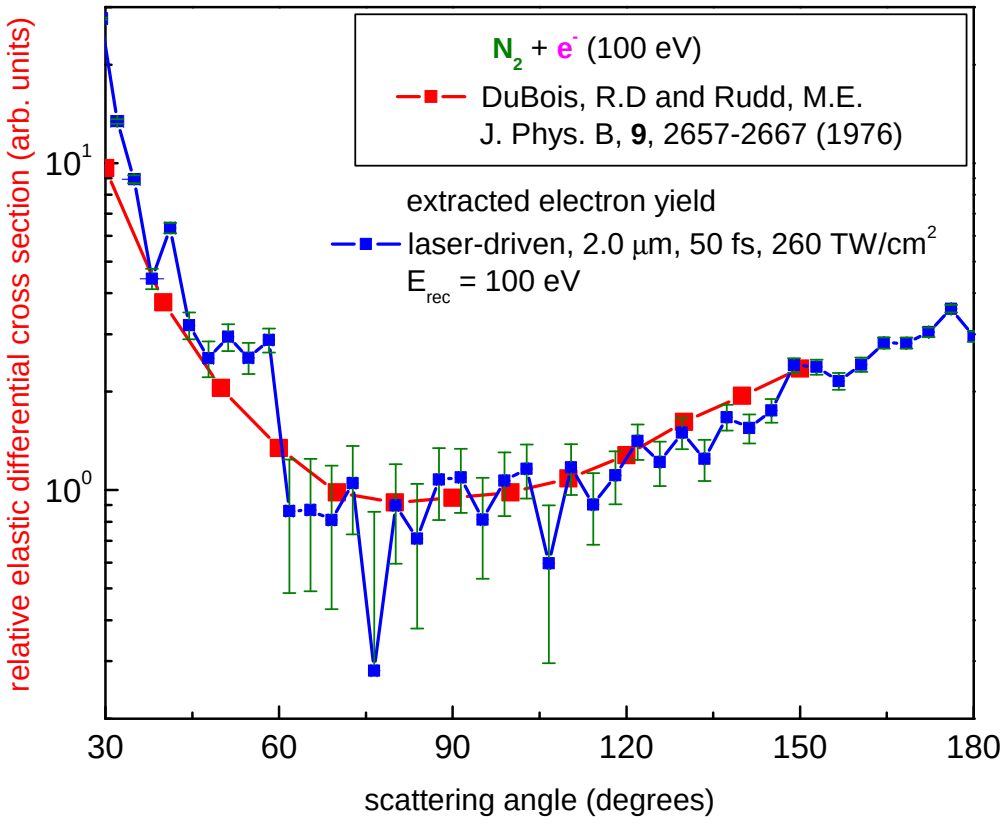

Figure 3.26: **Comparison between the differential cross section for a free electron scattering on neutral molecular nitrogen with 100 eV and the electron yield for laser-driven electron rescattering with the same energy.** The striking similarity is proof that laser-driven electron diffraction at long wavelengths can be used to measure relative elastic cross sections. The laser-driven plot was extracted using the rescattering model for electrons that were emitted and recollided in time windows less than 300 attoseconds. For long wavelengths, due to the fact that the (p_x, p_y) distribution is highly peaked around the laser polarization the contamination with direct electrons manifests itself only at very low scattering angles, thus allowing us to extract elastic cross section over a large range of scattering angles.

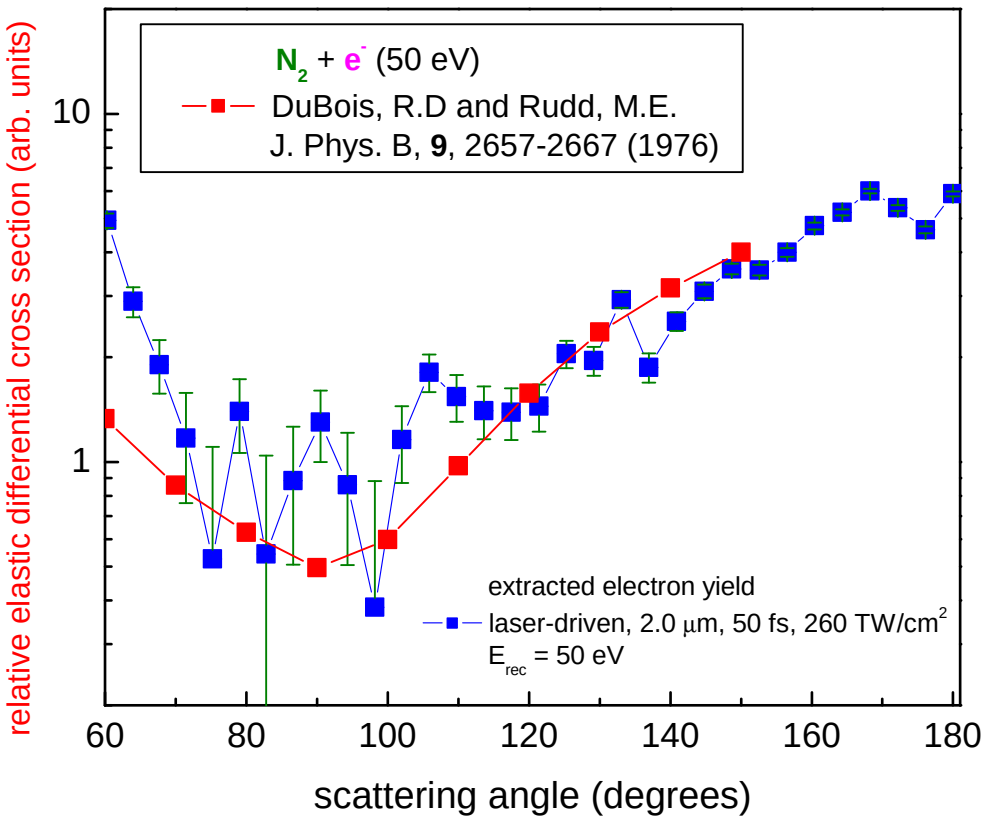

Figure 3.27: **Same as in previous figure, but for an electron scattering at 50 eV.** The disagreement at small angles is due to direct electrons, as they start to contribute to the extracted yield for lower energies.

becomes important. At even longer wavelengths and even larger returning kinetic energies, I expect the agreement between the laser-driven and field-free cases not only to persist, but to get better. In addition, the theoretical prediction from the quantitative rescattering theory that the returning electron wave packet becomes a simple normalization constant when averaged over the intensity distribution of the laser focus is also confirmed.

In the experiments reported by DuBois and our case the molecules were randomly distributed. There is however a difference. According to the theory of molecular tunneling (molecular ADK - see the theoretical chapter), the ionization rate for nitrogen molecules aligned parallel to the field is three times larger than that of randomly oriented molecules. However, in a randomly oriented sample only a small fraction of molecules are perfectly aligned, so the overall effect will be small. As a consequence, as far as detection is concerned, the signal recorded at the detector will have a larger contribution from nitrogen molecules aligned parallel to the polarization of the light, so in a sense the sample will look somewhat aligned. This should lead to minima and maxima in the cross section at different angles for the the aligned and antialigned case, but unfortunately, the statistics are too poor to see this small effect for N_2 and we only measured the overall contributions of both orientations, just as it was the case of DuBois. In the future we plan to align the molecules and see how differential cross sections change as a function of molecular orientation.

Looking at chemical reactions and fast molecular transformations

So how can we use laser-driven electron diffraction to "see" chemical reactions? In Fig. 3.28 the principle of such an experiment is presented. First, let's assume that a laser pulse acting as pump is carefully chosen to induce a chemical reaction $A + \text{pump} \rightarrow B$. Then, sending a short mid-IR pulse (like our 2.0 μm) acting as a time-delay probe before and after the reaction we would record the cross sections of compounds A and B as the reaction unfolds. Of course, the success of such a technique depends how fast the reaction is compared to the durations of the pump but especially the probe. In the chapter were the lasers were presented, we saw that we successfully compressed through filamentation our 2.0 μm pulses from 50 fs to 18 fs with enough bandwidth to support a 12 fs transform limited pulse. Therefore, using as pump a sub 10 femtosecond pulse such as the ones given by our 0.8 μm oscillator and the 18 fs 2.0 μm pulses as probe, we can record the differential cross sections of compounds A and B roughly 15 fs before the reaction and 15 fs after the reaction.

If 15 fs is too long, a different approach can be used. The two figures presenting the differential cross sections for N_2 at 50 eV and 100 eV have far reaching implications when viewed together, from the point of view of at what time they were created, in

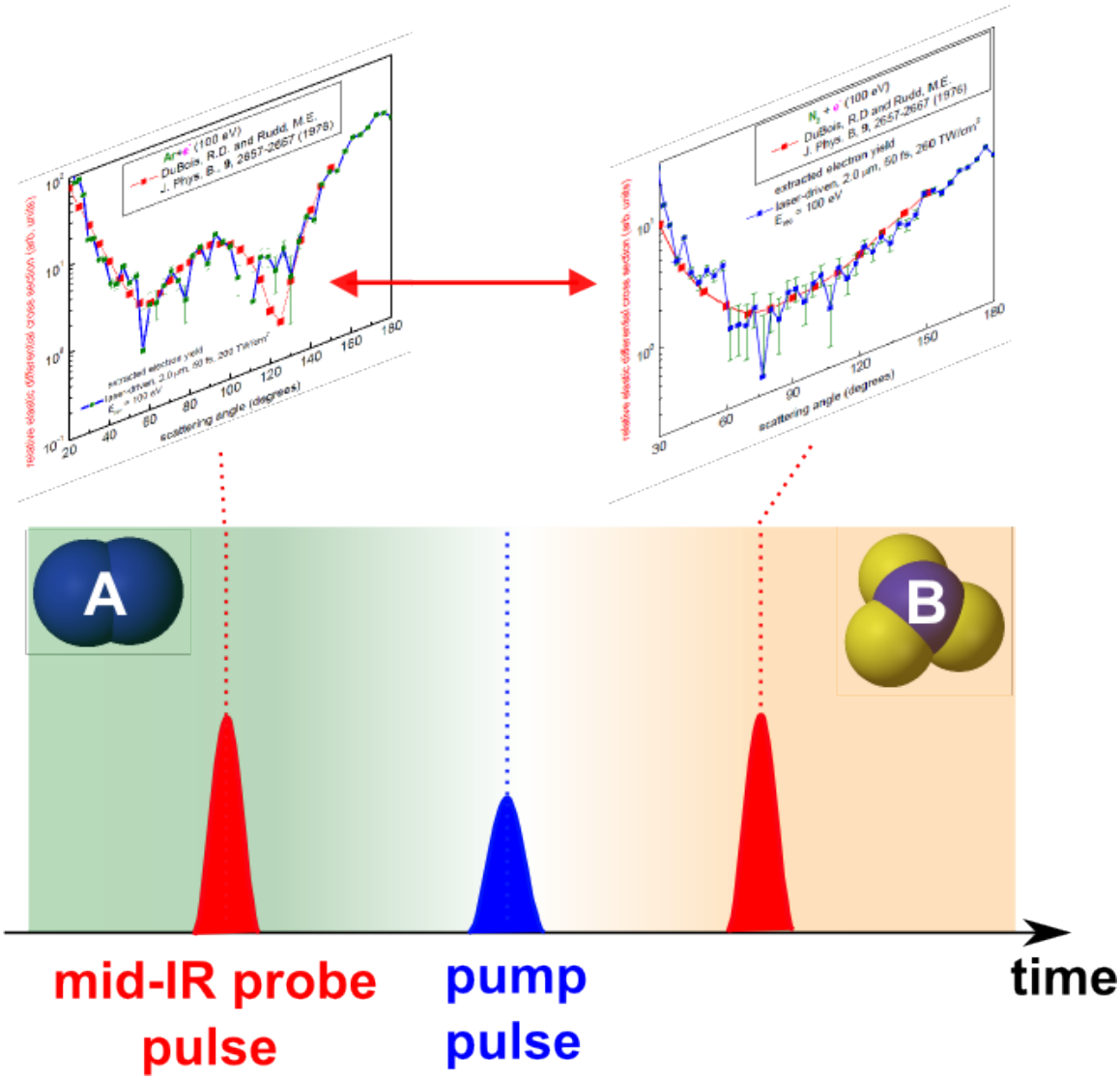

Figure 3.28: **Time resolved chemical reactions.** An ultra short pump pulse (blue) triggers a chemical reaction, changing compound A to B. Then just sending the mid-IR pulse before and after the reaction we can view the diffraction patterns as the chemical transformation takes place.

terms of the phase of the laser field (I will assume a sine field for our discussion, $E = E_0 \sin(\omega t)$). The rescattering model with its classical treatment for the ionized electron is deterministic at its core, and we have used this implicitly and explicitly in the successful extraction of the differential cross section. Let's use it once again, to calculate when the electrons that "recorded" the two diffraction pattern were created and when they rescattered. The 50 eV electron was born at a phase of 1.62 radians, whereas the 100 eV electron was born at 1.59 radians (both were born with zero kinetic energy, the 50 and 100 eV labels were given based on their kinetic energy at rescattering). For a 2.0 μm field this corresponds to a difference in birth times of only 32 attoseconds. However, it is far more interesting to look at when they rescattered. The 100 eV electron arrived first, at a phase $\phi_{100} = 7.12$ radians whereas the 50 eV electron arrived at a phase $\phi_{50} = 7.34$ radians. Therefore, the 100 eV cross section was measured $t_w = 260$ attoseconds earlier than the 50 eV cross section, according to:

$$t_w = \frac{\phi_{50} - \phi_{100}}{\omega}, \tag{3.4}$$

where ω is the angular frequency of the driving laser, which in our case is 0.023 au. The histories of the 50 eV and 100 eV electrons are presented graphically in Fig. 3.29.

In our case, we had the same molecule (N_2) for the entire duration of the pulse. But if we were to insert an XUV attosecond pulse (generated separately through HHG by a portion of the infrared beam that was previously split in two) inside the 260 as window and trigger a fast molecular transformation A+ XUV $\rightarrow$ A*, then the 100 eV electron will detect the diffraction pattern of A, whereas the 50 eV electron will record the diffraction pattern of A*. Even more remarkably, inside the 260 attosecond window t_w arrive electrons with energies in between 50 and 100 eV, and they too record their own diffraction patterns. In effect, in principle we could record the movie of the entire transformation, from start to finish as individual cross sections, seeing not only the initial and final products A and A*, but any intermediate ones created in between. Using even longer wavelengths, not only are the kinetic energies of the returning electrons increasing, but the time window t_w increases as well, allowing us to take longer movies with higher spatial resolution.

3.4 Future studies

Throughout the dissertation we have presented the reader with ideas for future studies. The aim of this section is not to summarize the already proposed future studies, but to unveil several structures that show up in the data and which were not presented already. As the reader might have guessed already, these new structures

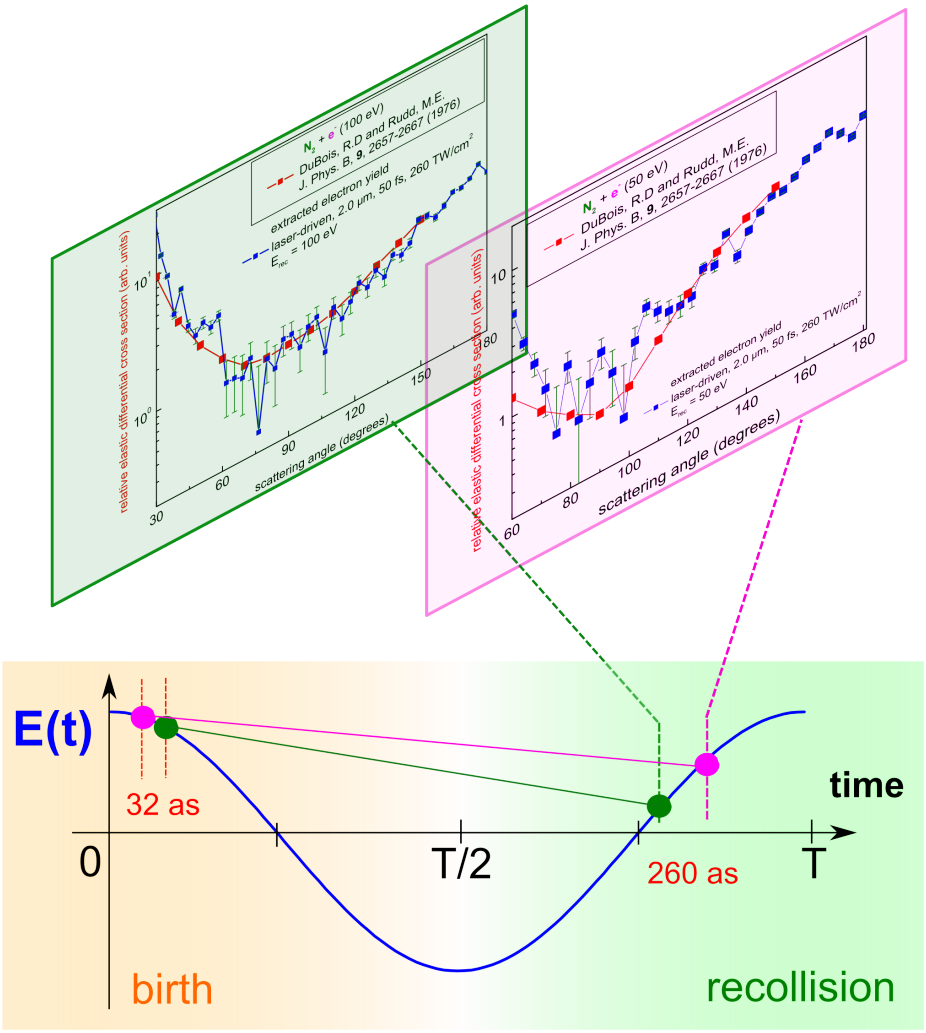

Figure 3.29: **Time resolved electron diffraction on N_2.** The rescattering model, which was successfully deployed to extract the elastic cross sections for 50 and 100 eV also allows to reconstruct the history of the two electrons. The 50 eV electron (magenta) is born first, then 32 attoseconds later the 100 eV (green) one is. At rescattering, when the two diffraction patterns are produced, the 100 eV electron arrives first, then 260 as later the 50 eV one. If a single attosecond probe pulse generated through HHG would be inserted in the 260 as window, then one could see structural changes on this time scale showing up in the two diffraction patterns.

require more investigations and therefore I will just provide the explanation where these structures are found in the data and only a brief idea of what they might be will be given.

Angular rings for direct electrons

In the upper panel of Fig. 3.30 the (p_x, p_y) angular distribution recorded in xenon is presented, this time plotted in linear scale and only for direct electrons (0 to $2U_P$). This is the same data presented in logarithmic scale for all electrons (direct and rescattered) in Fig. 3.25. Looking carefully at the plot in Fig. 3.30, we see a faint flower-like structure present in the distribution. To see it better, in the lower panel of Fig. 3.30 the angular distributions for electrons detected with a given momentum are presented (along circles of constant momentum like the dotted one drawn in the upper panel). The same flower-like pattern was observed in all data sets at 2.0 μm, for all targets and current work is under way to determine its presence at 3.6 μm.

From the lower panel plot in Fig. 3.30 we see that the positions of the maxima shift for different momenta. This fact directly proves that the oscillations are not due to variations in the overall count rate that might have happened if the laser intensity changed during the 5 hr run. Laser drifts are not to blame here for another reason. Two different data sets recorded more than one year apart display the same oscillations, an indication that they are robust and reproducible.

So where are these oscillations coming from? Although more thought and experimental work is required, early indications point to an interference between wave packets launched at different times during the laser pulse. In the theoretical chapter it was mentioned that within SFA the transition amplitude can be written as a sum of two terms, which when squared to get the ionization rate create an interference term (Eq. (1.24)). Equation (1.24) was obtained at constant intensity for an infinite electromagnetic wave, so to apply its prediction to the real data it is necessary to see if averaging over the intensities present in the real laser focus preserves the interference term. In addition, the finite pulse duration and its associated spectral bandwidth would need to be taken into account.

To end this short incursion into the floral realm it is worth pointing why such mechanism is appealing. Interference and diffraction carry information and these flowers should be no different. In fact, even if the above mechanism is not at play here, there is no doubt the shifts in the positions of the maxima as observed in the lower panel of Fig. 3.30 carry information out of the experiment. However, if the flowers are due to interferences between wave packets launched at different times during the pulse, looking at what times they are born can tell us what kind of information can be expected to be extracted. To stay with SFA as presented in the theoretical chapter, I will only consider a monochromatic field (plane wave), which will simplify things

considerably. In this case, the electric field is $E = E_0\sin(\omega t)$ and the vector potential is $A = A_0\cos(\omega t)$. During a cycle, there a two times at which the vector potential has the same value (this was the condition to find the two saddle points in Eq. (1.24)). In Fig. 3.31 a graphical description is provided for one laser period. The two wave packets launched at t_1 and t_2 at the same value of the vector potential will be detected with the same momentum (see the Simpleman's model), but they reach the detector following the trajectories depicted on the side in Fig. 3.31. Wave packet 1 is launched at t_1 and moves away form the core towards the detector. Wave packet 2 is launched at t_2 and first moves in the opposite direction as wave packet 1, then it is turned around, it revisits the core where undergoes forward scattering and then moves toward the same detector as wave packet 1. Then, *at detector* they interfere, displaying maxima and minima as a function of angle. Now the reason why this mechanism is appealing is obvious. Because wave packet 2 revisited the core, it should carry information with it about how forward scattering took place (we can view this as wave packet 2 probed the core). Wave packet 1 also felt the core in its way to the detector, but for a shorter time and perhaps to a lesser degree. Additionally, depending upon the exact phase at which wave packet 2 was born, it is either a long or a short trajectory, but never both. As a consequence, if wave packets 1 can be used as a reference (this is a big if at the moment but from our previous discussions we saw that electrons moving away from the core are well behaved classically which allowed us to extract the cross section), one can attempt to extract the relative phases for short and long trajectories. Given the complexity of the processes involved, more study is needed on this subject and to expect to quickly extract the information carried by these flowers is likely not a realistic expectation. Different angular distributions recorded at various wavelengths and various intensities are required. However, the (p_x, p_y) plot in Fig. 3.30 is in linear scale and unlike the plateau electrons the statistics for these flowers are great, so much shorter scans are necessary, making a detailed study dedicated to them feasible.

The elusive Auger electron

The "classical" Auger process (for a historical perspective see [74] and the references therein) involves in its first step the creation of a vacancy (hole) in the inner shell of an atom or molecule. Then, within few femtoseconds the hole is filled by an electron that occupies a less bound level and to conserve energy and angular momentum a second electron (also from a level less bound than the hole) is ejected. The ejected electron is called Auger electron and determining its energy and angular distribution a great deal of information about the atomic or molecular system can be extracted.

In the earlier section we saw that using high intensity lasers the electron extracted

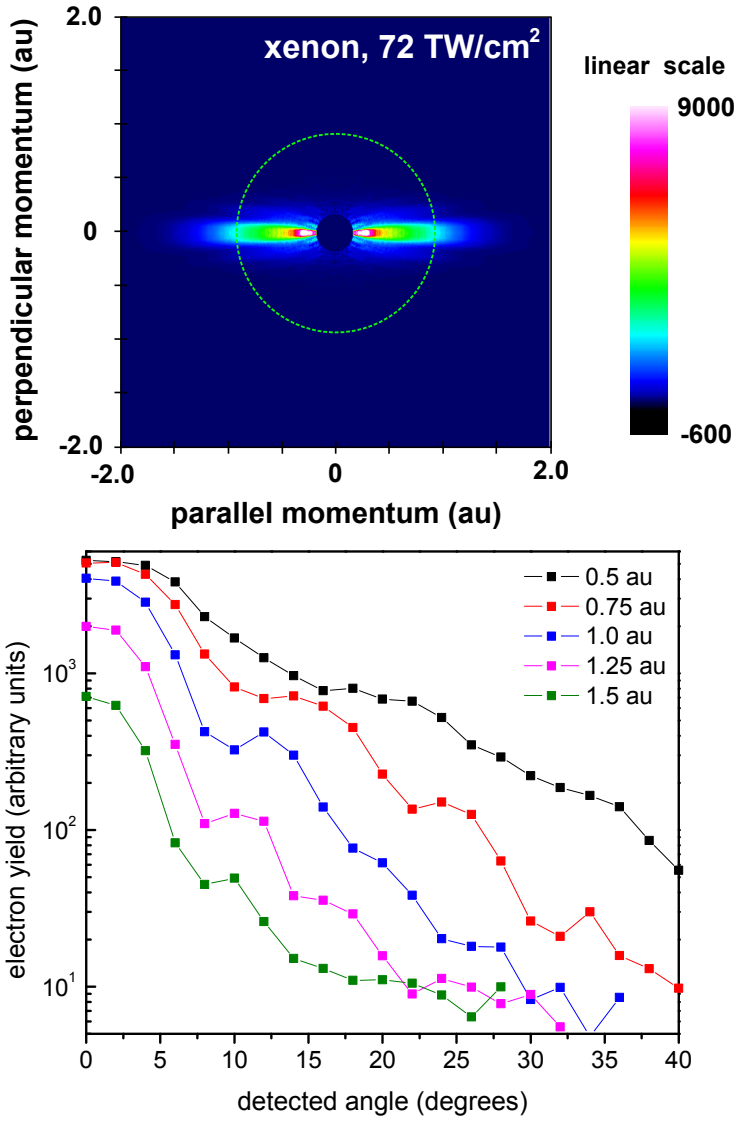

Figure 3.30: **Rings (or flowers) observed in xenon at 2.0 μm.** Upper panel: the (p_x, p_y) plot displayed for direct electrons only (0 to $2U_P$). At small angles a faint flower-like structure depending on the detected momenta is observed. Lower panel: The angular distributions for several measured electron momenta as a function of detection angle. Within the assumptions of the rescattering model, the electrons detected with the indicated momenta correspond to short trajectories so the ions were revisited only once.

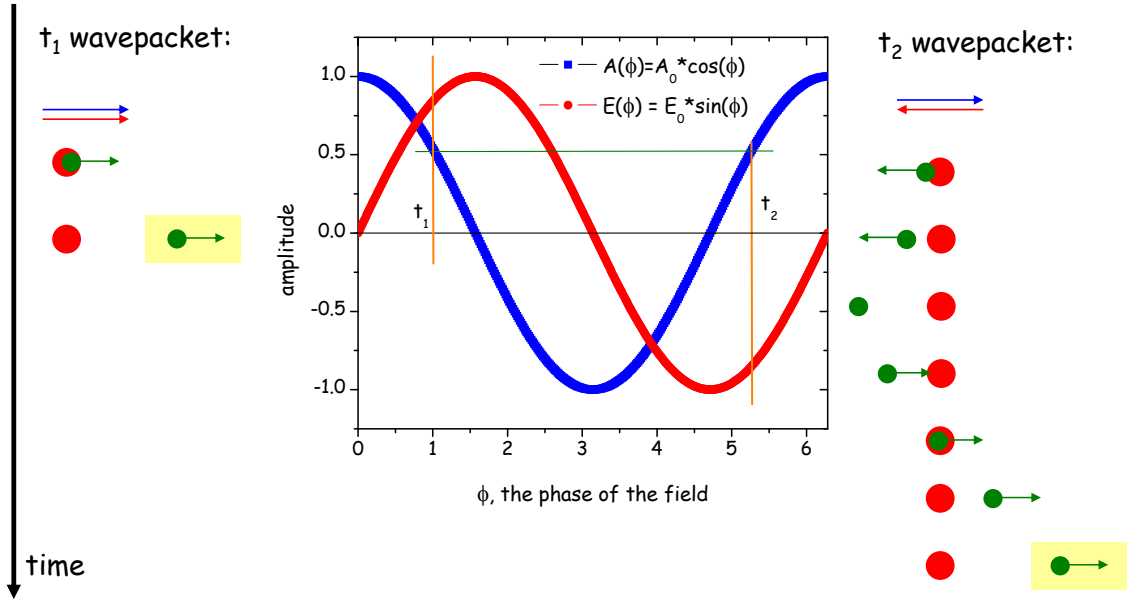

Figure 3.31: **Wave packet interferences between electrons born at the same value of the vector potential.** Wave packets 1 and 2 are born at the same instant value of the vector potential (blue) so they reach the same detector with the same momentum. However, their motion following ionization is different, due to the different values of the electric field (red). As a consequence, their trajectories are different as can be seen on the left and right side of the image. Due to the phase difference between the wave packets, interference maxima and minima will be present as a function of angle at detection.

from the outer shell of an atom or molecule is accelerated by the field and brought back to the parent ion where it elastically rescatters and we have used this process to extract elastic differential cross sections. Using a 2.0 μm source generating 200 TW/cm^2 the angular distribution of argon was presented and the elastic differential cross section extracted for an electron recolliding with 100 eV on its parent ion. At this wavelength and intensity, the maximum kinetic energy the electron can posses at rescattering is 236 eV. If the wavelength and the intensity were to increase even slightly, say 2.2 μm and 250 TW/cm^2, the electron could return with 357 eV. For argon, this last number is well above the binding energy for the $2p$ shell for the neutral as well as the singly charged ion. As a consequence, the possibility to create holes in the inner shell followed by Auger decay should exist. In fact, both our mid-IR sources (the tunable OPA and the 3.6 μm) break the energetic barrier for hole creation. Unfortunately, these inelastic (e,2e) processes usually have small cross sections, but due to the presence of the strong minima observed at certain angles in the elastic cross section one can attempt to find the fingerprint of these inelastic processes by "sitting" exactly at these angles.

However, if we do manage to see the Auger (and we are currently reaching in our bag of tricks and try to do so), this will be a new type of Auger. The reason is very simple and resides in the way the initial hole is created. In previous Auger processes, the hole was created by foreign photons, electrons or other projectiles. In our case however, the laser takes a part of the valence orbital, accelerates it and collides it with the inner shell, creating the hole. And unlike all cases with foreign projectiles, this one should have some level of coherence built in and as a bonus it is on a femtosecond or attosecond scale. If the femtosecond part is clear, perhaps the coherence one is not. One should always remember that argon for example is a multielectronic atom and the true wave function of the system is a combination of all wave functions of all electrons. Therefore, the wave packet that is pulled by the laser in the continuum is not a unielectronic wave packet but a part of the true multielectronic wave function. So when the laser brings it back it "knows" what to find in the inner shell, assuming complete decoherence did not take place and given the fact that we have HHG it is a reason to believe this is true. Of course, the presence of the laser will have to be taken into account, as the Auger electron will be born in it. This complicates the process, shifting the positions and the angular distribution of the Auger electrons, but it also allows the process to occur in the first place and provides the time information.

Chapter 4

Conclusions

In the current document we have investigated atoms and molecules subjected to strong mid-infrared pulses. Using the predictions and results of theoretical models and TDSE numerical computations we demonstrated that treating the ionized electrons within the framework of classical mechanics many phenomena associated with the regime of tunnel ionization can be understood.

In the first part of this dissertation we have investigated in great detail a universal low energy structure (LES) present in the tunneling regime. The electrons comprising part of the LES are born at phases corresponding to the second classical return, pointing to a rescattering mechanism at low kinetic energies. Therefore, for LES electrons Coulombic effects are expected to play a crucial role, but further studies need to be dedicated to uncover the details of this complex mechanism, especially regarding the angular distributions and the universal behavior. In fact, the LES itself can be viewed as forward diffraction of the returning electron wave packet, during the first and during the second return. Additionally, since during the second return the instantaneous electric field of the laser is large, the returning electron wave packet is expected to interfere with a fresh wave packet that tunnels out at the moment of recollision.

In the second part of the document we presented high resolution angular distributions recorded with near-infrared and mid-infrared lasers for atoms and molecules and extracted from them differential cross sections treating the returning electrons as classical particles within the framework of the rescattering model. In the case of near-infrared pulses, qualitative agreement between theoretical predictions and experiment was found. However, using near-infrared pulses the electrons rescatter at low kinetic energies, thus leading to poor spatial resolution. For targets with low ionization potentials (most atoms and molecules) the presence of a strong multiphoton component violates the assumption that electrons are born with zero kinetic energy, severely limiting an accurate retrieval of differential cross sections from the angular distributions. For mid-infrared pulses however, the classical treatment for the ionized electrons and

the assumptions the retrieval model is based on work extremely well. We have found that at large recollision energies the influence of the long-range Coulombic part of the potential becomes small and the extracted differential cross sections are mainly due to the short range of the potential. As a consequence, for both argon and nitrogen molecule the cross sections extracted from the laser-driven angular distribution at 100 eV approach the ones measured for the collision between the electron the neutral target. Finally, based on the classical treatment we estimated that the cross sections extracted successfully for electrons rescattering at 50 eV and 100 eV in the case of nitrogen were "recorded" in the angular distribution 260 attoseconds apart, and we proposed to use this time stamp to build a molecular tunneling camera to study fast molecular transformations with attosecond and sub angstrom resolution.

Bibliography

[1] Shirley, J.H. *Solution of the Schrödinger Equation with a Hamiltonian Periodic in Time.* Phys. Rev., **138**, B979-B987 (1965).

[2] Agostini, P., Fabre, F., Mainfray, G., Petite, G., Rahman, N.K. *Free-Free Transitions Following Six-Photon Ionization of Xenon Atoms.* Phys. Rev. Lett., **24**, 1127-1130 (1979).

[3] Keldysh, L.V. *Ionization in the field of a strong electromagnetic wave.* Sov. Phys. JETP, **20**, 19451950 (1964).

[4] Landauer, R., Martin, T. *Barrier interaction time in tunneling.* Rev. Mod. Phys., **66**, 217-227 (1994).

[5] Fedorov, M.V., *Atomic and Free Electrons In A Strong Light Field.* World Scientific Publishing Co. Pte. Ltd. (1997).

[6] Ammosov, M.V., Delone, N.B., Krainov, V.P. *find title here.* Sov. Phys. JETP, **64**, 1191 (1986).

[7] Bisgaard, C.Z., Madsena, L.B. *Tunneling ionization of atoms.* Am. J. Phys., **72**, 249-254 (2004).

[8] Nikishov, A.I., Ritus, V.I. *find title here.* Sov. Phys. JETP, **23**, 168 (1966).

[9] Delone, N.B., Krainov, V.P. *find title here.* J. Opt. Soc. Am. B, **8**, 1207 (1991).

[10] Ristić, J.M., Stevanović, J.M., Radulović, M.M. *Transition rate dependence on the improved turning point in ADK-theory.* Laser Phys. Phys. Lett., **3**, 298-300 (2006).

[11] Tong, X.M., Zhao, Z.X., Lin, C.D. *Theory of molecular tunneling ionization.* Phys. Rev. A, **66**, 033402 (2002).

[12] Milošević, D.B., Paulus, G.G., Bauer, D., Becker, W. *Above-threshold ionization by few-cycle pulses.* J. Phys. B: At. Mol. Opt. Phys., **39**, R203-R262 (2006)

[13] Nandor, M.J., Walker, M.A., Van Woerkom, L.D., Muller, H.G. *Detailed comparison of above-threshold-ionization spectra from accurate numerical integrations and high-resolution measurements.* Phys. Rev. A, **60**, R1771-R1774 (1999).

[14] Muller, H.G. *Numerical simulation of high-order above-threshold-ionization enhancement in argon.* Phys. Rev. A, **60**, 13411350 (1999).

[15] van Linden van den Heuvell, H. B., Muller, H. G. *Limiting cases of excess-photon ionization.* Multiphoton Processes, Cambridge University Press, 25-34 (1987)

[16] Paulus, G.G., Nicklich, W., Huale Xu, Lambropoulos, P., Walther, H. *Plateau in above-threshold ionization spectra.* Phys. Rev. Lett., **72**, 2851-2854 (1994).

[17] Yang, B., Schafer, K.J., Walker, B., Kulander, K.C., Agostini, P., DiMauro, L.F. *Intensity Dependent Rings in High-Order ATI.* Phys. Rev. Lett., **71**, 3770-3773 (1993).

[18] Walker, B., Sheehy, B., Kulander, K. C., DiMauro, L. F. *Elastic Rescattering in the Strong Field Tunneling Limit.* Phys. Rev. Lett., **77**, 5031-5034 (1996).

[19] Schafer, K.J., Yang, B., DiMauro, L.F., Kulander, K.C. *Above threshold ionization beyond the high harmonic cutoff.* Phys. Rev. Lett., **70**, 1599-1603 (1993).

[20] Corkum, P.B. *Plasma perspective on strong field multiphoton ionization.* Phys. Rev. Lett., **71**, 1994-1998 (1993).

[21] Sola, I.J., Mével, E., Elouga, L., Constant, E., Strelkov, V., Poletto, L., Villoresi, P., Benedetti, E., Caumes, J.-P., Stagira, S., Vozzi, C., Sansone, G., Nisoli, M. *Controlling attosecond electron dynamics by phase-stabilized polarization gating.* Nat. Phys., **2**, 319 - 322 (2006).

[22] Walker, B., Sheehy, B., DiMauro, L.F., Agostini, P., Schafer, K.J., Kulander, K.C. *Precision Measurement of Strong Field Double Ionization of Helium.* Phys. Rev. Lett., **73**, 1227-1230 (1994).

[23] Chaloupka, J.L., Lafon, R., DiMauro, L.F., Agostini, P., Kulander, K.C. *Strong-field double ionization of rare gases.* Optics Express, **8**, 352-357 (2001).

[24] Parker, J.S., Doherty, B.J.S., Taylor, K.T., Schultz, K.D., Blaga, C.I., DiMauro, L.F *High-Energy Cutoff in the Spectrum of Strong-Field Nonsequential Double Ionization.* Phys. Rev. Lett., **96**, 133001 (2006).

[25] Hasović, E., Busuladžić, M., Gazibegović-Busuladžić, A., Milošević, D.B., Becker, W. *Simulation of Above-Threshold Ionization Experiments Using the Strong-Field Approximation.* Laser Physics, **17**, 376-389 (2007).

[26] Dörr, M. *Double ionization in a one-cycle laser pulse.* Opt. Express, **6**, 111-116, (2000).

[27] Dundas, D., Taylor, K. T., Parker, J. S., and Smyth, E. S. *Double ionization dynamics of laser driven helium*, J. Phys. B, **32**, L231 (1999).

[28] Corkum, P.B., Burnett, N.H., Brunel, F. *Above-threshold ionization in the long-wavelength limit.* Phys. Rev. Lett., **62**, 1259 - 1262 (1989).

[29] Wassaf, J., Véniard, V., Taïeb, R., Maquet, A. *Roles of resonances and recollisions in strong-field atomic phenomena: Above-threshold ionization.* Phys. Rev. A, **67**, 053405 (2003).

[30] Maiman, T. H. *Stimulated Optical Radiation in Ruby.* Nature, **187**, 493 (1960).

[31] McClung, F.J. and Hellwarth, R.W. *Giant optical pulsations from ruby.* Journal of Applied Physics, **33**, 828-829 (1962).

[32] Hargrove, L.F., Fork, R.L., Pollack, M.A. *Locking of He-Ne laser modes induced by synchronous intracavity modulation.* App. Phys. Lett., **5**, 45 (1964).

[33] Strickland, D. and Mourou, G. *Compression of amplified chirped optical pulses.* Opt. Commun., **56**, 219221 (1985).

[34] Kane, S.J., Applied Physics, University of Michigan Press, Ann Arbor, MI, 137 (1996).

[35] Krausz, F. and Ivanov, M. *Attosecond physics.* Rev. Mod. Phys., **81**, 163-233 (2009).

[36] Couairon, A. and Mysyrowicz, A. *Femtosecond filamentation in transparent media.*, Physics Reports, **441**, 47 189 (2007).

[37] Backus, S., Durfee, C. G. III, Murnane, M. M., Kapteyn, H. C. *High Power Ultrafast Lasers.* Rev. Sci. Instrum., **69**, 1207 (1998).

[38] Walmsley, I., Waxer, L. and Dorrer, C. *The role of dispersion in ultrafast optics.* Rev. Sci. Instrum., **72**, 1 (2001).

[39] Boyd, R.W. *Nonlinear Optics.* Academic Press, Third Edition (2008).

[40] Kasparian, J., Rodriguez, M., Méjean, G., Yu, J., Salmon, E., Willie, H., Bourayou, R., Frey, S., Andreé, Y.-B., Mysyrowicz, A., Sauerbrey, R., Wolf, J.-P., Wöste, L. *White-Light Filaments for Atmospheric Analysis.* Science, **301**, 61-64 (2003).

[41] Hauri, C.P., Kornelis, W., Helbing, F.W., Heinrich, A., Couairon, A., Mysyrowicz, A., Beigert, J., Keller, U. *Generation of intense, carrier-envelope phase-locked few-cycle laser pulses through filamentation.* Appl. Phys. B, **79**, 673677 (2004).

[42] Hauri, C. P., Lopez-Martens, R. B., Blaga, C. I., Schultz, K. D., Cryan, J., Chirla, R., Colosimo, P., Doumy, G., March, A. M., Roedig, C., Sistrunk, E., Tate, J., Wheeler, J., DiMauro, L. F., Power, E. P. *Intense self-compressed, self-phase-stabilized few-cycle pulses at 2 μm from an optical filament.* Opt. Lett., **32** 7, 868-870 (2007).

[43] Ranka, J.K., Gaeta, A.L., Baltuska, A., Pshenichnikov, M.S., Wiersma, D.A. *Autocorrelation measurement of 6-fs pulses based on the two-photon-induced photocurrent in a GaAsP photodiode.* Opt. Lett., **22**, 1344-1346 (1997).

[44] Nicholson, J.W., Rudolph, W. *Noise sensitivity and accuracy of femtosecond pulse retrieval by phase and intensity from correlation and spectrum only (PICASO).* J. Opt. Soc. Am. B, **19**, 330-339 (2000).

[45] Kakehata, M., Takada, H., Kobayashi, Y., Torizuka, K., Fujihira, Y., Homma, T., Takahashi, H. *Single-shot measurement of carrier-envelope phase changes by spectral interferometry.* Opt. Lett. **26**, 1436-1438 (2001).

[46] O'Hanlon, J.F. *A User's Guide to Vacuum Technology.* Third Edition, John Wiley & Sons, Inc (2003).

[47] Wiza, J.L. *Microchannel plate detectors.* Nucl. Instr. and Methods, **162**, 587-601 (1979).

[48] Colosimo, P. *A Study of Wavelength Dependence of Strong-Field Optical Ionization.* PhD thesis, Stony Brook University (2007).

[49] March, A.M. *Strong Field Studies of Cesium Using Intense Mid-infrared Light.* PhD thesis, Stony Brook University (2009).

[50] Muller, H.G. *Coulomb focusing in resonant production of super-ponderomotive photo-electrons from helium.* Opt. Exp., **8**, 86-91 (2001).

[51] Yakovlev, V.S., Scrinzi, A. *High Harmonic Imaging of Few-Cycle Laser Pulses.* Phys. Rev. Lett., **91**, 153901 (2003).

[52] Tate, J., Auguste, T., Muller, H.G., Salières, P., Agostini, P., DiMauro, L.F *Scaling ofWave-Packet Dynamics in an Intense Midinfrared Field.* Phys. Rev. Lett., **98**, 013901 (2007).

[53] Colosimo, P., Doumy G., Blaga, C.I., Wheeler, Hauri, C, Catoire, F., Tate, J., Chirla, R., March A.M., Paulus, G.G., Muller H.G., Agostini, P., DiMauro, L.F. *Scaling strong-field interactions towards the classical limit.* Nat. Phys., **4**, 386-389 (2008).

[54] Blaga, C.I., Catoire, F., Colosimo, P., Paulus, G.G., Muller, H.G., Agostini, P., DiMauro, L.F. *Strong-field photoionization revisited.* Nat. Phys. **5**, 335-338 (2009).

[55] Clementi, E., Raimondi, D.L. *Atomic screening constants for SCF functions.* J. Chem. Phys., **38**, 2686-2689 (1963) and Clementi, E., Raimondi, D.L., Reinhardt, W.P. *Atomic screening constants for SCF functions II. Atoms with 37 to 86 electrons.* J. Chem. Phys., **47**, 1300-1307 (1967).

[56] Quan, W., Lin, Z., Wu, M., Kang, H., Liu, H., Liu, X., Chen, J., Liu, J., He, X.T., Chen, S.G., Xiong, H., Guo, L., Xu, H., Fu, Y., Cheng, Y., Xu, Z.Z. *Classical Aspects in Above-Threshold Ionization with a Midinfrared Strong Laser Field.* Phys. Rev. Lett., **103**, 093001 (2009).

[57] Itatani, J., Levesque, J., Zeidler, D., Niikura, H., Pépin, H., Kieffer, J.C., Corkum, P.B., Villeneuve, D.M. *Tomographic imaging of molecular orbitals.* Nature, **432**, 867-871 (2004).

[58] Le, V.H., Le, A.-T., Xie, R.-H., Lin, C.D. *Theoretical analysis of dynamic chemical imaging with lasers using high-order harmonic generation.* Phys. Rev. A, **76**, 013414 (2007).

[59] Brabec, T. and Krausz, F. *Intense few-cycle laser fields: Frontiers of nonlinear optics.* Rev. Mod. Phys., **72**, 545-591 (2000).

[60] Hentschel, M., Kienberger, R., Spielmann, Ch., Reider, G.A., Milosevish, N., Brabec, T., Corkum, P., Heinzmann, U., Drescher, M., Krausz, F. *Attosecond Metrology.*, Nature, **414**, 509-513 (2001).

[61] Li, W., Zhou, X., Lock, R., Patchkovskii, S., Stolow, A., Kapteyn, H., Murnane, M.M. *Time-Resolved Dynamics in N_2O_4 Probed Using High Harmonic Generation.* Science, **21**, 1207-1211 (2008).

[62] Morishita, T., Le, A.-T., Chen, Z., Lin, C.D. *Accurate Retrieval of Structural Information from Laser-Induced Photoelectron and High-Order Harmonic Spectra by Few-Cycle Laser Pulses.* Phys. Rev. Lett., **100**, 013903 (2008).

[63] Okunishi, M., Morishita, T., Prümper, G., Shimada, K., Lin, C.D., Watanabe, S., Ueda, K. *Experimental Retrieval of Target Structure Information from Laser-Induced Rescattered Photoelectron Momentum Distributions.* Phys. Rev. Lett., **100**, 143001 (2008).

[64] Morishita, T., Le, A.-T., Chen, Z., Lin, C.D. *Potential for ultrafast dynamic chemical imaging with few-cycle infrared lasers.* New J. of Phys., **10**, 025011 (2008).

[65] Tong, X.M. and Lin, C.D. *Empirical formula for static field ionization rates of atoms and molecules by lasers in the barrier-suppression regime.* J. Phys. B: At. Mol. Opt. Phys., **38**, 25932600 (2005).

[66] Morishita, T., Chen, Z., Watanabe, S., Lin, C.D. *Two-dimensional electron momentum spectra of argon ionized by short intense lasers: Comparison of theory with experiment.* Phys. Rev. A, **75**, 023407 (2007).

[67] Salvat, F. *Optical-model potential for electron and positron elastic scattering by atoms.* Phys. Rev. A, **68**, 012708 (2003).

[68] DuBois, R.D. and Rudd, M.E. *Differential cross sections for elastic scattering of electrons from argon, neon, nitrogen and carbon monoxide.* J. Phys. B: Atom. Molec. Phys., **9**, 2657-2667 (1976).

[69] Chen, Z., Le, A.-T., Morishita, T., Lin, C.D. *Quantitative rescattering theory for laser-induced high-energy plateau photoelectron spectra.* Phys. Rev. A, **79**, 033409 (2009).

[70] Chen, Z., Le, A.-T., Morishita, T., Lin, C.D. *Origin of species dependence of high-energy plateau photoelectron spectra.* J. Phys. B, **42**, 061001 (2009).

[71] Cohen-Tannoudji, C., Diu, B., Laloë, F. *Quantum Mechanics*, Hermann and John Wiley & Sons (2000).

[72] Ishii, N., Kosuge, A., Hayashi, T., Kanai, T., Itatani, J., Adachi, S., Watanabe, S. *Quantum path selection in high-harmonic generation by a phase-locked two-color field.* Optics Express, **16**, 20876-20883 (2008).

[73] Meckel, M., Comtois, D., Zeidler, D, Staudte, A., Pavičić, D., Bandulet, H.C., Pépin, H., Kieffer, J.C., Dörner, R., Villeneuve, D.M., Corkum, P.B. *Laser-Induced Electron Tunneling and Diffraction.* Science, **320**, 1478-1482 (2008).

[74] Mehlhorn, W. *70 years of Auger spectroscopy, a historical perspective.* Journal of Electron Spectroscopy and Related Phenomena, **93**, 1-15 (1998).

Appendix A

Atomic Units

Quantity	Name	Symbol	SI value
mass	electron rest mass	m_e	$9.10938215(45) \cdot 10^{-31}$ kg
length	Bohr radius	a_0	$0.52917720859(36) \cdot 10^{-10}$ m
charge	fundamental charge	e	$1.602176487(40) \cdot 10^{-19}$ C
action	reduced Planck's constant	$\hbar$	$1.054571628(53) \cdot 10^{-34}$ J·s
energy	Hartree energy	E_H	$4.35974394(22) \cdot 10^{-18}$ J

Table A.1: **Fundamental atomic units.** The SI values are taken from National Institute of Standards and Technology (NIST), as recommended in 2006 by the Committee on Data for Science and Technology (CODATA) - see http://physics.nist.gov/cuu for details.

Quantity	Symbol	Formula	SI value
electric field	E	E_H/ea_0	$5.14220632(13) \cdot 10^{11}$ V/m
momentum	p	$\hbar/a_0$	$1.992851565(99) \cdot 10^{-24}$ kg·m/s
time	t	$\hbar/E_H$	$2.418884326505(16) \cdot 10^{-17}$ s
electric potential	V	E_H/e	27.2113838(68) V
permittivity	ϵ_0	e^2/a_0E_H	$1.112650056... \cdot 10^{-10}$ F/m

Table A.2: **Some derived atomic units.** The SI values are taken from National Institute of Standards and Technology (NIST), as recommended in 2006 by the Committee on Data for Science and Technology (CODATA) - see http://physics.nist.gov/cuu for details.